Prediction of turbulent flow and scour around bridge piers: Development of a non-hydrostatic model with non-uniform sediments

Shaghayegh Pournazeri

A Thesis
in
The Department
of
Building, Civil and Environment Engineering

Presented in Partial Fulfilment of the Requirements
for the Degree of Doctor of Philosophy
(Civil Engineering) at
Concordia University
Montreal, Quebec, Canada

September 2013

CONCORDIA UNIVERSITY
School of Graduate Studies

This is to certify that the thesis prepared

By: Shaghayegh Pournazeri

Entitled: Prediction of turbulent flow and scour around bridge piers:
Development of a non-hydrostatic model with non-uniform sediments

and submitted in partial fulfillment of the requirements for the degree of

DOCTOR OF PHILOSOPHY (Civil Engineering)

complies with the regulations of the University and meets the accepted standards with respect to originality and quality.

Signed by the final Examining Committee:

Dr. S. Williamson_____ Chair
Dr. S. Li_____Thesis Co- Supervisor (BCEE)
Dr. F. Haghighat_____Thesis Co- Supervisor (BCEE)
Dr. L. Wang_____ Examiner (BCEE)
Dr. C. Mulligan_____ Examiner (BCEE)
Dr. W. Ghaly_____ External Examiner (MIE)
Dr. Y. C. Jin_____ External Examiner (Univ. of Regina)

Approved by _____
Chair of Department or Graduate Program Director

_____ 2013 _____
Dean of
Faculty of Engineering and Computer Science

Abstract

Prediction of turbulent flow and scour around bridge piers: Development of a non-hydrostatic model with non-uniform sediments

Shaghayegh Pournazeri
Concordia University, 2013

The prevention and control of bridge scour is a challenging element in bridge-pier foundation design. Sediment scour from around the piers has been a main cause of all bridge failures. For the cost-effective and reliable design of pier foundations, one needs accurate prediction of flow-inducing scour. Such prediction can be obtained from numerical modelling, as a good extension of experimental results. General CFD software packages are incapable to simulate sediment transport (bedload) and bed-level change (scour/deposition). Some numerical models have been developed for bedload and scour simulations, but there are two major limitations: (1) the bed sediments are assumed to have uniform grain size which is not true in natural river channels; (2) the modelling techniques are not computationally efficient for applications at the field scale. Thus, new modelling techniques for scour prediction are needed.

The objectives of this research are: (1) to modify an existing shallow-water hydrodynamics model to allow for non-hydrostatic pressure corrections; (2) to improve the prediction of bed shear stress, a key parameter for bedload prediction; (3) to incorporate a new module for calculating bedload of mixed sediment-grain sizes; (4) to verify the model's prediction with existing experimental data.

For pressure corrections, a seven-diagonal linear system is added to the model, which is symmetric and positively defined. This system is numerically solved for non-hydrostatic

pressure through preconditioned conjugate gradient iterations. Then, corrections to velocity and water surface elevation due to non-hydrostatic pressure are obtained. Fractional bedload calculations are based on a surface-based transport function, which depends on a particle-hiding factor, bed shear stress, and grain size distribution. Bed level change caused by bedload is calculated using the Exner equation added to the model.

The new model successfully predicts 3-D velocities around a circular pier in a fixed scour-hole and scour development on a mobile bed with uniform and non-uniform sediments. We improve bed shear stress prediction by using near-bottom velocities, as opposed to the widely used bottom-layer velocity, in the wall function method. Velocity and scour depth predictions agree well with experimental data. We show that scour emerges from the lateral sides of a pier, and scour patterns move toward its upstream nose. On the upstream side, relative to the pier's centre, scour depth increases until the bed slope reaches the angle of repose of sediments. On the downstream side, scour continues until equilibrium is reached. Scour is deeper on the upstream than downstream side. Non-uniformity in grain sizes tends to reduce the magnitude of scour. The presence of the pier causes a strong vortex at its foot on the upstream side, which effectively moves sediments toward downstream. On the upstream side, the scour-hole's outer shape is almost half a cone, true for both uniform and non-uniform sediments. These findings have implications to foundation design. The modelling techniques presented in this study are computationally efficient and are practical for applications at the field scale, which have been difficult so far.

Acknowledgments

I would like to sincerely thank both of my supervisors, Professor S. Samuel Li and Professor Fariborz Haghighat for providing continuous support, encouragement, and supervision while accomplishing this work.

I would like to express my high appreciation to my advisor, Professor Li, for his tireless support and patience throughout my research. Without his help, this journey would have become impassable. His endless supports, generosity and strong management skills make him perfect as an adviser. I owe my intense interest to this field to him. I truly believe that this dissertation would not have been possible without his help and support.

I would like to acknowledge my supervisor, Professor Haghighat, for his endless help and support. His infinite knowledge and valuable comments made this dissertation reach to a desired quality. His generosity and support make him not only wonderful as a supervisor, but someone who can act as a role-model for the future life.

I would like to thank the examination committee members Professor Wahid Ghaly, Professor Liangzhu Wang, and Professor Catherine Mulligan whose comments and suggestions were extremely helpful in improving my manuscript. Special thanks to Professor Yee-Chung Jin from University of Regina, for serving as my external examiner.

I gratefully acknowledge Dr. Ayyoub Mehdizadeh for his help and valuable suggestions in the numerical code.

I would like to appreciate my lovely parents, Shahrzad and Bahram Pournazeri for their endless support, patience, and dedication throughout my whole life and especially kindly support to my little son, Shervin.

I am deeply grateful to my lovely brother, Sam Pournazeri who generously supported me and helped me in my PhD thesis academically and gave me great facilities to accelerate finishing this program. His mathematical understanding is tremendous and his scientific work inspired me a lot. My research has greatly benefited from his suggestions and kind supports.

Additionally, I would like to appreciate my very kind brother Mohammad Pournazeri who has been a great source of motivation and inspiration during my life.

Great thanks go to all my friends specially who helped me with different aspects of my PhD life.

Dedicated to my beloved parents, Shahrzad and Bahram; my generous and lovely brothers, Sam and Mohammad; my dear little son, Shervin.

CONTRIBUTIONS OF AUTHORS

This doctorate research thesis uses the manuscript-based format. The contributions of authors are clarified in the following:

(1) Chapter 3 is a manuscript prepared by S. Pournazeri, S.S. Li and F. Haghighat, which was submitted to the Canadian Journal of Civil Engineering in April 2013.

Pournazeri has contributed to data analysis, result discussion and the preparation of tables, figures and manuscript text. Li and Haghighat play the role of supervision and quality control.

(2) Chapter 4 is a manuscript prepared by S. Pournazeri, S.S. Li and F. Haghighat, which was accepted by Proceedings of the Institution of Civil Engineers-Water Management in May 2013.

Pournazeri has contributed to data analysis, result discussion and the preparation of tables, figures and manuscript text. Li and Haghighat play the role of supervision and quality control.

(3) Chapter 5 is a manuscript prepared by S. Pournazeri, S.S. Li and F. Haghighat (2013) which is submitted to Proceedings of the Institution of Civil Engineers-Water Management.

Pournazeri has contributed to method development, computational coding and testing, result interpretation and the preparation of tables, figures and manuscript text. Li and Haghighat play the role of supervision and quality control.

Table of Contents

List of Figures

List of Tables

List of Nomenclature

A_M	Horizontal eddy viscosity (m^2/s)
b	Channel width (m)
C_D	Bottom drag coefficient
c	Chezy coefficient
D	Pier diameter (m)
d	Size of the particle of interest (mm)
d_j	Grain size of the j'th sediment fraction (mm)
d_g	surface geometric mean grain diameter(mm)
d_s	Scour depth (m)
d_{se}	Equilibrium scour depth (m)
d_{50}	Median grain size of sediments (mm)
F_i	Horizontal diffusion term (m/s^2)
F_0	Approach flow Froude number
f_j	j'th fraction of sediment
g	Gravitational acceleration (= 9.81 m/s^2)
g_0	Reduced hiding factor
G	Bed load transport function
H	Flow depth below the datum (m)
HH	Height of the pier (m)
i	Cell index in the x_1 direction
j	Cell index in the x_2-direction or j'th sediment fraction
J	Total number of fractions
k	Cell index in the x_3-direction
K_M	Vertical eddy viscosity (m^2/s)
Kq	Vertical eddy diffusivity (m^2/s)
k_s	Bed roughness height (mm)
k_s^+	Roughness Reynolds number (defined as $k_s u_*/\nu$)
K_1	Correction factor for pier nose shape
K_2	Pier alignment factor
K_3	Correction factor for bed condition
K_4	Correction factor for armouring by bed material
L_1	Length of the approach flow channel section (m)
L_2	Length of the upstream scour hole (m)
L_3	Length of the downstream scour hole (m)
L_4	Length of the downstream channel section (m)
LL	piers' spacing (m)
l	Turbulence macro-scale (m)
m	Non-hydrostatic pressure correction (m^2/s^2)
n	Index of last cell
n_0	Distance from the bed (m)
p	Pressure (N/m^2)
q_b	Bed load flux ($m^3/s/m$)

(q_{b1}, q_{b2})	Bed load flux in (x_1, x_2) directions ($m^3/s/m$)
q_j	Bedload flux in the x_j-direction ($m^3/s/m$)
$q_t^2/2$	Turbulence kinetic energy (m^2/s^2)
Q	Discharge (m^3/s)
Re	Reynolds number
Rep	Particle Reynolds number
s	Specific gravity of sediments (= 2.65)
sl	Longitudinal slope
S_{ij}	Mean strain rate (sec^{-1})
St	Strouhal number
t	Time (sec)
t_e	Time of equilibrium (sec)
Δt	Time step (sec)
T	Non-dimensional excess bed shear stress
(U_1, U_2, U_3)	Depth-averaged velocity in the (x_1,x_2,x_3) directions (m/s)
(u_1, u_2, u_3)	Reynolds average velocity components in the (x_1, x_2, x_3) directions (m/s)
u_b	Bottom-layer velocity in the horizontal (m/s)
u_c	Threshold velocity (m/s)
u_j	Reynolds average velocity component in the x_i-direction (m/s)
u_*	Friction velocity (m/s)
u_p	Magnitude of velocity parallel to the bed surface (m/s)
u_{pc}	Particle velocity (m/s)
u_0	Cross sectional approach flow velocity (m/s)
$\tilde{u}_1$	Provisional velocity component in x_1 direction (m/s)
$\tilde{u}_2$	Provisional velocity component in x_2 direction (m/s)
$\tilde{u}_3$	Provisional velocity component in x_3 direction (m/s)
(u'_1, u'_2, u'_3)	fluctuating velocities in x_1, x_2, and x_3 direction
W_j	dimensionless fractional transport rate of the j'th fraction
w	Width of the pier (m)
(x_1, x_2, x_3)	Cartesian coordinates (m)
x_{3d}	Vertical coordinate of the parabola vertex below the flat-bottom level (m)
x_{3u}	Vertical coordinate of the cone vertex below the flat-bottom level (m)
Δx_i	Grid size in the x_i-direction (m)
Δx_1	Distance between adjacent grids in the x_1-directions (m)
Δx_2	Distance between adjacent grids in the x_2-directions (m)
Δx_3	Distance between adjacent grids in the x_3-directions (m)
y	Normal distance from the channel bed to a velocity point (m)
y^+	Normalised wall distance (defined as yu_*/v)
y_0	Approach flow depth (m)
z	Bed level above reference datum (m)
Δz_j	Difference in bed level between adjacent nodes in the x_j-direction (m)
α	Angle between near-bed velocity and the maximum slope direction (deg)
β	Angle of steepest descent or maximum bed slope (deg)
ε	Multiplication factor of critical shear stress
ε_o	Lower limit for ε
η	Free surface elevation (m)

$\tilde{\eta}$	Provisional free surface elevation (m)
θ_j	Angle of slope of local bed-surface in the x_j-direction (deg)
φ_c	Angle of repose of sediments (= 34º)
φ_0	Normalized bed shear stress
ψ	Implicitness factor
κ	von-Karman constant (= 0.41)
λ	Sediments porosity
ν	Molecular kinematic viscosity of water (m^2/s)
ξ	Vorticity (sec^{-1})
ρ	Density of water (= 1000 kg/m^3)
ρ_s	Density of sediments (= 2650 kg/m^3)
σ	Coordinate in vertical
σ_g	Geometric standard deviation of sediment
σ_φ	Arithmetic standard deviation of the surface size distribution
τ_b	Bed shear stress (N/m^2)
(τ_{b1}, τ_{b2})	Bed shear stress in (x_1, x_2) directions (N/m^2)
τ_c	Critical shear stress (N/m^2)
τ^*_c	Dimensionless bed shear stress
τ_{ij}	Turbulent shear stress (N/m^2)
τ_{max}	Local bed shear stress maximum (Pa)
τ_u	Particle momentum relaxation time (sec)
ω	Straining factor

Chapter 1 Introduction

In this chapter, the scope and motivation behind this research are discussed. The issue of bridge failure and scouring corresponding to the flow field around bridge piers are addressed followed by an outline of the contributions of this thesis.

1.1 BACKGROUND

One of the important issues in civil engineering is to protect the structure of bridge piers from collapse. Scouring, defined as the decrease in a riverbed's elevation caused by flow passing around bridge piers is a main reason for failure of bridge pier foundations. In an investigation of 823 bridge failures in the U.S.A. since 1950 (Shirole & Holt, 1991), it has been shown that 60% of the bridges' failures were due to scour around bridges' foundations and channel instability. Furthermore, the cost of each event was estimated at about US$100 million (Brice & Blodgett, 1978).Thus it is a high priority to predict the flow field and sediment transport around the bridge piers accurately in order to ensure the protection of such structures. As the flow approaches the bridge piers, it begins to separate, i.e. the fluid flow becomes detached from the surface of the object, and secondary flow such as eddies and vortices start forming. During separation, the fluid particles push off the object and cause a wake to develop.

The horseshoe vortices and the down flow play a key role in sediment transport and scouring around the bridge piers. Figure 1.1 illustrates the principal features and variables associated with clear water scouring around a circular pier in a steady flow over a planar bed of uniform, spherical, cohesion-less sediment near a state of incipient motion.

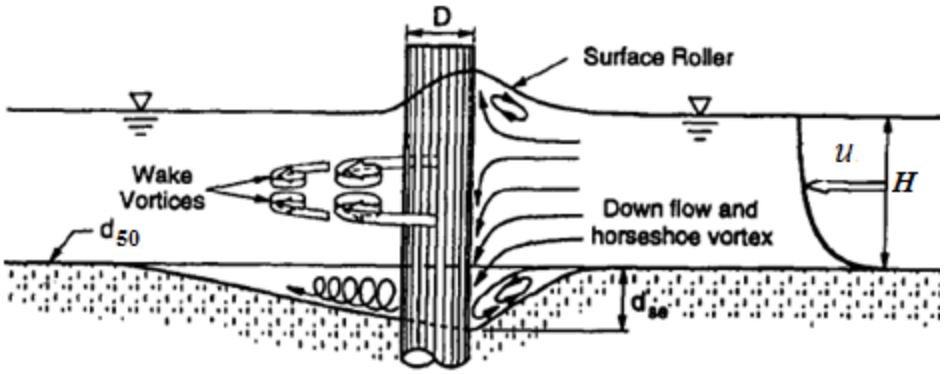

Figure 1.1 A vertical section, showing the general characteristics of the flow field and local scour around a circular pier, where d_{50} is the median diameter of sediment grains, D is the pier diameter, u is the distributed velocity of flow that approaches the pier, and H is the depth of flow (Ettema et al., 1998).

For the past decades, there have been many studies involved with the flow field and sediment transport around bridge piers such as Graf and Istiarto (2002), Dey (1995), Sadeque et al. (2008), Sarker (1998), Shepard and Miller (2006), Ettema et al. (2006), and Dargahi (1989). Most of these studies focused on flow around a single cylinder in a fixed flat bed and a fixed scour bed with uniform sediment as bed material. Moreover, most of the simulations were conducted under low Reynolds number flow conditions and measured the forces on the body of the piers. With respect to the hydraulics of sediment transport, the existing empirical equations tend to overestimate the depth of scouring due to the use of simplified assumptions for the pier's geometry in the laboratory, flow conditions, bed sediments, and river geometry. The development of the methods has not considered the complexity of the flow and scour phenomena occurring in nature. Thus more accurate investigations of scouring around a pier are required. The development of new methods for calculations of the flow field as well as sediment transport is necessary for a number of reasons, including:

- Most of the experimental studies have not considered the actual geometry of river channels; most of them were implemented for rectangular channels. Similarly, the geometry of piers

is usually simplified, adding another assumption to the problem. Thus they cannot reflect the real features in nature. Furthermore, the experimental studies are more time consuming and expensive. To avoid such problems, numerical modellings are of high preference to study the scouring process around bridge piers.

- Bed shear stress is the essential part to calculate the sediment transport; therefore, it is vital to estimate this value accurately. Some of the numerical studies calculated the bed shear stress using the bottom layer velocities (Khosronejad et al., 2012) which leads to high computational cost and time in real cases, and gives rise to numerical errors and model instability. Thus, it is necessary to find a new modelling approach to overcome such low computational efficiency problems.
- Most of the numerical studies for flow calculation and sediment transport were limited to highly simplified conditions such as considering uniform sediments as bed materials. As in nature, bed materials in river channels are a sediment mixture of different grain sizes, the non-uniformity of bed material should be included in the computation of the steady flow interaction with the sediment.
- As flow approaches the pier, the down flow upstream of the pier becomes a significant factor in scouring. Due to considerable vertical acceleration of flow near the pier resulting from obstruction, non-hydrostatic pressure should be included in hydrodynamic simulations of flow to attain more accurate results.

1.2 OBJECTIVES

In this study the 3-D flow around a cylindrical pier is predicted using a CFD code (HydroQual, 2002) with further development in a fixed scour bed and mobile bed. This study combines the hydrostatic hydrodynamics computations with non-hydrostatic

pressure corrections using efficient multi-layer techniques. The scour depth around a circular pier will be investigated using both uniform and non-uniform sediments for bed materials. Flow with a high Reynolds number is considered for this study. The results will be verified by existing experimental measurements. The major objectives of this study are as follows:

- Simulation of steady flow using an efficient multi-layer approach; considering non-hydrostatic pressure around a single cylinder in a fixed scour bed using the geometric and hydraulic condition of Graf and Istirato's (2002) experiment and comparison of the horizontal velocity with Graf and Istirato's (2002) measurements.
- Calculation of bed shear stress inside the scour hole around a cylinder using the wall function and near-bed velocities as opposed to bottom-layer velocities in order to decrease the numerical errors in bottom boundaries.

The predictions will be compared with those obtained by Graf and Istirato (2002).

- Simulation of steady flow around a cylinder in a mobile bed considering non-hydrostatic pressure corrections and simultaneous calculation of scouring in uniform sediment using geometric and hydraulic condition of Graf and Istiarto's (2002) experiment.

  The predictions of velocity and equilibrium scour depth will be verified through comparison with measurements.
- Simulation of steady flow around a cylinder in a mobile bed considering non-hydrostatic pressure and simultaneous calculation of scouring in non-uniform sediment using geometric and hydraulic condition of Chang et al.'s (2004) experiment.

  The prediction of equilibrium scour depth will be verified through comparison with measurement.

- Calculation of equilibrium scour depth around a pier using Chang et al.'s (2004) geometric and hydraulic conditions in uniform bed with the same median size of sediment as non-uniform bed material in order to investigate the effect of non-uniformity of sediment on the scour depth.

1.3 Overview and Contribution of the Dissertation

The contributions of this study are as follows:

- Employing a new modelling approach which combines layered hydrodynamics computations with non-hydrostatic pressure corrections to simulate the 3-D flow around a circular bridge pier.
- Using the approach of near bed velocity as opposed to bottom-layer velocities to obtain more reliable bed shear stress estimates and increase the computation efficiency.
- Predicting the scour depth around a circular pier considering non-uniformity of bed material.

The remainder of the thesis is organized as follows: In Chapter 2, a review of the literature is given, which covers the experimental, numerical and analytical research work on the topic of flow and scour around bridge piers. Chapter 3 provides a detailed description of efficient non-hydrostatic modelling of flow and bed shear stress in a pier scour hole (a manuscript submitted to the Canadian Journal of Civil Engineering). An efficient multi-layer model for pier scour computations considering uniform bed material is described in Chapter 4 (a paper in press, Proceedings of the Institution of Civil Engineers-Water Management). Chapter 5 presents a bridge scour model with non-uniform sediments (a manuscript submitted to Proceedings of the Institution of Civil Engineers-Water Management. Chapter 6 contains conclusions and some discussions for future work.

Chapter 2 Literature Review

This chapter provides a review of the literature pertinent to the problem of water flow and riverbed sediment erosion around bridge piers in a river channel. It begins with a brief introduction of some fundamental quantities and concepts traditionally used to study turbulent flows. Then, a description of grain size distributions of a sediment mixture, together with the concept of critical shear stress, is given. This is followed by discussions about the progress made through the previous studies of the problem as well as their limitations.

2.1 DESCRIPTION OF TURBULENT FLOW

The instantaneous water velocities around bridge piers fluctuate rapidly in time and space even if the flow that approaches the bridge piers is relatively steady. At high values of the Reynolds number, Re, the flow is turbulent. For such value, a point is reached where a transition occurs in which disturbances are no longer damped out but rather are amplified (Bernard and Wallace, 2002). Turbulent flow is dominated by inertial forces, which tend to produce chaotic eddies, vortices and other flow instabilities. They contain considerable vorticity.

Let $<u_1, u_2, u_3>$ denote the three orthogonal components of the instantaneous velocity vector, $\vec{u}$. By the Reynolds decomposition, the velocity components may be written as the sum of the depth average velocity and the fluctuating velocity. For example, we have

$$u = U + u' \tag{2.1}$$

The former computed in numerical simulations, except direct numerical simulations, whereas latter is parameterized. In other words, the effects of the fluctuating velocities on

the Reynolds-averaged velocity field are taken into account indirectly.

Some quantities frequently used to describe the turbulent flow field are listed below:

The vorticity of the velocity field, mathematically expressed as

$$\zeta = \frac{1}{2}\nabla \times \langle U_1, U_2, U_3 \rangle \tag{2.2}$$

Specific turbulent shear stress, for example

$$\tau_{12} = -\rho \overline{u_1' u_2'} \tag{2.3}$$

where the subscripts can be 1, 2 or 3, for the x_1-,x_2- and x_3-direction, respectively.

Turbulent kinetic energy

$$q_t^{\,2}/2 = \frac{1}{2}\left(\overline{u_1'^2} + \overline{u_2'^2} + \overline{u_3'^2}\right) \tag{2.4}$$

where the over bar presents the Reynolds average of the quantity. The turbulent shear stresses appear due to non-linear interactions of the flow velocity components. Of particular interest are the spatial and temporal distributions of the 3-D Reynolds-averaged velocity and the above-mentioned quantities upstream and downstream of bridge piers (Graf and Istiarto, 2002). In sediment erosion applications, it is critical to obtain reliable calculations of the turbulent shear stresses.

Some turbulence models do not use constant turbulent viscosity or diffusivity but calculate them from turbulence quantities such as turbulent kinetic energy and dissipation rate. These quantities are predicted using one or two differential transport equations (Rodi, 1993). The former is known as one-equation turbulence model, whereas the latter is referred to as two-equation turbulence model, e.g. k-ε and k-ω.

2.2 RIVERBED SEDIMENT

2.2.1 Grain size distribution

Riverbed sediments include sands and gravel of grain sizes ranging from 0.062 to 64 mm. The sediments are commonly subdivided into three major groups: mechanical, chemical, and organic (Hechanova, 1977). Figure 2.1 shows three sample distributions of sediment grain size. Soil A is well graded, with all sizes of grains in a proportion that makes it easy to compact to maximum density. Soil B is coarse fraction predominant. Soil C is fine fraction predominant.

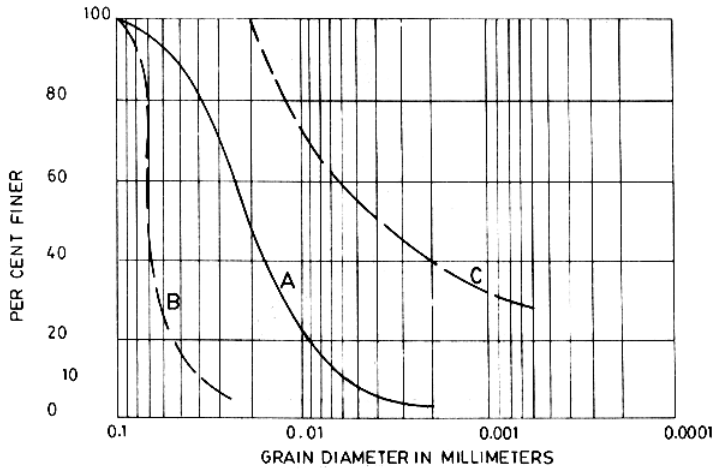

Figure 2.1 Distribution of grain size (Hechanova, 1977)

2.2.2 **Critical shear stress**

The critical shear stress is defined as shear stress corresponding to the general movement of bed materials. According to Graf and Altinakar (1998), it correlates well with the plasticity and void ratio. Shields (1936) conducted flume experiments and developed an expression for the critical shear stress, τ_c, to move a particle of a given size

$$\tau_c = \tau_c^* \times g(\rho_s - \rho)d \tag{2.5}$$

where τ_c^* is dimensionless critical shear stress, g is the acceleration due to gravity, ρ_s is the

density of sediment, ρ is the density of water, and d is the size of the particle of interest. The widely used Shields diagram empirically shows how the dimensionless critical shear stress required for the initiation of motion is a function of a particular form of the particle Reynolds number, Re_p, or Reynolds number related to the particle. The diagram shows that in gravel-bed channels of homogeneous sediment sizes and turbulent flow, the value of dimensionless critical shear stress is 0.06. Fischenich (2001) provided a list of empirical expressions to estimate the critical shear stress for various types of sediment grains, including clays, silts, sands, gravel and cobbles. Table 2.1 shows the value of critical shear stress for different sizes of grains (Julien, 1995).

Table 2.1 Critical shear stress for different sizes of grains (Julien, 1995)

Class Name	Grain size (in)	Dimensionless Critical bed shear stress
Boulder		
Very large	>80	0.054
Large	>40	0.054
Medium	>20	0.054
Small	>10	0.054
Cobble		
Large	>5	0.054
Small	>2.5	0.052
Gravel		
Very coarse	>1.3	0.05
Coarse	>0.6	0.047
Medium	>0.3	0.044
Fine	>0.16	0.042
Very fine	>0.08	0.039
Sands		
Very coarse	>0.04	0.029
Coarse	>0.02	0.033
Medium	>0.01	0.048
Fine	>0.005	0.072
Very fine	>0.003	0.109
Silt		
Coarse	>0.002	0.165
Medium	>0.001	0.25

2.3 FLOW AND SCOURING AROUND BRIDGE PIERS

The problem of water flow and riverbed sediment erosion around bridge piers is notoriously difficult to deal with. Even under simplified conditions, the problem is intractable analytically. Most of the previous studies of the problem have taken the experimental and numerical approaches, as discussed below.

2.3.1 Experimental investigations: Single pier

The simplest consideration is a single cylindrical pier in a river channel, as in the experimental studies by Melville and Raudkivi (1977), Dargahi (1989), Dey (1995), Sarker (1998), Sadeque et al. (2008) and Unger and Hager (2007).These studies improved the understanding of the flow patterns in response to changes in hydraulic and structural conditions. Melville and Raudkivi (1977) investigated the flow patterns, distributed turbulence intensity, and distributed boundary shear stresses in the scour zone. They analyzed water-flow over a mobile sediment bed for different fixed scour stages. The flow patterns were traced using the hydrogen-bubble method. The velocity magnitudes and turbulence intensities within the scour hole were measured by a DISA hot-Film anemometer. Before starting measurements, the loose sediment bed was coated with plaster to retain three stages of scour: (1) the initial flat bed, (2) the scoured bed after 30 min and (3) equilibrium scour conditions. The main results concerned the flow patterns in vertical and horizontal planes, the turbulence intensity and the bed shear stress distribution. Additionally, this study indicates the existence of a non-scour inducing single horseshoe vortex during all three stages. Another significant limitation of Melville and Raudkivi's (1977) work was that the bed sediments had a uniform grain size; this is also the case in most of the experimental studies discussed below. The implication is that the results may

not be directly applicable to natural rivers where sediments often have mixed grain sizes.

Using the same measurement techniques, Dargahi (1989) carried out laboratory experiments of flow patterns around a single cylindrical pier in a flat-bed channel. The experiments covered the Reynolds number, *Re*, of 6600–65000. The author showed that the number of vortices increased with increasing *Re*. However, the vortex system's dimensions were independent of *Re*; they were primarily determined by the cylinder's diameter, *D*. Dargahi (1989) also observed that wake vortices caused bursts downstream of the cylinder.

The effects of sediment grain size and pier's diameter were investigated by Dey (1995) and Sarker (1998). Dey (1995) focused on 3-D quasi-steady vortex flow and large secondary vortex flow. The experimental conditions were as follows: The scour hole was stable; the flow regime was clear water; the Reynolds number was 10,000–20,000; the bed materials used were sands of two different grain sizes (0.26 and 0.58 mm); the pier's diameter was given three different values. Velocity vectors were measured by a five-hole pitot sphere. The results of this study showed that the horseshoe vortex started with zero intensity at the bed, and attained the maximum at the free surface. The flow separated at the edge of the scour hole and produced a reversal nature of radial component of velocity in the hole. The variation of such a velocity component along x_3 axis (the vertical axis) is linear within the hole. It starts from zero in the middle depth and reach the positive value at the bed, it becomes negative at x_3=0, with the same magnitude. The implication of this model is that the model is not compatible with the real nature due to considering fixed scour bed for the channel. In reality, the bed is mobile therefore the flow simulation should be done with sediment transport simultaneously.

Sarker (1998) considered various wave-current combinations. In the experiments, the approach velocity varied between 0.1 to 0.24 ms^{-1}. Velocity measurements from an Acoustic Doppler Velocimeter (ADV) showed lower longitudinal velocity magnitudes close to the pier throughout the depth of flow. The magnitudes gradually increased further away from the pier. Reversed flow took place below the bed level, with higher values of velocity closer to the pier. Stronger reversed velocity occurred for larger pier sizes.

Given that ADV measurements are intrusive, the significance of disturbances induced by ADV probe ought to be assessed. The same issue needs to be addressed with respect to measurements from an acoustic Doppler velocity profile (ADVP), as used in Graf and Istiarto (2002) for measurements of instantaneous velocity, vorticity, the Reynolds shear stress and turbulence intensity, upstream and downstream of a bridge pier.

Sadeque et al. (2008) investigated the flow around cylindrical objects in an open channel which are of equal diameter and four heights. They were tested under similar flow conditions producing four different levels of submergence, including a surface piercing bridge-pier-like cylinder. Horse-shoe vortex systems were found to appear closer to the submerged cylinders compared to a surface piercing cylinder. The increase in dimensionless bed-shear stress is found to be inversely related to the level of submergence of the cylinders.

The internal flow features around circular bridge piers by Particle Image Velocimetry applied both in the horizontal and vertical planes were investigated by Unger and Hager (2007). The temporal evolution of the vertical deflected flow at the pier front and the horseshoe vortex was explored. The study showed that the main effects along the pier front, such as down-flow, up-flow and the stagnation point do not explicitly vary with time while

the horseshoe vortex develops with time.

In Graf and Istiarto (2002), three different methods for calculating the bed shear stress were discussed. They are based on, respectively, a) velocities measured near the bed of the channel for example at x_3=4mm, such velocity at the distance of n_0 was calculated, u_p; the bed shear stress was calculated as well:

$$\tau_{0,1} = \rho \nu_t \left(\frac{\partial u_p}{\partial n_0} \right) \tag{2.6}$$

where $\nu_t = 1.3 \times 10^{-5}$, u_p is the magnitude of velocity parallel to the bed surface and n_0 is the shortest distance from the bed.

b) measured shear stress distribution. In order to obtain the bed shear stress, extrapolation towards the bed was used;

$$\tau_{0,2} = -\rho \left(\overline{u'_1 u_3'} \right)|_{bed} \cos\theta \tag{2.7}$$

where θ is the angle of slope of scour hole.

c) a relation for the velocity distribution(Graf and Altinakar, 1998), the bed shear stress was evaluated by:

$$\tau_{0,3} = \rho \left(U . \sqrt{\frac{g}{c^2}} \right)^2 = \rho (0.07U)^2 \tag{2.8}$$

where U is the local depth averaged flow velocity and c is the Chezy coefficient. In this study c=44 [$m^{1/2}/s$].

The experimental results of Graf and Istiarto (2002) are summarized below. First, the bed shear stress gradually reduces when entering the scour hole (Figure 2.2).

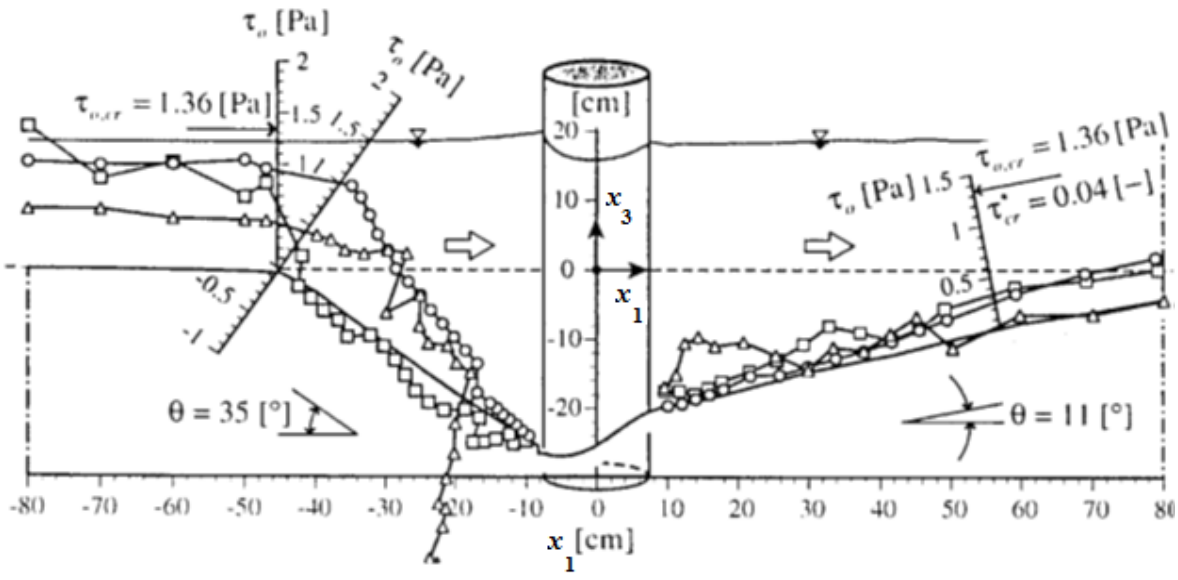

Figure 2.2 Estimated bed shear stress in the plane upstream and downstream of the cylinder by Graf and Istiarto (2002), □ relates to $\tau_{0,1}$; Δ relates to $\tau_{0,2}$; ○ relates to $\tau_{0,3}$.

Secondly, a strong horseshoe vortex system appears upstream of the cylinder, positioning at its foot, another weaker vortex forms due to the change in the slope of the bed surface leading into the scour hole. Downstream of the cylinder, a flow reversal occurs near the water surface; the vorticity is relatively weak in this region. Lastly, the turbulent kinetic energy is very strong at the foot of the cylinder on the upstream side as well as in the wake behind the cylinder. The Reynolds number of the experiments is high, being 81,000. The above-mentioned flow characteristics are in agreement with those obtained by Dey (1995).

Ettema et al. (2006) conducted experiments with cylinders of different diameters placed in a uniform sandy bed channel. The Reynolds number was 2.9×10^4–1.86×10^5 and the total depth of flow was 1 m. The author obtained a direct trend between the scour intensity and frequency of large-scale turbulence shed from each cylinder. Six values of *D* were used in his study. The strength and extent of the vorticity structures behind the cylinder were

determined from ADV and large-scale particle image velocimeter (LSPIV) measurements (Figure 2.3). Some of the experiments revealed sediments being entrained and moved from the scour hole by wake vortices. The author suggested a relationship between scour depth and pier diameter (Figure 2.4). It can be seen that scour depth is decrease by increasing the diameter of the cylinders.

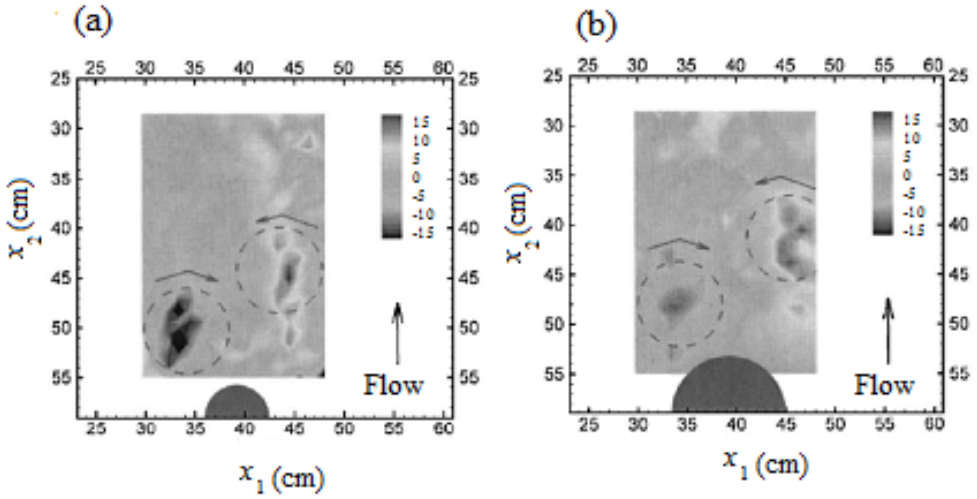

Figure 2.3 Time-averaged structures of the wake vortices behind a cylinder of diameter *D*: (a) *D* = 64 mm, and (b) *D* = 114 mm, showing contours of horizontal-plane vorticity. Eddies produced by the smaller cylinder (a) are of much higher vorticity than the wake vortex formed by the large cylinder (b), Ettema et al. (2006)

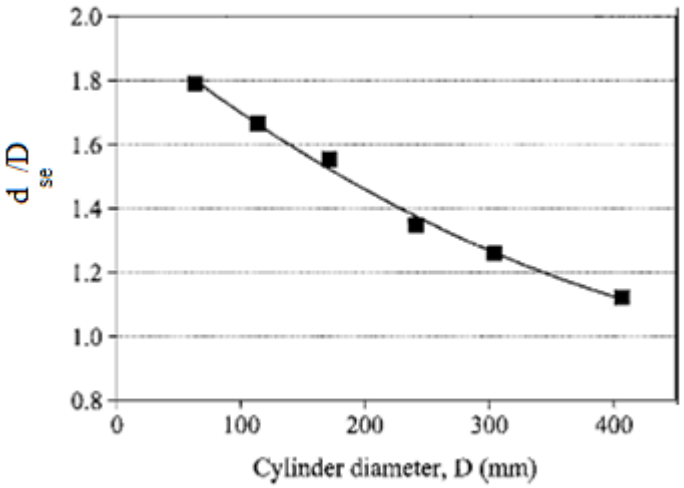

Figure 2.4 Relationship between scour depth d_{se} and pier diameter, D, showing that normalized d_{se} increases with decreasing D (Ettema et al., 2006)

The empirical methods of various degrees of complexity derived by many researchers for determining local or maximum scour depth, the methods developed by Melville and Chiew (1999), FHWA (2001), Sheppard et al. (2004),Sheppard and Miller (2006), Raudkivi and Ettema (1983), Raudkivi (1986), Melville and Sutherland (1988), Jain and Fischer (1980), Melville, (1997), Grade and Kothyari (1998), Johnson (1992), Laursen and Toch (1956), Melville (2008) are well-referenced.

Melville and Chiew (1999) investigated the temporal development of clear-water local scour depth at cylindrical bridge piers in uniform sand beds. The results show that the scour depth after 10% of the equilibrium time is between about 50% and 80% of the equilibrium scour depth, depending on the approach flow velocity.

The new method with the addition of a time factor to Melville's (1997) equation and simplified to apply to cylindrical piers founded in uniform sediments, was updated by Melville and Chiew (1999) which is as follows:

$$d_s = K_{yd} K_I K_d K_t \tag{2.9}$$

where $K_t = d_s / d_{se}$; $K_{yD} = 2.4D$, when $D/(H+\eta) < 0.7$; and $K_{yD} = 2\left((H+\eta)D\right)^{0.5}$, when

$0.7 < D/(H+\eta) < 5$; $K_{yD} = 4.5(H+\eta)$, when $D/(H+\eta) > 5$; $K_I = U/u_c$, when $U/u_c < 1$; $K_I = 1$, when $U/u_c > 1$; $K_d = 0.57\log(2.24D/d_{50})$, when $D/d_{50} < 25$; and $K_d = 1$, when $D/d_{50} > 1$; u_c means approach flow velocity at threshold condition for sediment movement, d_{50} is the median size of sediment, D is the pier's diameter, U is the depth average velocity, H is the flow depth below the datum d_s is the scour depth, d_{se} is the equilibrium scour depth and η is the free surface elevation.

The functional dependence of normalized equilibrium scour depth d_{se}/D on D/d_{50} in the clear-water scour range reported earlier by Sheppard et al. (1995) was verified by Sheppard et al. (2004) as follows

$$d_{se}/D^* = 2.5 f_1\left((H+\eta)/D^*\right) f_2(U/u_c) f_3\left(D^*/d_{50}\right) \tag{2.10}$$

$$f_1\left((H+\eta)/D^*\right) = tanh\left[\left((H+\eta)/D^*\right)^{0.4}\right] \tag{2.11}$$

$$f_2(U/u_c) = 1 - 1.75\left(\ln(U/u_c)\right)^2 \tag{2.12}$$

$$f_3\left(D^*/d_{50}\right) = \frac{D^*/d_{50}}{0.4(D/d_{50})^{1.2} + 10.6(D/d_{50})^{-0.13}} \tag{2.13}$$

where U is local depth average velocity, u_c is the velocity at threshold condition for sediment motion, $D^*=k'w$; k' is 1 for a circular pier, and 1.23 for a square pier; w is the width of the pier.

To determine pier scour, an equation based on the *CSU* equation (FHWA, 2001) was recommended for both live-bed and clear-water pier scour which is as follows:

$$d_s/(H+\eta) = 2K_1K_2K_3K_4\left(D/(H+\eta)\right)^{0.65} F_0^{0.43} \tag{2.14}$$

where d_s is scour depth, H is flow depth directly upstream of the pier, K_1 is correction factor for pier nose shape, K_2 is correction factor for angle of attack of flow, K_3 is correction factor

for bed condition, K_4 is correction factor for armouring by bed material size, D is pier diameter and F_0 is Froude Number directly upstream of the pier.

Raudkivi and Ettema (1983) indicated that the equilibrium depth of clear-water local scour is related to the grading of the bed sediment. As the geometric standard deviation of the particle size distribution increases, the equilibrium scour depths decrease. Moreover, The equilibrium depth of local scour decreases with the decreasing relative size of pier diameter to mean bed particle size for values less than about 20 to 25. The equilibrium depth of local scour decreases at a greater rate with decreasing flow depth for smaller values of the relative flow depth which is the result of interference of the water surface roller formed around the pier with the downwards flow into the scour hole.

Raudkivi (1986) studied the controlling factors for scour depth at a bridge pier in subcritical flow including: (1) Pier width or diameter; (2) type and grading of sediment; (3) flow depth relative to pier width or diameter; (4) size of sediment relative to pier width (important mainly for laboratory experiments); and (5) alignment of piers. The author showed that the shape of piers has only as mall effect on scour depth. The major factors of uncertainty were the alignment of flow during flood conditions and the changes to pier shape and dimensions caused by debris or ice rafts caught on the pier.

Melville and Sutherland (1988) presented a design method for scour depth prediction using multiplying factors which reduces the maximum depth of the scour hole of 2.4D. Such factors are applied where clear-water scour conditions exist, the flow depth is relatively shallow, and the sediment is relatively large. Moreover, the shape factor and alignment factor were applied in the case of non-cylindrical piers.

The predicted scour depth at high flow velocity through a formula was shown by Jain

and Fischer (1980). They also showed that after decreasing slightly, upon the onset of sediment transport in a stream, scour depth increases again with increasing the velocity.

Sheppard and Miller (2006) studied the local scour around a circular pier for a range of water depths and flow velocities. The experimental conditions were such that the Reynolds number ranged from 7×10^4 to 6.5×10^5, the pier diameter was $D = 0.15$ m, and non-cohesive sands used had median grain sizes of d_{50} equal to 0.26 mm and 0.83 mm. In Figure 2.5a,b, predictions (solid curves) of d_{se} are compared with experimental data (dots). This figure shows that at higher value of u/u_c, the dependency of normalized equilibrium scour depth on D/d_{50} decreases and the depth of the scour hole tends to a constant value.

It can be seen that Sheppard and Millar's (2006) findings contradicted Ettema et al.'s (2006) finding which showed the decreasing of scour depth by increasing the pier's diameter.

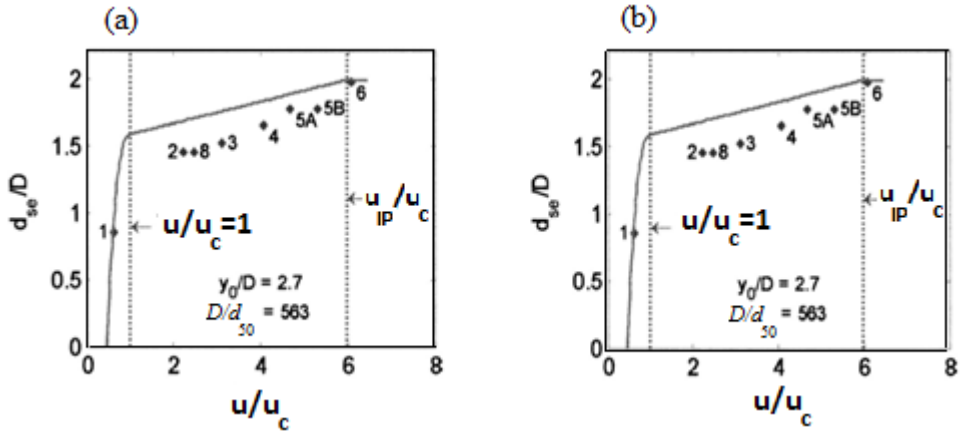

Figure 2.5 Measured (dots) and predicted (solid curves) scour depth d_{se} (normalized by the pier diameter D) versus flow velocity, u, normalized by the critical velocity, u_c, for two D/d_{50} ratios: (a) 181, and (b) 563 (Sheppard and Miller, 2006)

The experimental results of Yanmaz and Altinbilek (1991), Mia and Nago (2003), and Melville and Chiew (1999) considering uniform sediments as bed material showed that the bed evolution is the function of time. In Mia and Nago's (2003) experiment, the shape of

the scour hole around the pier was approximated as an inverted cone throughout the elapsed time of scour, and the angle of the scour hole was considered equal to the angle of repose of the sediment.

The comparison of scouring in uniform and non-uniform sediment was investigated by Chiew and Melville (1989) who found that the scouring in non-uniform sediment is less than or equal to that in uniform sediment.

Oliveto and Hager (2002) showed that the temporal evolution of scour depth regarding non-uniform sediments as bed material is a function of depth of the flow and velocity.
The effect of grain size on scour depth was investigated by Raikar and Dey (2005), Chang et al. (2004) and Debnath and Chaudhuri (2010). Chang et al (2004) investigated the sediment size variation of surface bed material and found a regressed formula for estimating the mixing layer thickness in terms of median size of sediment and geometric standard deviation of grain size distribution. The study has also shown that the relation between scour depth and time is approximately linear in the very short period of time, thus the scour rate may be assumed to be a constant for such period of time. Furthermore, the equilibrium time of scour in non-uniform sediment was estimated in terms of equilibrium time in uniform sediment and a correction factor related to geometric standard deviation of grain size. Regarding scouring under unsteady flow, Chang et al. (2004) showed that the scour depth increases steadily during the rising period of the hydrograph and changes only slightly during the recession period.

The temporal variation of scour around circular bridge piers placed in uniform, non-uniform, and stratified beds under steady and unsteady clear-water flows was investigated by Kothyari et al. (1992). He proposed a scheme along with an equation which enables

computation of the temporal variation of scour depth in uniform and non-uniform materials. He used the effective size of non-uniform material to calculate the non-uniform sediment transport by regression analysis of the data of Ettema (1980).

2.3.2 **Experimental investigations: Multiple cylindrical piers**

Akilli et al. (2004) extended the investigation of flow around bridge piers to include two and three side-by-side circular cylinders. These cylinders were given the same diameter. A particle image velocimeter (PIV) was used to measure the flow field. The transverse gap, *LL*, between adjacent cylinders was one third of the cylinder diameter (*LL*/*D* = 1/3). The Reynolds number was 5×10^3. The PIV measurements gave time-averaged patterns of velocity vectors, vorticity, Reynolds stress contours and streamline topology (Figure 2.6 and Figure 2.7). In Figure 2.6a, the Karman vortex shedding interfered with each other and acted as a single vortex. Figure 2.6b and Figure 2.6c show the asymmetric flow pattern. Such flow sometimes deflects to the upper cylinder and sometimes it deflects to the lower cylinder. In Figure 2.6d, two distinct coherent vortex streets are observed downstream of the cylinders.

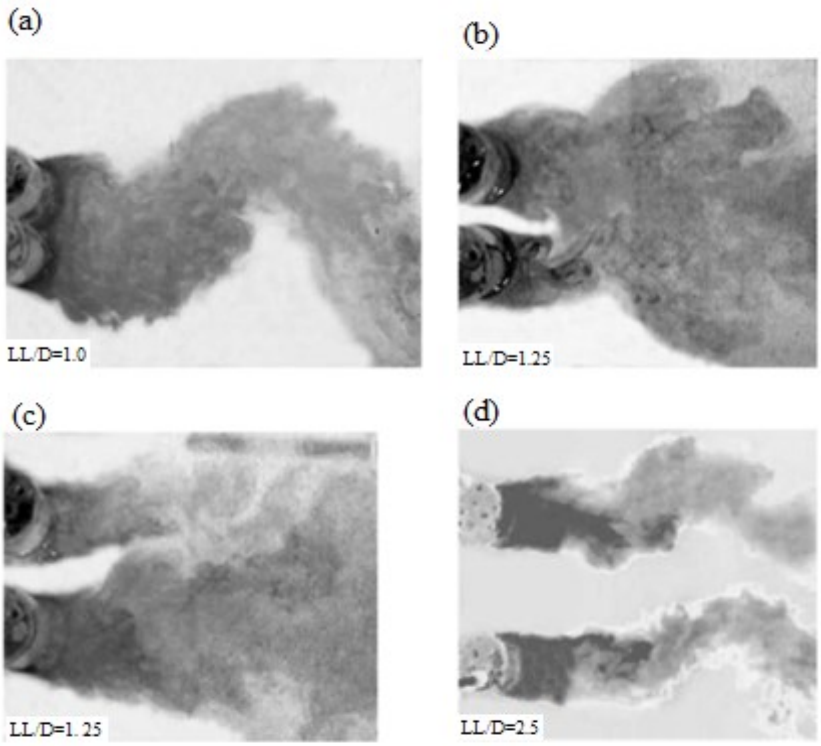

Figure 2.6 Flow patterns visualized using tracer dye. Two circular cylinders were arranged side-by-side. (Akilli et al., 2004)

In three side by side cylinders, the vortex shedding is different. When the piers are close to each other, a couple vortex shedding is observed (Figure 2.7a).When the distances between the piers increase and reach LL/D=1.25 (Figure 2.7b,c), two different patterns of vortex shedding can be seen, wider wake region downstream of the central pier and two narrow wakes downstream of outer piers (Figure 2.7b). In Figure 2.7c, the wider wakes can be seen downstream of the outer cylinders. In this case, both asymmetrical flow structure at the small gap ratio (LL/D=1.25) and symmetrical flow structure at the intermediate gap ratios ($1.5 < LL/D < 2$) were observed. Bi-stable wake regions were obtained especially for the gap ratio of LL/D=1.25, for both the two and three side-by-side cylinder arrangements. When the gap ratio reach 2.5 (Figure 2.7d) the Karman vortex shedding is observed downstream of the outer cylinders.

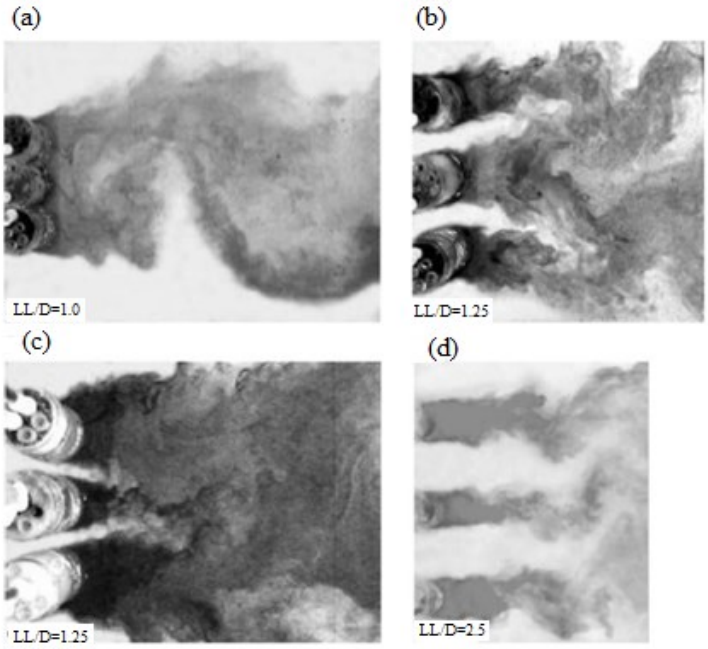

Figure 2.7 Flow patterns visualized using tracer dye. Three circular cylinders were arranged side-by-side (Akilli et al., 2004)

The implication of this study shows that if the piers of the same diameter are close to each other the vortex shedding induced by them is wide. On the other hand, if the piers are far from each other the vortex shedding induced by the piers become distinct from each other. In other words, the distance between piers is important in interaction of the wakes induced by piers.

2.3.3 **Numerical investigations: Single pier**

Richardson and Panchang (1998) simulated 3-D flow at the base of a bridge pier within a scour hole. The two equation k-ε model and Renormalized Group theory (RNG) were used for turbulence closure. The simulations allowed for three scouring stages: an initial flat bed, an intermediate scour hole, and an equilibrium scour hole that matches the measured scour hole of Melville and Raudkivi (1977). The simulations corresponded to approach velocity of 0.25m/s. Richardson and Panchang's (1998) results near the bed

appear to be less sensitive to the choice of turbulent closure schemes than the geometric grid representation. Far from the bed, the results are somewhat sensitive to the choice of turbulent parameterizations. A number of uncertainties possibly appear in Richardson and Panchang's (1998) results:

The drag coefficient used is based on laboratory experiments. On one hand, variations in experimental conditions inevitably produce different values for the drag coefficient. On the other hand, the equilibrium scour depth depends on the coefficient; this depth is not a single value (as used) but varies from case to case.

The scour hole has been assumed to be of cone shape at all times, which neglects the variations in shape at the different stages of scouring.

A mound develops downstream of the pier (Melville and Raudkivi, 1977); However, a lack of information has prevented the consideration of the exact shape of the mound.

In fact, the simulations failed to reproduce the vertical and reversed flow near the bed. They also failed to reproduce the unique feature of high velocity contours penetrating down to the scour hole.

Using large eddy simulations (LES), Yen et al. (2001), Breuer (1998), and Catalano et al. (2003) computed 3-D flow velocity around a circular pier.

In Yen et al.'s (2001) model, the down flow was computed using a flat bed and was scaled up to obtain the corresponding jet flow in the scour hole. This treatment at best gives a very crude approximation for the true flow velocity in the scour hole. Also, the use of the empirical van Rijn (1984) formula developed for the bed load transport of uniform sands means the results are not valid for conditions of a sediment mixture of different grain sizes.

Nevertheless, Yen et al.'s (2001) predictions of flow velocities (Figure 2.8) appear to

agree reasonably well with the laser Doppler velocimeter (LDV) measurements made by Yeh (1996) under flatbed conditions. A reasonable comparison of final scouring between simulations and laboratory measurements is plotted in Figure 2.9.

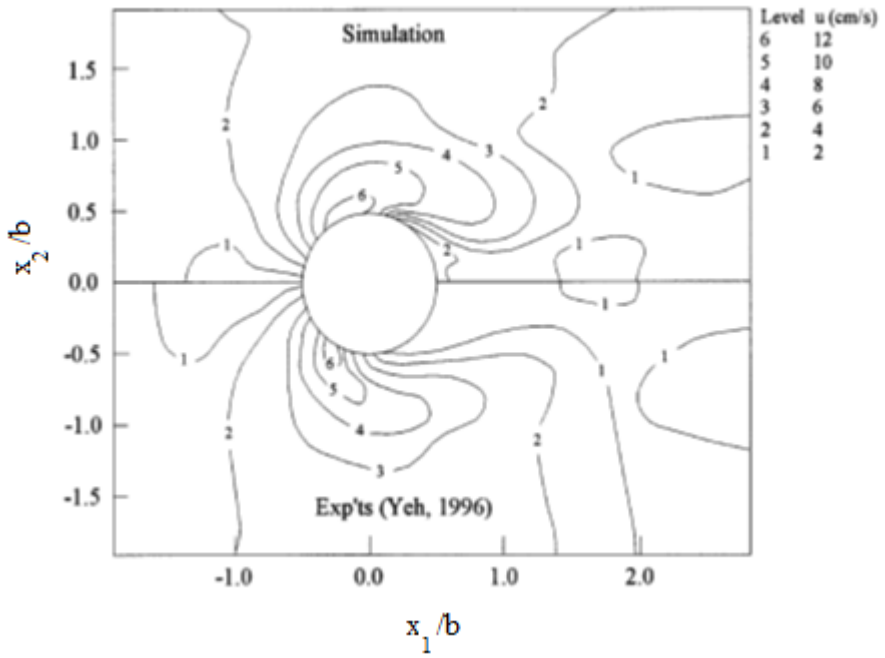

Figure 2.8 Comparison of simulated (upper half) and measured (lower half) isovels on the horizontal plane at x_3/D = 0.032 around the pier (Yen et al., 2001)

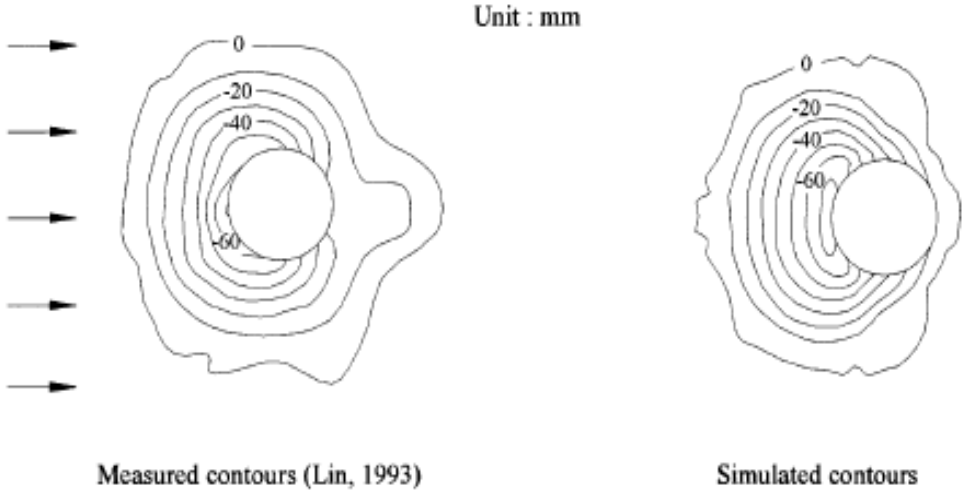

Figure 2.9 Comparison of measured (Lin, 1993) and simulated final bed elevation contours- a verification, (Yen et al., 2001)

Using the CFD software FLUENT, Salaheldin (2004) simulated the flow around a pier

under the condition of clear water and an intermediate Reynolds number. The purpose was to compare the performance of a number of turbulence models (available in FLUENT) in terms of bed shear stress and scour initiation area $\tau_b/\tau_c > 1$. The author suggested that the k-ε model performed poorly, leading to overestimates of the scour initiation area and unrealistic distributions of near-bed flow velocity and shear stress. This is not surprising; the k-ε model is invalid for conditions where turbulence is non-isotropic, as is the case near solid boundaries. The Reynolds stress model was recommended because of good predictions of distributed velocities and shear stresses on a flat bed and in the scour hole.

Ali and Karim (2002) also used FLUENT to investigate the effect of different size of scour hole and time duration on flow pattern. However, the code was not able to consider the increase in water surface.

Roulund et al. (2005) computed the flow field and bed scouring around a cylindrical pile, with a three-dimensional model known as EllipSys3D (Danish Computing Centre). The sediments were uniform and non-cohesive. The PISO algorithm (Issa, 1985), was used to calculate the unsteady flow, and k–ω model (Wilcox, 1993) was used for turbulence closure. Computations were carried using both fixed and mobile bed channels. The simulation of flow field was done considering a rigid bed. This model does not have free surface facility and there is a 'lid' at the top surface, thus it is applicable when the Froude number is small ($F_0 < 0.2$). The pile Reynolds number was 100 to 2×10^6.

In the computations of mobile bed scouring, the mesh is continuously adjusted in response to changes in bed topography. Water velocities are computed by multiplying an empirical coefficient with the friction velocity. This is questionable. The equation of motion in the direction of the particle motion shows that the particle moves with constant

velocity. This assumption may be unrealistic. In order to verify the computational results, LDA velocity measurements and bed shear stress measurements from hot film were available. The results indicated that the size of the horseshoe vortex as well as the bed shear stress under the horseshoe vortex increased with increasing ratio of boundary-layer thickness to the pile diameter until the latter quantity reached a certain value. The results also showed that the horseshoe vortex size and bed shear stress under the vortex changed significantly with the Reynolds number; when $Re < 500$, the size increases with increasing Reynolds number, and when $Re > 500$, the size reduces with increasing Reynolds number. The influence of the bed roughness on the horseshoe vortex was found to be negligible.

The computed scour depth was smaller (by 15%) than the scour depth measured in the experiment. This was attributed to the fact that the steady-state flow model did not take into account the unsteady effects such as vortex shedding and horseshoe vortex in front of the pier and did not consider the suspended load due to vortex shedding which caused unpredicted scour depth downstream of the pier.

Some numerical models with sophisticated formulations have been applied to the problem of 3-D flow around piers with a scour module (Dehghani et al., 2012; Olsen and Melaaen, 1993; Khosronejad et al., 2012; Nagata et al., 2005) or without a scour module (Said et al., 2008).

Nagata (2005) conducted simulations to predict the bed deformation around hydraulic structures and one cylinder. The Reynolds number based on flow depth varied from 4675 to 37544. The RANS equations were solved, together with the k-ε turbulence closure. The bed topography was calculated by coupling a stochastic model for sediment pick up and deposition and by using a momentum equation of sediment particles. The bed materials

were uniform sands. The topography of equilibrium scour was computed for a mobile bed and the local bed slope was initially estimated. Bed scouring occurred gradually near the edge of the scour hole, which made the edge smooth, although the actual edge of the scour hole was sharp. Flow simulations were first implemented for a fixed scour bed and the results were compared with those obtained by Melville (1975). Then, a moving boundary-fitted coordinate system was employed to simulate the unsteady flow field especially at the initial stage of scouring and at the equilibrium stage. The overall scour geometry was reasonable. This study was an extension of Richardson and Panchang's (1998) study in order to identify vertical and reversed flow near the bed more clearly and reproduce the unique feature of high velocity contours penetrating down to the scour hole.

Khosronejad et al. (2012) carried out experiments and numerical simulations to investigate the scour pattern around three different shapes of the piers using unsteady Reynolds averaged Navier–Stokes (URANS) equations closed with the k-ω turbulence model. He found that for piers with a blunt leading edge, the URANS model cannot resolve the energetic horseshoe vortex system at the pier/bed junction and thus significantly under-predicts both the scour depth at the nose of the pier and the rate of scour growth.

Considering a square cylinder under the condition of a relatively high Reynolds number, Srinivas et al. (2006) investigated the flow around the pier using LES. The computations made use of the finite difference techniques on staggered grids in which scalar variables such as pressure is stored in the cell centres of the control volumes, whereas the velocity or momentum variables are located at the cell faces. The grid spacing was high near the cylinder and coarse far from it. The no-slip boundary condition was imposed at the walls. The upwind scheme was used for discretization of the convective term and the Adams-

Bashforth scheme, having second-order accuracy in time for time advancement, and the dynamic subgrid scale stress model of Piomelli and Liu (1995) have been used. The Courant-Friedrichs-Lewy condition was used to determine the maximum allowable time step.

In Figure 2.10a,b, the time-averaged axial velocity, $<u_1>$, and transverse velocity, $<u_2>$, downstream of the square cylinder were compared with the LDV measurements of Lyn et al. (1995). The LES results of Wang and Vanka (1996) were also shown for comparison. The distributions of the normal and shear stresses appear to be well predicted by Srinivas et al. (2006).

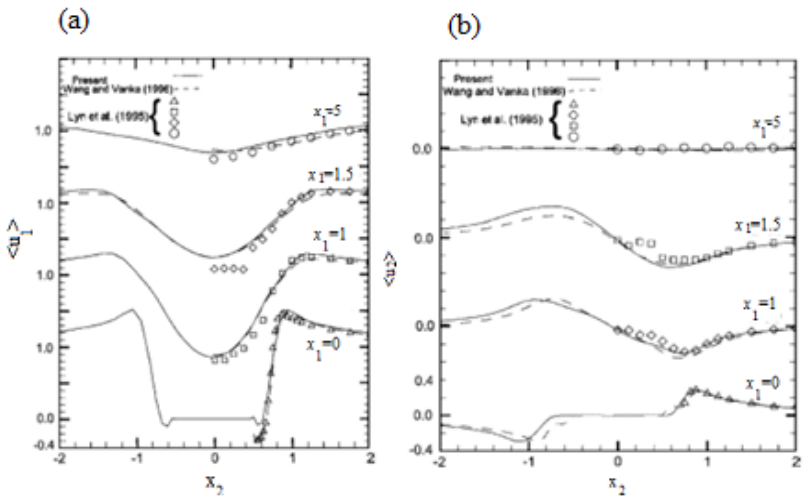

Figure 2.10 (a) Time-averaged streamwise velocity profiles at x_1=0.0, 1.0, 1.5 and 5.0; (b) Time-averaged transverse velocity profiles at different downstream locations x_1=0.0, 1.0, 1.5, and 5.0 (x_1 is in direction of flow, x_2 is in transverse direction), (Lyn et al., 1995)

In the near wake there is more coherence than in the far wake, whereas in the far wake, the magnitudes of coherent and incoherent components are comparable. The phase averaged data in the far wake is random and the incoherence fluctuations in the far wake are larger than in the near wake. At the high Reynolds number, vortices shed in the near wake underwent breakup; therefore, the cascade mechanism of energy transfer as in

developing turbulent flow was established.

Recently, Pasiok and Stilger-szyd (2010) took the particle trajectory approach in order to investigate sediment motion and turbulent flow around piers with a scour hole, as illustrated in Figure 2.11. The author used LES for the flow-field, and allowed for friction and gravity forces acting on particles. The equation of particle motion is as follows:

$$\frac{du_{pc}}{dt} = -\frac{u_{pc} - u}{\tau_u} + g \tag{2.15}$$

$$\tau_b = \frac{4}{3}\frac{\rho_s d}{\rho C_D \left| u_{pc} - u \right|} \tag{2.16}$$

where upc is the particle velocity, u is the fluid velocity, d is the size of the particle of interest, ρs is the density of particle, CD is drag coefficient, τu is particle momentum relaxation time and ρ is the density of water. The model is applicable for uniform sediments only. Pasiok and Stilger-szyd (2010) showed that particles trajectories depend on the intensity of wake vertical vortices, which are the main force to move particles out of the scour hole. The markers tended to concentrate in vertical vortex cores or regions of local vorticity maxima and pressure minima. Once trapped into a vortex core, markers were transported out of the scour hole.

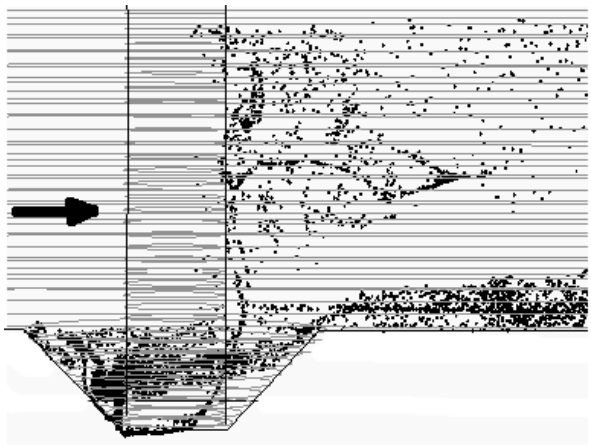

Figure 2.11 Marker particles around a cylindrical pier with a scour hole (Pasiok and Stilger-szyd, 2010)

Using SSIIM code, Aarabi et al. (2011) investigated the time variation of local scour with non-uniform sediment around a cylindrical pier. The maximum scour depth which occurred at lateral sides of the pier was compared with the depth of the scour hole at the nose of the pier obtained by Chang et al. (2004). It has been shown that the predicted results and the measurements are in good agreement. However, the locations of occurrence of maximum scour depth show a discrepancy between numerical calculations and measurements.

2.3.4 **Numerical investigations: Multiple piers**

Said et al. (2008) conducted 3-D numerical simulations using the Reynolds stress model (RSM) for turbulence closure. The purpose was to examine the effects of a single cylinder and two tandem cylinders on the flow field. PIV techniques were used in the wind tunnel experiments for velocity data in order to validate numerical results. The Reynolds number ranged from 8.5×10^3 to 6.4×10^4. In the case of two cylinders in tandem, the flow patterns in the gap region were examined as a function of the distance between the cylinders. The author encountered difficulties in capturing the velocity field close to the cylinder surface.

Some modelling studies (e.g. Akbari and Price, 2005; Papaioannou et al., 2006) have

been conducted to investigate the flow patterns under the low Reynolds number condition. Such studies are limited to laminar and early turbulent flow regimes. In Papaioannou et al. (2006), the flow around two tandem cylinders over a flat bed with Re=100–1000 was simulated to document the influences of three-dimensionality, cylinder spacing and their coupling. The issue of three-dimensionality was addressed by a comparison between 2-D and 3-D simulations (Figure 2.12). It is interesting to note that there is a critical cylinder spacing for vortex formation and shedding in the gap region, depending on the Reynolds number.

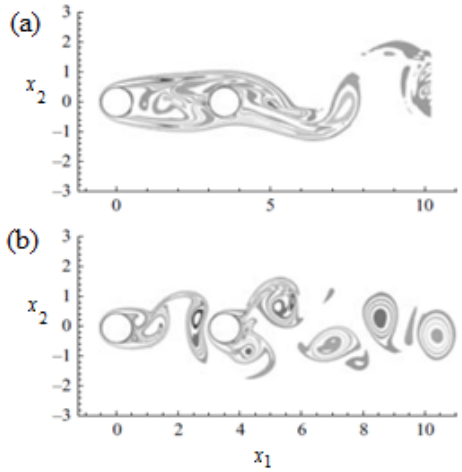

Figure 2.12 (a) Instantaneous vorticity field from 3-D predictions; (b) compared to that from 2-D predictions; the cylinder spacing is LL/D = 3.5, Re= 500, (Papaioannou et al., 2006).

The 3-D simulations predict reattachment (Figure 2.12a), whereas the 2-D simulations predict vortex shedding in the gap region (Figure 2.12b), which is termed the co-shedding or binary vortex regime. The 2-D and 3-D predictions differ not only in the vorticity field but also in the force on the downstream cylinder as well as in the shedding frequency of the tandem system (Figure 2.12). Papaioannou et al. (2006) indicated that the differences become larger at a higher Reynolds number. In the 2-D simulation, at much smaller value

of LL/D, the reattachment ceases in comparison with 3-D simulation. A follow up study by Papaioannou et al. (2007) showed that an increase in cylinder spacing leads to an increase in the maximum oscillation of the downstream cylinder. A decrease in cylinder spacing gives rise to flow reattachment and the two cylinders behave like a single cylinder.

The flow past two side-by-side identical circular cylinders was investigated by Kun et al. (2007) using unstructured spectral element methods. Akbari and Price (2005) investigated the effect of the cylinders arrangement on flow pattern around them. Depending on the Reynolds number and cylinder spacing, nine different wake patterns were predicted; five of them shown in Figure 2.13 are under supercritical flow condition. Clearly, the wake structure of the flow past two side-by-side cylinders is much more complex than that of the flow past a single cylinder.

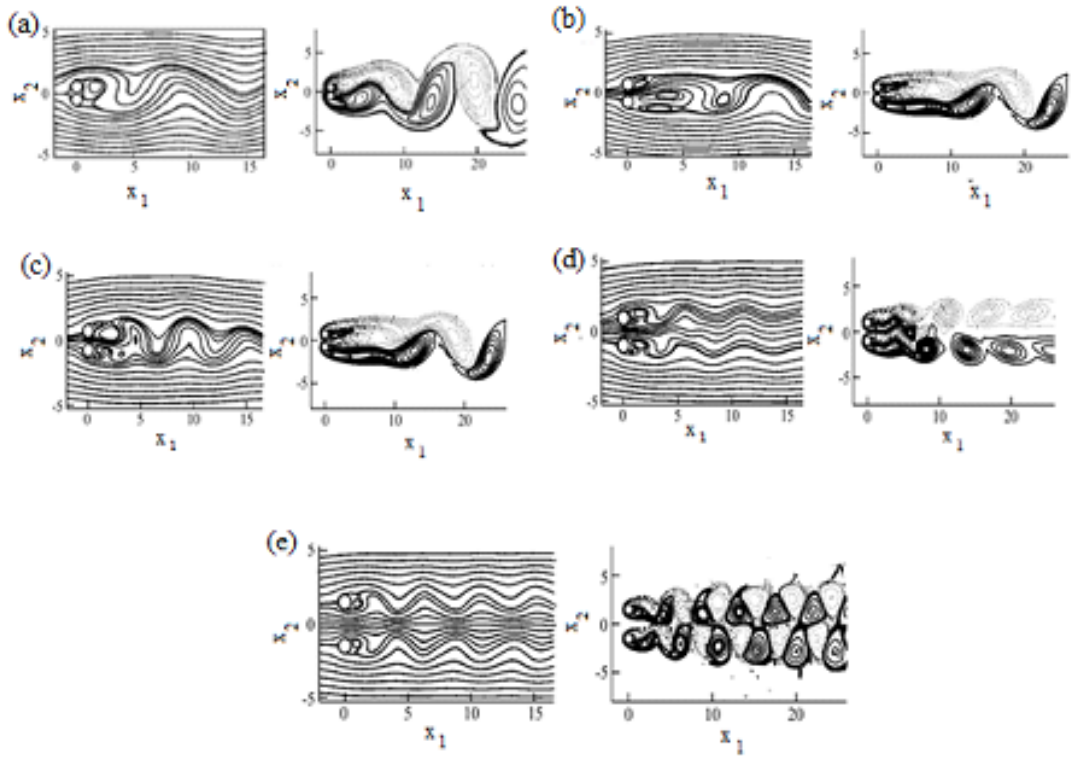

Figure 2.13 Predicted streamlines (panels to the left) and the vorticity field (panels to the right), showing (a) single bluff body periodic patterns with LL/D = 1.1 and Re = 30, (b) biased quasi-steady patterns with LL/D = 1.5 and Re = 70, (c) quasi- periodic patterns with LL/D = 1.5 and Re = 100, (d) in-phase-synchronized patterns with LL/D = 2 and Re = 5, and (e) anti-phase-synchronized patterns with LL/D = 3 and Re = 100, (Kun et. al, 2007).

Motta et al. (2007) calculated maximum depth of the scour hole around the bridge piers using CFX-5. The not coherent uniform sediment size was used in Motta et al. (2007) model. The suspended sediment transport was computed through the advection-dispersion equation. They showed that the bed shear stress was locally increased around the points of flow separation along the upstream edges of the piers, where a large decreasing of the bed level occurred, especially for the upstream part of the pier.

A number of researchers (Lam et al., 2008; Lin et al., 2008; Lam and Zou, 2009) have conducted numerical investigations on turbulent flow past four cylindrical piers. Lam et al. (2008) considered four cylinders in an in-line square configuration in 2-D and 3-D

simulations using FLUENT. The computational domain is 24D×24D×16D. The author focused on the effects of different spacing under low Reynolds number condition (Re = 100 and 200). Simulations in 2-D produced three flow patterns: I) stable shielding flow, II) wiggling shielding flow, and III) vortex shedding flow. These results revealed the relationship between flow pattern transformation and the pressure characteristics of the four cylinders. The amplitude of the maximum fluctuating pressure on the downstream cylinder surface was increased by 4–12 times when the flow pattern transformed from (I) to (II) at Re = 100, while the amplitude of maximum fluctuating pressure was enhanced by 2-3 times when the flow pattern transformed from (II) to (III). There is a large discrepancy between the 2-D results and laboratory observations at LL/D=4 and Re=400 due to neglecting the strong 3-D effects at the end of the cylinders when the aspect ratio, HH/D, is low and the cylinder spacing is critical; HH is height of cylinder, D is diameter of cylinder and LL is longitudinal and transversal distance between the piers. Thus, 2-D simulations are not adequate. In

Figure 2.14, the flow pattern agrees well with the flow visualization results shown in Figure 2.15 obtained with flow visualization methods.

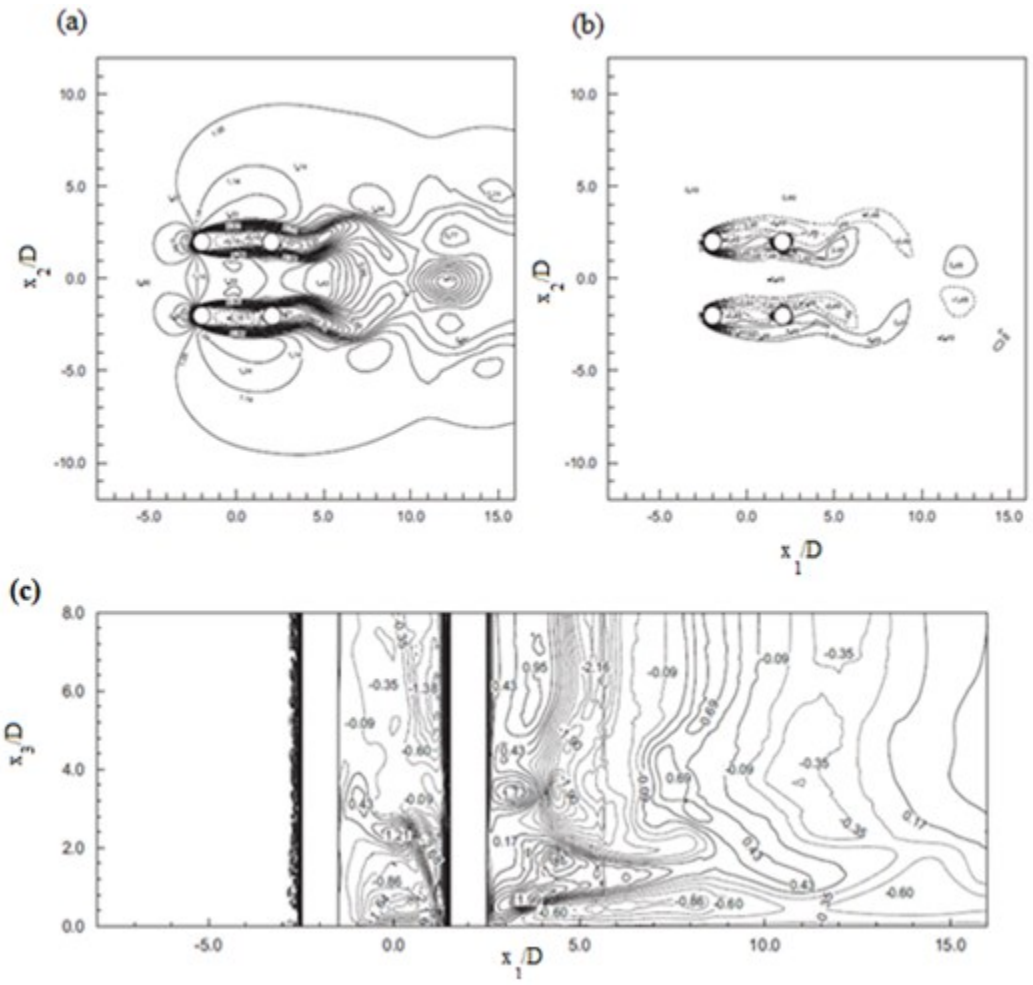

Figure 2.14 Contours of flow velocity and vorticity for 3-D simulations: (a) Predictions of normalized flow speed u_1/u_0 in the plane of $x_3/D = 8.0$. (b) Predictions of normalized vorticity $\omega_z D/u_0$ in the plane of $x_3/D = 8.0$, where ω_z is x_3 vorticity; (c) Predictions of normalized vorticity $\omega_z D/u_0$ in the plane of $x_2/D = -2.0$. The origin of the coordinates system is at central point of four piers at the bottom surface. Solid curves are positive value levels and dashed lines are negative, $Re = 200$. (Lam et al., 2008)

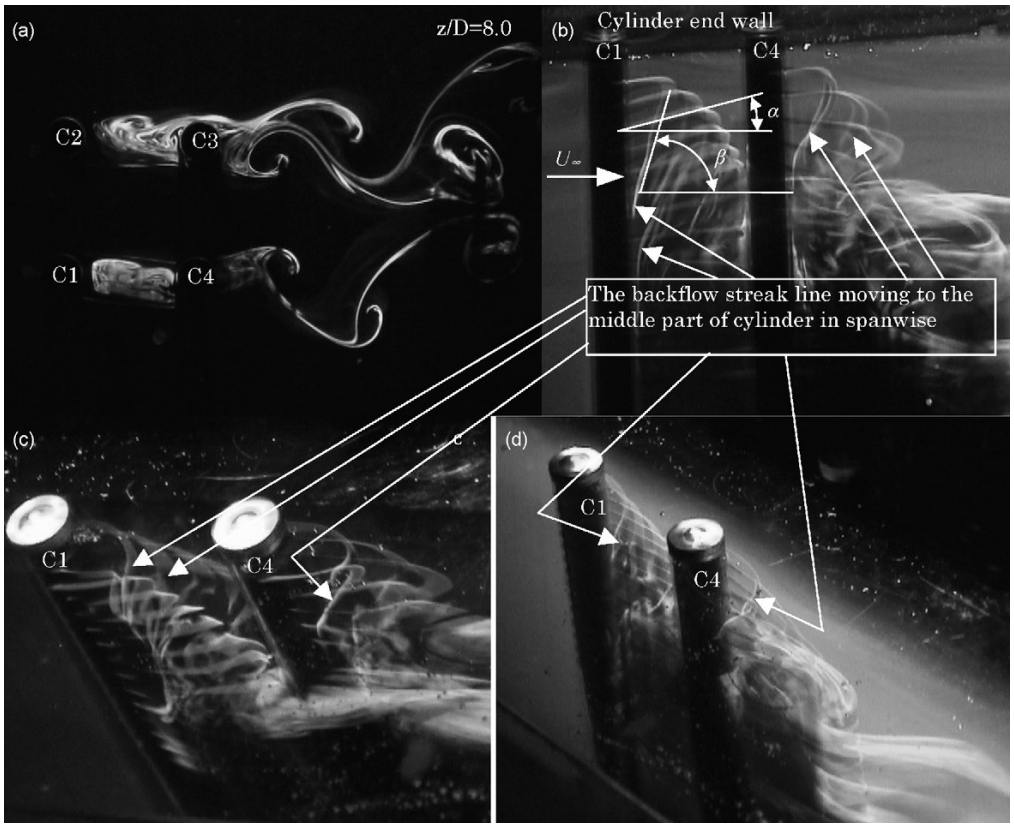

Figure 2.15 Flow pattern at cylinder end observed by visualization at LL/D = 4.0, Re = 200 and HH/D = 16.0. (a) Flow pattern in the cylinder middle plane, (b) view in the x_2-direction, (c) and (d) view in an oblique top direction. In (c) only the inside dye is illuminated; (b)–(d) show the backflow and no shedding vortex forming near the cylinder end plane (Lam et al., 2008)

Lin's et al. (2008) 3-D LES simulations were limited to the case of flat bottom. The cylinder arrangement is shown in Figure 2.16. The author used unstructured hexahedral grids and considered spacing ratios of LL/D = 1.5 and 3.5. The bi-stable nature of wake flow patterns was predicted behind the downstream cylinders when two cylinders were positioned close to each other. At larger cylinder spacing, in-phase and anti-phase vortex shedding occurred (Figure 2.16). Lin et al. (2008) indicated that the numerical results were validated using LDA and PIV measurements.

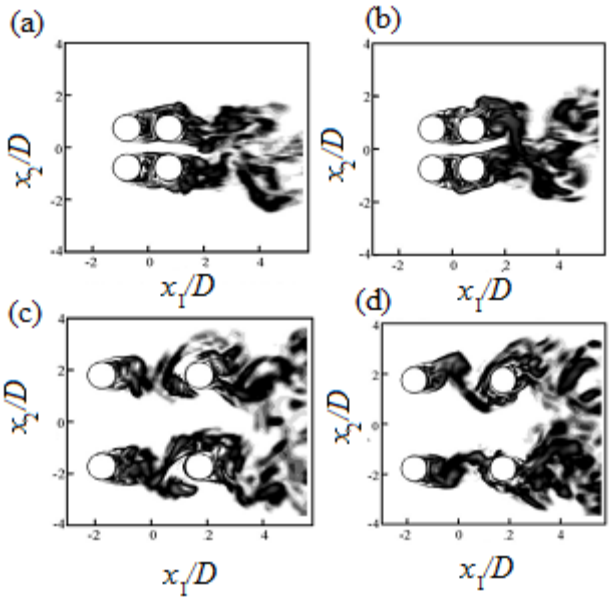

Figure 2.16 Instantaneous vortex structures, showing (a) downward deflection at LL/D = 1.5; (b) upward deflection at LL/D = 1.5; (c) in-phase vortex shedding at LL/D = 3.5; (d) anti-phase vortex shedding at LL/D = 3.5, and Re = 1.5×10^4 (Lin et al., 2008)

Lam and Zou's (2009) numerical investigation is similar to that of Lin et al. (2008), considering four cylinders in an in-line square configuration at different spacing. The Reynolds number is 1.1–2.0×10^4. Lam and Zou's (2009) LES results of mean velocity are plotted in Figure 2.17 showing that an increase in the Reynolds number leads to a decrease in the level of asymmetry of the wake velocity profiles.

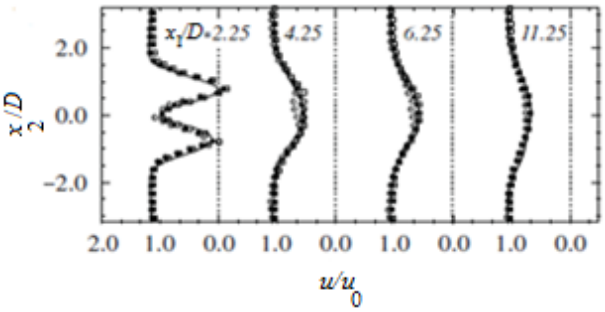

Figure 2.17 Predicted distributions of the mean streamwise velocity from LES (solid curves) at four different x locations and at the Reynolds number of Re = 1.5×10^4. LDA data (for Re = 1.1×10^4, for Re = 1.5×10^4, and Re = 2.0×10^4) are plotted for comparison. The solid curves are plotted more or less through the LDA data points. The cylinder spacing ratio LL/D is 1.5. (Lam and Zou, 2009)

Lam and Zou (2009) also used PIV for measuring the instantaneous spanwise vorticity and velocity (Figure 2.18). In Figure 2.19b,d, contours of the time-averaged root-mean-square in the x_1–x_2 plane of the streamwise velocity fluctuation, u_1u_1', and the transverse velocity,u_2', from PIV measurements are plotted. The cylinder spacing ratio is $LL/D = 1.5$ and the $Re = 1.5\times10^4$.The LES results are plotted in Figure 2.19a,c for comparison.

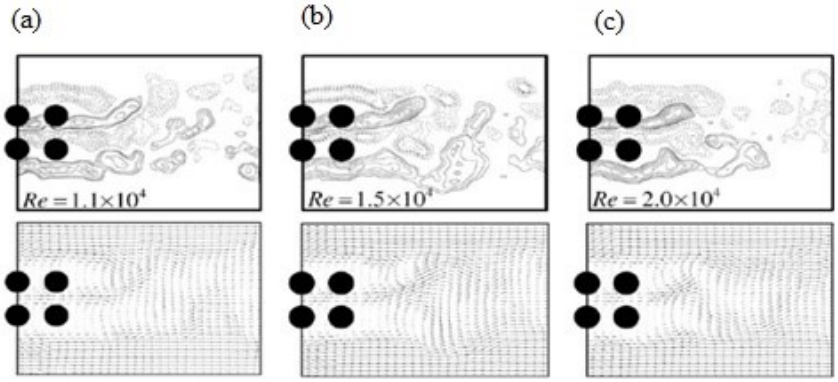

Figure 2.18 Instantaneous vorticity field (top panels) and velocity field (bottom panels) from PIV measurements at different values for the Reynolds number, *Re*. The *LL*/*D* ratio is 1.5. Dashed and solid lines correspond to negative and positive vorticity, respectively (Lam and Zou, 2009).

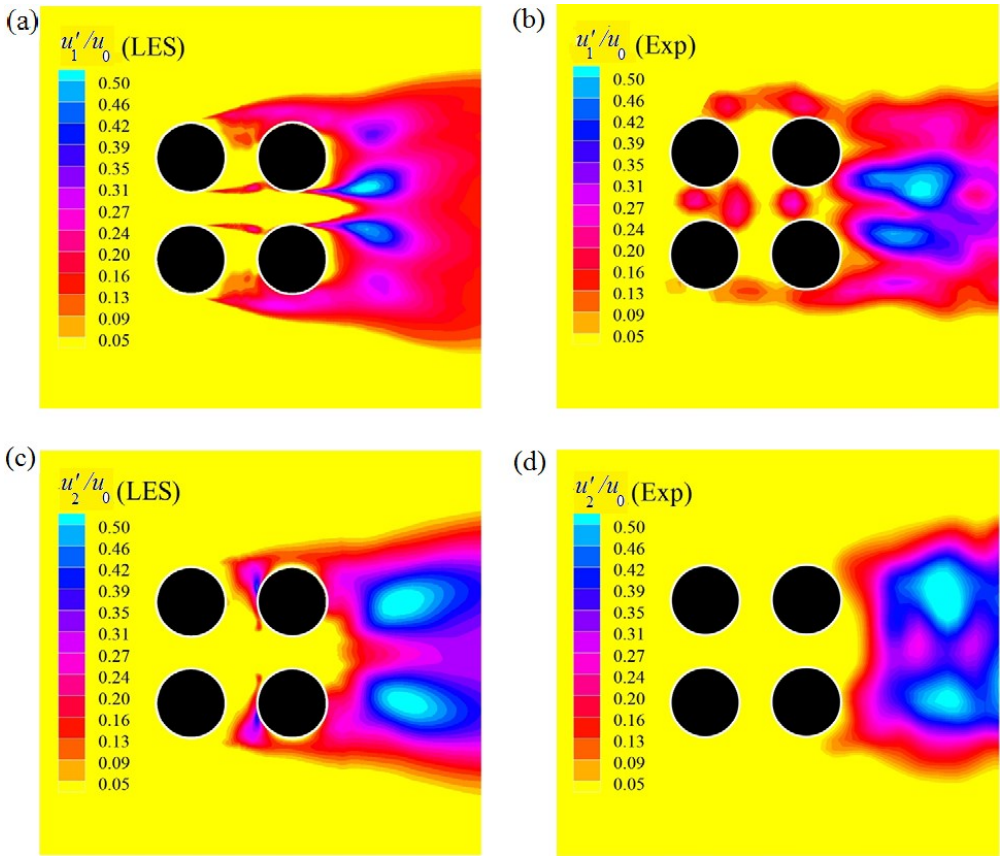

Figure 2.19 Time-averaged streamwise (u_1') and transverse (u_2') velocity fluctuations from PIV measurements (Exp) and LES simulations (LES) at the LL/D ratio of 1.5, and Re=1.5×10^4. The velocity fluctuations have been normalized by the speed of the approach flow u_0 (Lam and Zou, 2009).

From Lam and Zou's (2009) LES, the velocity field around the cylinders shows similar features to what are shown in Figure 2.16 from Lin et al. (2008). Distinct flow patterns are possible, depending on the cylinder spacing as well as the Reynolds number. These factors also affect the extent of vortex formation upstream and downstream of the cylinders. A symmetrical flow pattern occurs at larger spacing.

In what follows, an efficient non-hydrostatic model of flow and bed shear stress in a pier scour hole is described (Chapter 3), an efficient multi-layer model for pier scour computations with uniform sediment is covered (Chapter 4), a bridge scour model with non-uniform sediments is presented (Chapter 5), and conclusions are drawn (Chapter 6),

along with discussions for future work.

Chapter 3 Efficient non-hydrostatic modelling of flow and bed shear stress in a pier scour hole

Summary: Predicting 3-D flow in a pier scour hole and the associated bed shear stress is important for the safe and economical design of bridge piers. This paper combines layered, hydrostatic hydrodynamics computations with non-hydrostatic pressure corrections, exploring a new modelling approach for efficient and reliable predictions of 3-D flow velocity. The law of the wall method is used for estimating the bed shear stress. Its suitability for incorporation into layered models for bedload transport and pier scour simulations is also discussed. The predicted flow shows realistic features: strong downward flow adjacent to the upstream nose of a circular pier, vortex motions in the vertical and horizontal, and meandering flow wakes. The velocity results compare well with available experimental data. In the approach region, the bed shear stress is uniform. It attains a local maximum immediately before flow enters the scour hole and then drops non-linearly in the scour-hole region toward the pier. In the wake region, the bed shear stress has very low values. The bed shear stress predictions are consistent with the experimental data. In multi-layer models, when applying the law of wall method, one should use near-bed velocities as opposed to bottom-layer velocities to obtain more reliable bed shear stress estimates and avoid fluctuating features, which can cause a numerical instability problem in bedload transport simulations.

3.1 INTRODUCTION

Numerous cases exist where river flow has caused severe bridge pier scour and structural failures. For the safe and cost-effective design of the structures, it is vital to be able to predict the flow around piers and the associated bed shear stress τ_b as essential input to scour predictions. The flow field is complicated. Turbulent horseshoe vortices initiate at the foot of a pier and wrap around it, strong downward flow appears immediately upstream of the pier, and intricate wake flow occurs downstream (Dargahi, 1989).

In the past, considerable research efforts have been devoted to the study of pier scour and its control. Most of the work used the experimental approach (Akilli et al., 2004; Dargahi, 1989; Dey et al., 1995; Ettema et al., 2006; Kothyari et al., 1992; Melville and Raudkivi, 1977; Sarker, 1998). These studies have made impressive progress with respect to the maximum depth of scour and the flow patterns in response to changing hydraulic and structural conditions. Some detailed velocity measurements and τ_b estimates (Graf and Istiarto, 2002) are available; they are useful for validating numerical models. Commonly, the experimental approach suffers from the limitation that small-scale laboratory models are used, which gives rise to uncertain scaling effect.

In spite of extensive numerical studies conducted previously, there is a lack of direct comparisons of velocities in scour holes between models and experiments. Also, there is no systematic assessment of the suitability of existing methods for calculating τ_b. Furthermore, a need exits for improving computational efficiency of 3-D modelling. This has motivated the present study.

Some numerical studies (Akbari and Price, 2005; Lam et al., 2008; Lee and Yang, 2009; Papaioannou et al., 2006) considered low Reynolds number conditions, which does not

fully reflect the typically turbulent nature of flow around piers. Most of the existent numerical studies have not included a scour hole in the model channels (Palau-Salvador et al., 2008; Zou et al., 2008). They may not give satisfactory results in the presence of a scour hole. Most of the studies have not provided τ_b predictions.

So far only a limited number of numerical studies of 3-D flow around piers and local scour have been conducted. Using general CFD code, Richardson and Panchang (1998) predicted the flow within a scour hole, pointing out the importance of proper grid representations. The code has the limitation that it allows no flexibility in application to a mobile bed, as is typically the case for general CFD code. Yen et al. (2001) simulated the downward flow under the simplified condition of flat-bed geometry, and subsequently scaled up the computed velocities to obtain the corresponding jet flow in the scour hole. Such a treatment potentially contributes to uncertainties in the results. Previously, only very limited direct comparisons between predicted and measured velocities in a scour hole were made (Ali and Karim, 2002; Roulund et al., 2005; Salaheldin et al., 2004). Some of the problems encountered are unrealistic distributions of near-bed flow velocity and shear stress and the difficulty to obtain explicit predictions of the free surface.

Recently, a few numerical models with sophisticated formulations of relevant physical processes have been developed and applied to the problem of 3-D flow around piers with a scour module (Khosronejad et al., 2012; Nagata et al., 2005) or without a scour module. Nagata et al. (2005) considered the bed deformation around hydraulic structures including a bridge pier. They used the k-ε technique for turbulence closure. This technique is known to encounter difficulties in handling anisotropic turbulence, which is expected to be the case in the vicinity of piers.

On one hand, sophisticated models can incur prohibitively high computational costs and therefore are impractical for large-scale engineering applications (Khosronejad et al., 2012; Salaheldin et al., 2004). On the other hand, they do not necessarily produce reliable results for bridge piers of different geometric configurations, as in Khosronejad et al. (2012) who failed to deal with circular piers.

This study combines the efficient multi-layer modelling approach with non-hydrostatic pressure corrections. To the best of our knowledge, this represents a new approach to predicting flow in a scour hole. We verify the model results against the experimental data of Graf and Istiarto (2002). In the following, the methods for flow and shear stress computations are described. Then, the results, along with data comparison, are presented and discussed. This is followed by conclusions.

3.2 METHODOLOGIES

3.2.1 Model domain

Computations of flow around a bridge pier are setup for the same geometric and hydraulic conditions as the experiments of Graf and Istiarto (2002). This facilitates a direct comparison between the experimental and numerical data. The model domain is a channel of uniform width. There is a scour hole around the pier at the otherwise flat channel bed (Figure 3.1a). The pier is circular, with a diameter of $D = 0.15$ m (Figure 3.1b). At the flat-bottom level, the upstream and downstream edges of the scour hole are $L_2 = 0.45$ m and $L_3 = 1.05$ m, respectively, from the pier's centre (Figure 3.1b); the maximum width of the scour hole in the cross-channel direction cutting through the pier centre is 0.9 m (Figure 3.1a). The scour-hole surface upstream of the pier is a half cone. Upstream of the

pier, the surface's downward incline into the scour hole is 35°; the maximum depth of the scour hole is 0.25 m (Figure 3.1b). Downstream of the pier, the surface's upward incline is 11°; the maximum depth of the scour hole is 0.19 m. The lengths of the upstream and downstream flat-bottom channel sections are L_1 = 10.55 m and L_4 = 16.95 m, respectively. The entire channel has a uniform width of b = 2.45 m and an overall longitudinal slope of sl = 0.0016.

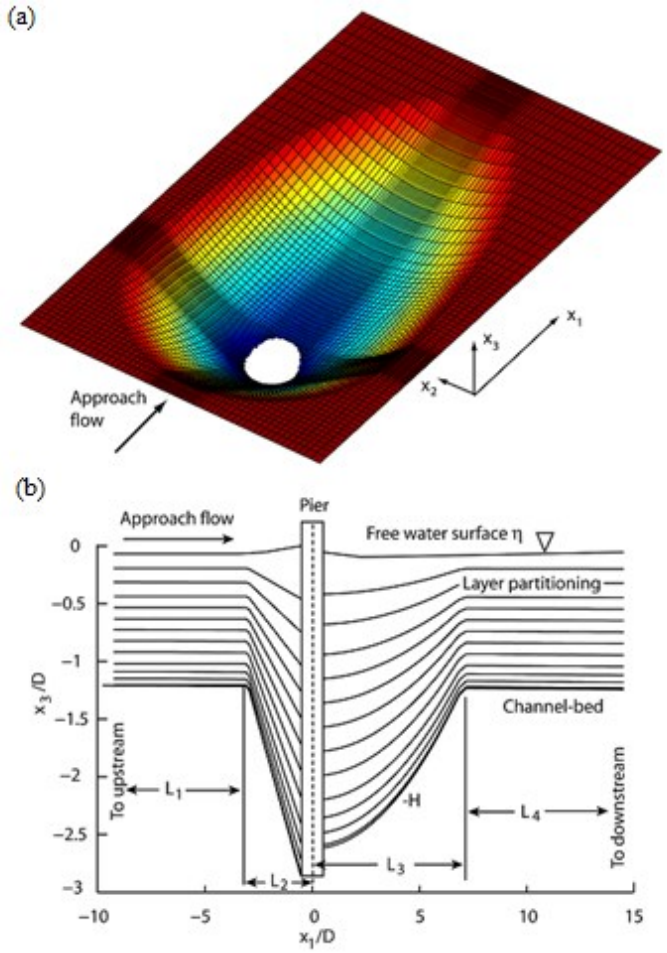

Figure 3.1 Model channel showing: (a) a scour hole at the channel-bed overlaid with computational meshes of varying sizes in the horizontal; (b) a vertical section along the channel centreline, the total depth of flow ($H + \eta$) being divided into multiple layers of varying thicknesses in the vertical.

The portion of the scour-hole surface upstream of the pier is a half-cone, expressed as

$$\left(\frac{x_3 - x_{3u}}{x_{3u}}\right)^2 = \left(\frac{x_1}{L_2}\right)^2 + \left(\frac{x_2}{L_2}\right)^2 \quad x_1 \le -D/2 \tag{3.1}$$

where x_{3u}= -0.30 m. The portion of the scour-hole surface downstream of the pier is a parabolic surface, given by

$$-\frac{x_3 - x_{3d}}{x_{3d}} = \left(\frac{x_1}{L_3}\right)^2 + \left(\frac{x_2}{L_2}\right)^2 \quad x_1 \ge D/2 \tag{3.2}$$

where x_{3d} = - 0.21 m. For $-D/2 < x_1 < D/2$, the scour-hole surface is a linear transition between Equations (3.1) and (3.2). L_1 is the length of approach flow channel section, L_2 is length of upstream scour hole, L_3 is length of downstream scour hole.

In the horizontal, the model channel is covered with non-uniform, structured meshes (Figure 3.1a) in order to obtain finite difference solutions to the governing equations given in Appendix A. Sizes of the meshes are as fine as 0.005 m in the vicinity of the pier within the scour; this is necessary to resolve expected large spatial variations in the velocity field. To reduce the computational costs, the mesh sizes are allowed to increase gradually (by a factor of less than or equal to 1.4 between adjacent meshes) for areas away from the pier. Areas far away from the scour hole are of less interest, and therefore they are covered with relatively coarse meshes, the sizes being 0.05 m as the maximum. For all the cells, the aspect ratio of the size in the along-channel direction to that in the cross-channel direction is limited to 10 as the maximum (Figure 3.1a). This limit on aspect ratios helps reduce flow distortion and computational errors.

In the vertical, the total depth of flow, $H + \eta$, is divided into a desired number of layers. The positions of these layers in the vertical change with time. This permits the computation of the layer-averaged velocity (u_j for the x_j direction, i= 1, 2, 3) for each of the layers (from

the equations given in Appendix A), and reveals the vertical structure of the velocity field. Figure 3.1b shows an example of $H + \eta$ being divided into thirteen layers. They decrease in thickness from $0.16(H + \eta)$ for the top layer to $0.01(H + \eta)$ for the bottom layer. The layer thickness is 0.075 m as the maximum for the top layer and 0.004 m as the maximum for the bottom layer. On one hand, higher resolutions for layers closer to the channel bed allow for resolving the important bottom boundary layer of the flow. On the other hand, the use of relatively thick layers closer to the free water surface, which are less important for scour modelling, reduces the total number of layers and hence enhances computational efficiency.

3.2.2 **Hydraulic conditions**

In Graf and Istiarto (2002), the bed sediments had a median grain size of $d_{50} = 2.1$ mm. This condition is applied as a dynamic condition in the model, in terms of an effective roughness height. The roughness height is calculated as $k_s = 2.1$ mm ($\approx d_{50}$). At the upstream end of the model channel (Figure 3.1a,b), open boundary condition of discharge must be prescribed in a model run. The discharge was derived from velocity profiles and the depth of flow measured from the upstream flat-bottom channel section (L_1 in Figure 3.1b), reported in Graf and Istiarto (2002). In that section, the depth of flow was 0.18 m, which was virtually uniform across the channel width. All the model runs to be described later used the derived discharge of $Q = 0.2$ m^3/s.

3.2.3 **Solution techniques**

The model channel with a scour hole at the channel-bed features large variations in bottom topography (Figure 3.1a,b). In order to realistically apply kinetic and dynamic

conditions at the varying bottom boundary, the σ-coordinate is used in the vertical. The transformation from the Cartesian coordinate in the vertical x_3 to the σ-coordinate is mathematically expressed as $\sigma = (x_3 - \eta)/(H+\eta)$, where $x_3 = \eta$ is the free water surface and $x_3 = -H$ is the channel-bed elevation. Both the varying free water surface and channel-bed are transformed into flat σ-coordinate surfaces, with $\sigma = 0$ and -1, respectively. Correspondingly, the continuity and momentum equations [Equations (A.1) and (A.2)] and subsequent relationships are transformed. Between the two coordinate surfaces of $\sigma = 0$ and -1, the partitioning of all the layers (Figure 3.1b) is at constant σ values.

For better computational efficiency, mode splitting technique is applied by which the flow field is split into depth-averaged velocity $<U_1, U_2>$ (external mode) and vertical velocity shear $<u_1 - U_1, u_2 - U_2>$ (internal mode). Computations of the modes and free surface elevations make use of the finite difference techniques. For numerical solutions of the external mode, the equations are integrated vertically over the total depth of flow, and the resultant equations are solved using a relatively small time step. The use of a small time step is to accommodate usually fast moving surface waves. For solutions of the internal mode, a larger time step is used to solve the layer-averaged equations, subtracted by the external mode. The mode splitting technique permits the calculation of the free surface elevation with little sacrifice in computational time by solving the volume transport separately from the vertical shear velocity.

The techniques described above use the hydrostatic approximation (Appendix A), which are computationally efficient. As flow acceleration in the vertical is expected to occur near the pier, locally the pressure distribution is non-hydrostatic As ECOMSED neglects the vertical acceleration of the flow, i.e. the pressure is considered to be hydrostatic, to retain

high computational efficiency and at the same time to achieve high accuracy, we allow for non-hydrostatic pressure corrections in the hydrodynamics predictions, which are made to all the layers at every time step during a simulation. Equations for the corrections are given in Appendix B.

3.2.4 **Model runs**

All the model runs commence from a state of rest. Dynamic and kinetic conditions applied are in model runs as follows: At the channel bed, the frictional force ($\vec{\tau}_b$) is parameterized using the quadratic law – that is $\vec{\tau}_b = C_D \rho |\vec{u}_b| \vec{u}_b$, where $\vec{u}_b = \langle u_1, u_2 \rangle$ at x_3 = -H is the bottom-layer velocity vector in the horizontal. At a solid sidewall, the flow is fully slippery. The velocity component normal to a solid wall is zero. At the upstream end of the model channel, discharge is prescribed; at the downstream end, water level is given.

The first series (or the A series) of model runs used a model channel of 29 m long (L_1 = 10.55 m, L_2 = 0.45 m, L_3 = 1.05 m and L_4 = 16.95 m, see Figure 3.1b), which match the dimensions of the laboratory channel of Graf and Istiarto (2002); the runs used 10 layers in the vertical. To reduce computational costs, the second series (or the B series) of model runs used a shortened downstream flat-bottom channel section (L_4 is shortened to 2.95 m); at the same time, the number of layers used was reduced to seven. The third series (or the C series) of model runs used a shortened upstream flat-bottom channel section (L_1 is shortened to 1.5 m), and 13 layers in the vertical in order to produce more detailed flow structure. Table 3.1 gives a summary of the mesh dimensions, layer thickness and time step, along with other physical and control parameters. In all the model runs, the eddy viscosity was given suitable values for numerical stability, and bottom friction was adjusted

for model calibration.

Table 3.1 Physical and control parameters for model runs. The three different values in parentheses for some of the parameters correspond to the first, second and third (or A, B and C) series of runs.

Parameters	Value	Unit
Length of the approach flow channel section (L_1)	(10.55, 10.55, 1.5)	m
Maximum length of the scour hole ($L_2 + L_3$)	1.50	m
Length of the downstream channel section (L_4)	(16.95, 2.95, 2.95)	m
Maximum width of the scour hole	0.90	m
Channel width (b)	2.45	m
Discharge (Q)	0.20	m^3/s
Equilibrium water level η (at the upstream end)	(0.01, 0.02, 0.03)	m
Water level η at downstream	(-0.02, 0.01, 0.03)	m
Overall bed slope	0.0016	
Grid dimension in the along-channel direction	(597, 317, 175)	
Grid dimension in the cross-channel direction	(65, 65, 108)	
Grid resolution in the along-channel direction	(1-5, 1-5, 0.5-5)	cm
Grid resolution in the cross-channel directions	(1-5, 1-5, 0.5-5)	cm
Number of layers in the vertical	(10, 7, 13)	
Minimum thickness of the bottom layer	(1.8, 0.54, 0.18)	cm
Aspect ratio of mesh in the horizontal	(5, 5, 10)	
Time step (Δt)	(0.001, 0.001, 0.0001)	sec
Simulation period	(70, 80, 80)	sec
Bottom drag coefficient ($C_D \times 10^3$)	(2.5, 0.625, 0.625)	
Bed roughness height (k_s)	0.0021	m
Horizontal eddy viscosity (A_M)	0.05	m^2/s
Gravitational acceleration (g)	9.81	m/s^2
Ramping period	0	sec
Criterion for convergence	10^{-6}	
Pier diameter (D)	15	cm
Sediment median grain size (d_{50})	2.1	mm

3.2.5 **Bed shear stress**

We express the bed shear stress ($\vec{\tau}_b$) in terms of the resolved velocity field from hydrodynamics modelling. The three velocity components (u_1, u_2, u_3) are illustrated in Figure 3.2. They are obtained from hydrodynamics computations described in the Solution techniques and Model runs Sections. Let u_* denote the friction velocity, defined by

$$\left|\vec{\tau}_b\right| = \rho u_*^2 \tag{3.3}$$

There are four different methods for calculating the bed shear stress: 1) depth-averaged flow method, 2) eddy viscosity method, 3) the law of the wall method, and 4) Reynolds shear stress method. In this study, the logarithmic law of the wall method is used to calculate the bed shear stress. According to the logarithmic law of the wall, the friction velocity is related to the tangential velocity as

$$\frac{u_{p1}}{u_*} = \begin{cases} \frac{1}{\kappa}\ln\left(y^+ / {k_s}^+\right) + 8.5 & , \quad \text{when } y^+ \succ 11.53 \\ y^+ & , \quad \text{when } \mathrm{y}^+ \le 11.53 \end{cases} \tag{3.4}$$

where $y^+ = yu_*/v$ is the non-dimensional wall distance, y is the shortest distance from the channel bed to the velocity point in question (from p to c in Figure 3.2), k_s^+ ($= k_s u_*/v$) is the roughness Reynolds number, and u_{p1} is the component of the vector $<u_1,0,u_3>$ in the direction parallel to the channel-bed surface (Figure 3.2). The coordinates of point c are denoted by (x_{1c}, x_{2c}, x_{3c}). u_{p1} is given by

$$u_{p1} = \frac{u_1 \Delta x_1 + u_3 \Delta x_3}{\sqrt{{\Delta x_1}^2 + {\Delta x_3}^2}} \tag{3.5}$$

In the x_2-direction, the calculations are similar, with the substitution of u_{p2} for u_{p1}. u_{p2} is the component of the velocity vector $<0, u_2, u_3>$, given by

$$u_{p2} = \frac{u_2 \Delta x_2 + u_3 \Delta x_3}{\sqrt{\Delta x_2{}^2 + \Delta x_3{}^2}} \tag{3.6}$$

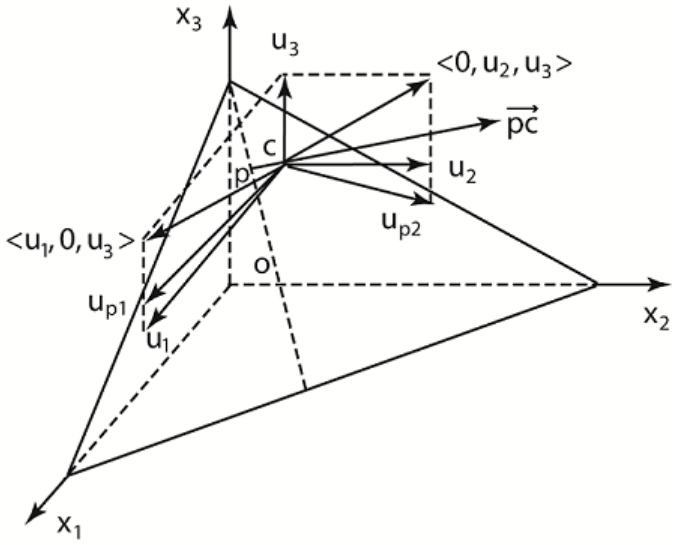

Figure 3.2 Projections of the velocity vector <u_1, u_2, u_3>. Point c is the centre of a computational cell. The line through c and p is normal to the bed surface at point p. u_{p1} indicates the magnitude of the vector as the projection of <u_1, 0, u_3> in the direction parallel to the tangent line of the bed surface at point p. u_{p2} indicates the magnitude of the velocity vector as the projection of <0, u_2, u_3>.

Note that inside the scour hole, Δx_3 is significant (Figure 3.1a), meaning that there is a large difference in bed elevation between adjacent cells. It is negligible outside, where one recovers $u_{p1} = u_1$ and $u_{p2} = u_2$.

Consider a grid on the bed surface. Let (x_{1o}, x_{2o}, x_{3o}) denote the coordinates of that grid's centre. Let (x_{1e}, x_{2e}, x_{3e}) denotes the coordinates of its adjacent grid in the x_1-direciton, and (x_{1n}, x_{2n}, x_{3n}) denote the coordinates of its adjacent grid in the x_2-direciton. The three points determine a plane. An equation of the plane can be written as $Ax_1 + Bx_2 + Cx_3 + 1 = 0$, where A, B, C are determinants:

$$A = \frac{-1}{D}\begin{vmatrix} 1 & x_{2o} & x_{3o} \\ 1 & x_{2e} & x_{3e} \\ 1 & x_{2n} & x_{3n} \end{vmatrix} \tag{3.7}$$

$$B = \frac{-1}{D}\begin{vmatrix} x_{1o} & 1 & x_{3o} \\ x_{1e} & 1 & x_{3e} \\ x_{1n} & 1 & x_{3n} \end{vmatrix} \tag{3.8}$$

$$C = \frac{-1}{D}\begin{vmatrix} x_{1o} & x_{2o} & 1 \\ x_{1e} & x_{2e} & 1 \\ x_{1n} & x_{2n} & 1 \end{vmatrix} \tag{3.9}$$

$$D = \begin{vmatrix} x_{1o} & x_{2o} & x_{3o} \\ x_{1e} & x_{2e} & x_{3e} \\ x_{1n} & x_{2n} & x_{3n} \end{vmatrix} \tag{3.10}$$

The determinant D is non-zero. The shortest distance y from c to the plane (or to point p, see Figure 3.2) is

$$y = \frac{\left|Ax_{1c} + Bx_{2c} + Cx_{3c} + 1\right|}{\sqrt{A^2 + B^2 + C^2}} \tag{3.11}$$

3.3 RESULTS AND DISCUSSION

The first and second series (or A and B series) of model runs (Table 3.1) served to test the functioning of the hydrodynamics model with respect to numerical stability, end (lateral open boundary) effects and choice of time step for integration. An examination of the results (not shown) for these runs indicates that the numerical solutions converge, no significant disturbances bounce back from the downstream end of the model channel, and time step used is optimal. The third series (or C series) of model runs are computationally efficient because the grid dimensions are relatively small. The results of velocity field and free surface elevation for the third series of model runs are presented and discussed in the

following.

3.3.1 **Flow velocities in the horizontal**

The predicted flow velocities in the horizontal are shown as vectors in Figure 3.3a for the surface layer and in Figure 3.3b for the 2nd layer above the channel-bed. The partitioning of layers is shown in Figure 3.1b. In Figure 3.3a, the flow approaches the pier at a longitudinal velocity of u_1 = 0.45 m/s (at x_1/D < -10) and rapidly slows down to u_1 = 0.14 m/s (at $x_1/D \approx$ -0.55). Water flows around the pier, with a transversal velocity of up to u_2= 0.26 m/s. After the flow passes the pier, the longitudinal velocities range from-0.14 m/s (flow reversal) in the vicinity of the pier to 0.44 m/s far from it; the transversal velocities vary from -0.17 to 0.17 m/s.

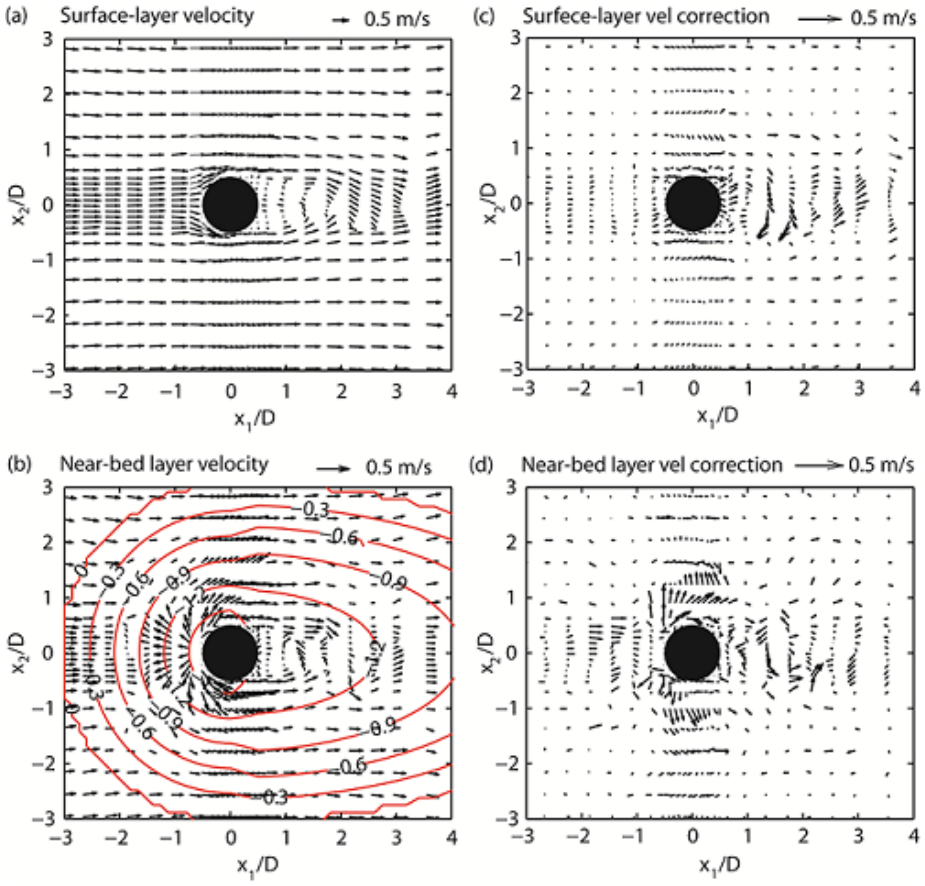

Figure 3.3 Predicted flow velocities in the horizontal [panels (a) and (b)] and velocity corrections due to non-hydrostatic pressure [panels (c) and (d)]. Panels (a) and (c) are for the surface layer [$-0.16 \leq x_3/(H+\eta) \leq 0$]. Panels (b) and (d) are for the 2nd layer above the channel-bed [$-0.99 \leq x_3/(H+\eta) \leq -0.95$]. The total depth of flow ($H+\eta$) varies from 18 to 46.8 cm. Every third vectors are plotted. In panel (b), the contour lines indicate scour-hole depths normalized by the pier diameter. The upstream edge of the scour hole is located at $x_1/D = -3$.

Flow wakes are visible, circulating in the clockwise and counter-clockwise directions (Figure 3.3a). The associated wake vortices drift downstream owing to the mean flow, which can lift up bed sediments on the downstream side of the pier, sweep them downstream and produce local scour. The depth of local scour should decrease as wake vortices weaken with increasing distance from the pier. The wakes have a total width approximately equal to the diameter of the pier, since the Reynolds number is high. If the Reynolds number is low, flow separation is known to delay, resulting in narrower wakes

(Kravchenko and Moin, 2000).

In Figure 3.3b, the flow approaching the scour hole has a longitudinal velocity of u_1 = 0.24 m/s (at x_1/D = -5.9). As expected, the velocity drops to almost zero on the upstream face of the pier. Upstream of the pier, the longitudinal velocity is negative, ranging from -0.05 to -0.35 m/s (at -1.53 <x_1/D < -0.5), meaning that flow reversal occurs in the scour hole; the transversal velocity ranges from u_2= -0.3 to 0.3 m/s. Downstream of the pier, flow wakes form, where water circulates in the clockwise and counter-clockwise directions. The longitudinal velocity ranges from -0.12 m/s near the pier to 0.25 m/s far from it; the transversal velocity is between -0.15 and 0.15 m/s. The flow velocity vectors shown in Figure 3.3a,b are steady-state distributions as a result of advection, flow-pier interaction, turbulent mixing and non-hydrostatic pressure.

3.3.2 **Flow velocity corrections**

Flow velocities calculated using the hydrostatic approximation (Appendix A) need to be corrected to allow for the effect of non-hydrostatic pressure (Appendix B).In Figure 3.3c and Figure 3.3d, we plot velocity correction vectors as the result of subtracting non-hydrostatic predictions of velocity from hydrostatic predictions. From the free surface (Figure 3.3c) to near the bottom (Figure 3.3d), the corrections are significant in the wake region within a longitudinal distance three times the pier diameter from the pier. In the surface layer (Figure 3.3a), the wake region corrections have a maximum speed of 0.17 m/s in the longitudinal direction and 0.26 m/s in the transverse direction. The speed of 0.17 m/s amounts to 38% of the depth-averaged speed of 0.45 m/s of the approach flow. Corrections for the other regions around the pier appear to be insignificant, meaning that the pressure distributions there are hydrostatic.

Within the scour hole, non-hydrostatic pressure-induced velocities are significant all around the pier (Figure 3.3d). Within a radial distance of one and a half to two times the pier diameter, velocity correction vectors are seen to have a significant magnitude. The maximum magnitude is as large as 0.16 m/s in the longitudinal direction and 0.19 m/s in the transverse direction. More importantly, the velocity corrections give rise to eddy motions on both the upstream and downstream sides of the pier. The resultant vorticity contributes to the local bed shear stress and can make it to exceed the threshold for movement of bed sediments of given grain size. On the flanks of the pier, non-hydrostatic pressure causes divergent flow as strong as 0.12 m/s. This directly increases the scouring of the pier base.

It is important to note that the formulation of velocity corrections using Equations (B.1) – (B.3) is much more efficient than general purpose CFD code as those code use the primitive Navior Stokes equations, which results in high computational costs especially in applications at the field scale. The formulation can easily be incorporated into hydrostatic hydrodynamics models for efficient computations of sediment transport and bed scour, whereas general CFD code typically does not provide sediment scour computations.

3.3.3 **Flow velocities in the vertical**

In order to reveal the vertical structure of flow, we plot velocity vectors at the vertical cross section along the channel centreline (Figure 3.4a-d). The vertical structures are significant from predictions with the hydrostatic pressure approximation (Figure 3.4a,b) as well as with non-hydrostatic pressure corrections (Figure 3.4c,d). For example, far upstream of the scour hole ($x_1/D < -4$) where the channel-bed is flat, velocity vectors are parallel to the bed with negligible vertical velocities. The longitudinal velocity varies with

height above the bed, giving rise to typical boundary-layer velocity profiles (Figure 3.4a,c). Their shape does not change much and the pressure distribution is hydrostatic until the flow reaches the scour hole at x_1/D = -3. The velocity structures cannot be simulated using depth-averaged models.

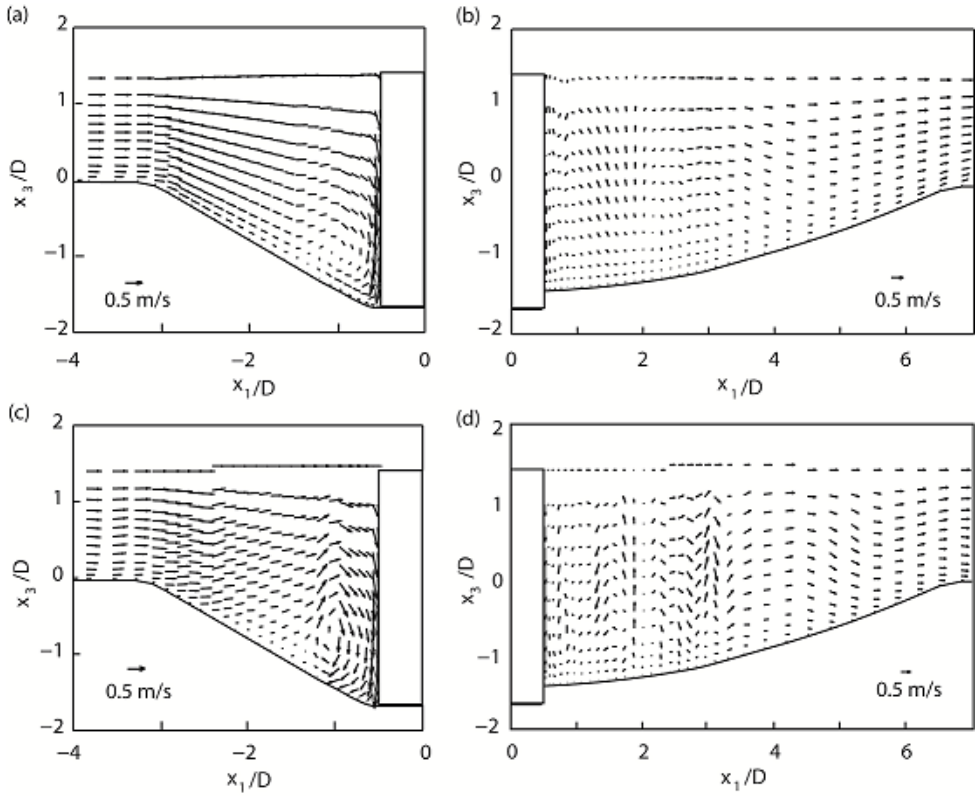

Figure 3.4 Vertical cross sections along the channel centreline (the same as Figure 3.3a,b at x_2/D = 0 and Figure 3.1b), showing predicted velocity vectors on the basis of hydrostatic pressure [panels (a) and (b)] and non-hydrostatic pressure [panels (c) and (d)].

Within the scour hole upstream of the pier, the most striking feature is the appearance of downward velocities in the vertical (Figure 3.4a,c). They are intensified just upstream of the pier, because the pier obstructs the flow in the longitudinal direction. The intensification can simply be explained using the principle of continuity. On the basis of the hydrostatic approximation, the flow circulation upstream of the pier shows rather weak vortices (Figure 3.4a). Non-hydrostatic pressure corrections lead to stronger flow and

vortices (Figure 3.4c).

Tison (1961) suggested that downward velocity results from the horizontal curvature of the streamline in front of the pier and the reduction of velocity near the bed by friction. Downward velocity gives rise to horseshoe vortices wrapping around the pier and can effectively initiate a scour hole, with the potential to cause bridge failures. The longitudinal velocity is shown to decrease toward the pier (Figure 3.4a,c), and the flow passes around the pier at all depths (Figure 3.3a,b).

The downward velocities just upstream of the pier (at a distance of 0.17*D* from the pier nose) appear to be over-predicted, being about 1.13 (Figure 3.4a) and 1.17 (Figure 3.4c) times the depth-averaged velocity (0.45 m/s) of the approach flow, compared to the literature value of 0.8 times (Copp and Johnson, 1987; Melville, 1988). Possibly, the overprediction results from the approximation that the pier is considered to have a fully slippery surface. In principle, the prediction errors can be alleviated by applying more realistic condition that the surface is partially slippery or non-slippery. The application will require the use of smaller grid sizes as well as smaller time step.

Relatively speaking, the flow is weak downstream of the pier (Figure 3.4b,d). Next to the pier, the vertical velocity is mostly (in more than half the total depth of flow) in the downward direction, with a magnitude of 0.09 m/s (Figure 3.4b) and 0.16 m/s (Figure 3.4d), whereas the longitudinal velocity of lesser strength is in the backward direction (flow reversal). A comparison between Figure 3.4b and Figure 3.4d shows that non-hydrostatic pressure causes multiple eddies downstream of the pier. The associated water circulations in the upward and downward directions can stir up bed sediments. Non-hydrostatic pressure corrections are important for simulating the flow field in a scour hole.

3.3.4 **Comparison of velocities between predictions and measurements**

For a series of locations at the vertical cross section along the channel centreline (Figure 3.4a-d), predicted longitudinal velocities are extracted from the model results. The predicted velocities are compared with laboratory measurements by Graf and Istiarto (2002) from corresponding locations (Figure 3.5a,b). Almost all the comparison data are from within the scour hole (Figure 3.1b). The overall comparison is reasonable (Figure 3.5b).The introduction of non-hydrostatic pressure corrections lead to an improved comparison (Figure 3.5b) from the results of hydrostatic predictions (Figure 3.5a). Note that the discrepancies are associated mainly with near zero velocities. The comparison between the predictions and measurements is particularly good with regards to strong velocities. This is the most significant for the problem of bedload transport and scour.

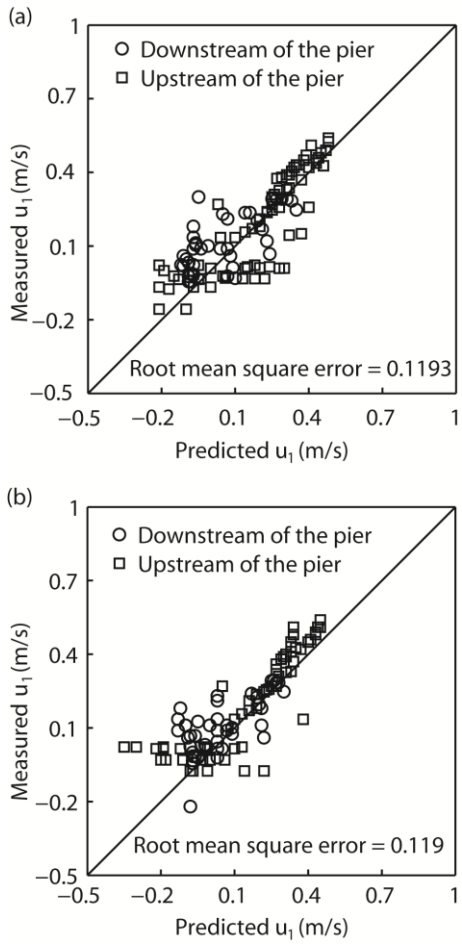

Figure 3.5 Comparison of predicted longitudinal velocities with experimental data of Graf and Istiarto (2002): (a) predictions based on the hydrostatic pressure assumption, and (b) predictions with the effect of non-hydrostatic pressure.

3.3.5 **Bed shear stress**

The bed shear stress τ_b [Equations (3.3) and (3.4)] has been calculated using predicted velocities from the 2nd, 3rd and 4th layer above the channel-bed (Figure 3.1b). These three layers have typical wall distances of $30 < y^+ < 150$, $150 < y^+ < 350$ and $300 < y^+ < 800$, respectively. The results of τ_b are shown as contours in Figure 3.6a-f. A comparison between the panels on the left and the right shows the effect of non-hydrostatic pressure

corrections. With non-hydrostatic pressure corrections, the results on the basis of the velocities of the 4th layer above the bed show less fluctuating features (Figure 3.6f), and we consider them to be more reliable.

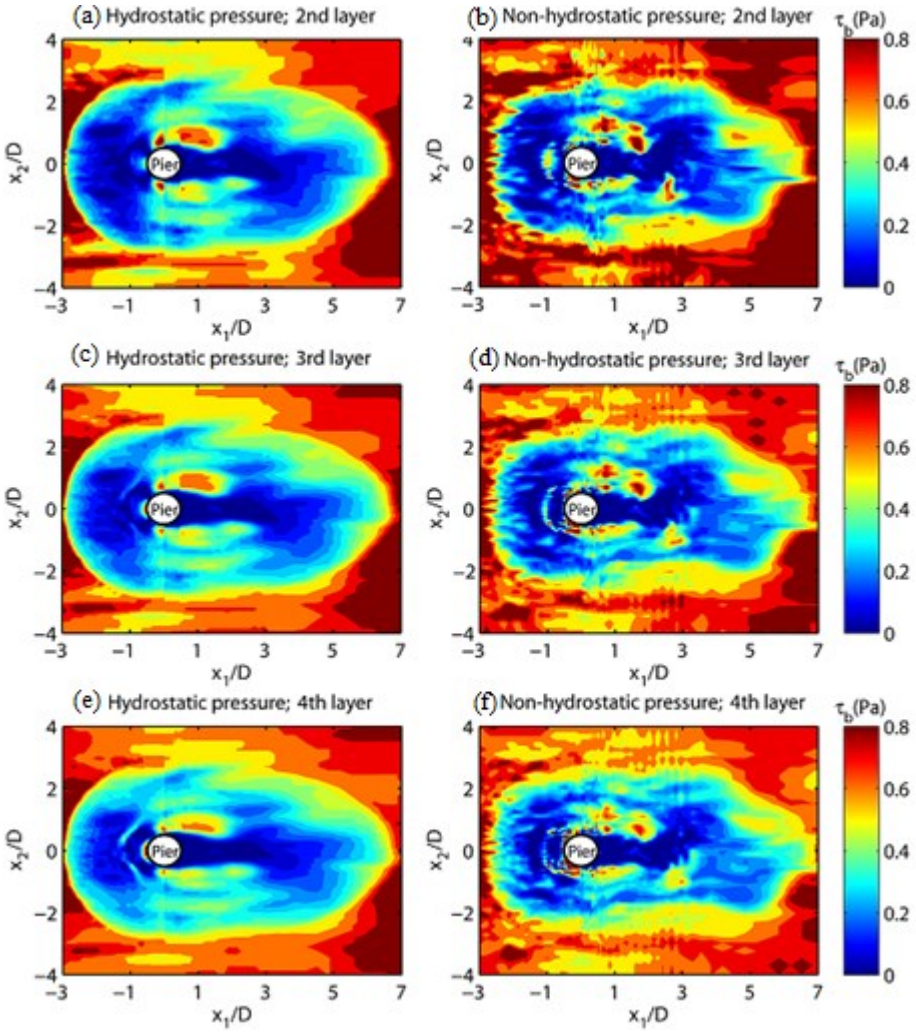

Figure 3.6 Contours of bed shear stress [Equations (3.3) and (3.4)] based on predicted velocity from the 2nd layer [(a) and (b)], 3rd layer [(c) and (d)] and 4th layer [(e) and (f)] above the bed. The predictions shown in the panels on the left use the hydrostatic pressure approximation. The predictions shown in the panels on the right uses non-hydrostatic pressure corrections.

In the approach region (the L_1 section in Figure 3.1b), τ_b is more or less uniform, with an average value of about 0.81 Pa (Table 3.2). Near the upstream edge of the scour hole (at x_1/D = -3), the local τ_b increases from the average value by about 50% (without non-hydrostatic pressure corrections) and 20% (with non-hydrostatic pressure corrections). The increase is probably due to the response to horizontal and vertical acceleration on entering the scour hole. With non-hydrostatic pressure corrections, predictions of the average bed shear stress and local maximum compare well with the measurements of Graf and Istiarto (2002), and the predictions are rather similar whether the 2nd, 3rd or 4th layer velocities are used. The use of non-hydrostatic pressure renders corrections of 20% to the local maximum (Table 3.2).

Table 3.2 Calculated and measured bed shear stresses in the approach region.

	Hydrostatic run			Non-hydrostatic run			Measurements
Layer above the bed	2nd	3rd	4th	2nd	3rd	4th	Graf and Istiarto (2002)
Average τ_b (Pa)	0.75	0.82	0.82	0.83	0.81	0.81	0.6 - 1.0
Local maximum τ_b (Pa)	1.25	1.2	1.2	1.0	1.0	0.91	

In the region of the scour hole (Figure 3.1a,b), τ_b varies significantly with space (Figure 3.6a-f). Upstream the nose of the pier (x_1/D < -0.5), τ_b values are low relative to the average value in the approach region. In fact, τ_b drops non-linearly from the upstream edge of the scour hole on entering the scour hole (Figure 3.7); this is consistent with the experimental data of Graf and Istiarto (2002). Specifically along the centreline, τ_b is approximately 1 Pa at (with non-hydrostatic pressure corrections) at $x_1/D \approx$ -3 and drops to almost zero at x_1/D = -1.35.

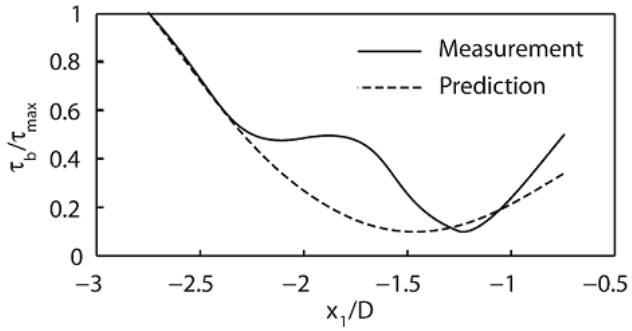

Figure 3.7 Reduction of the bed shear stress τb in the scour hole compared to its maximum value τ_{max} in the approach flow.

Inside the scour hole (Figure 3.1a,b), on each lateral side of the pier, there is a region of relatively high bed shear stress, which stretches three and a half times the pier diameter toward downstream (or from x_1/D = -0.5 to x_1/D = 2.93). The two regions are not symmetrical about the channel centreline. On the basis of the flow velocities from the 4th layer (Figure 3.6f), the maximum τ_b is 4.8 Pa, which occurs near the pier surface (x_1/D = -0.37 and x_2/D = 0.52).

In the wake region (at $0.5 < x_1/D < 2.93$ and $-0.5 < x_2/D < 0.5$), τ_b values are also low, which is consistent with the finding of Graf and Istiarto (2002). The bed shear stress increases to an average value of 0.7 Pa (Figure 3.6f) at the downstream edge of the scour hole, and then further decreases to about 0.5 Pa toward downstream.

It can be seen that the contours of bed shear stress using non-hydrostatic pressure corrections is asymmetric. The reason is that the flow field is asymmetric around the pier. According to Schewe (1983) and Singh and Mittal (2005), the change in the flow from symmetric to asymmetric distributions is accompanied by the generation of circulation around the cylinder. Asymmetric flow separation occurs with the generation of non-zero steady lift of both positive and negative sign (Schewe, 1983). This phenomenon is marked by two discontinuous transitions, i.e. drop and jump in C_D and St. After the first transition,

the flow achieves a bistable asymmetric state consisting of two stable states corresponding to positive and negative lift force (Spingh and Mittal, 2005). The second transition is characterised by further jump and drop in St and C_D and the abrupt disappearance of the steady lift. This phenomena occurs at the Reynolds number less than 10^5 (Spingh and Mittal, 2005). The asymmetric flow results in asymmetric bed shear stress contour. Also, in case of a mobile bed, the symmetric flow has an important effect on the asymmetric shape of the scour hole.

3.4 CONCLUSION

We have extended a 3-D multi-layer hydrodynamics model to include non-hydrostatic pressure corrections for efficient simulations of flow passing around a pier in a scour hole. We have investigated the distribution of the bed shear stress. From this study, we can draw the following conclusions:

1) Predicted velocities compare well with the experimental data of Graf and Istiarto (2002). The good comparison has been accomplished through the use of a proper bed friction coefficient, along with sufficient resolutions of the varying geometry of the scour hole in the horizontal and the vertical.
2) The law of wall method for calculating the bed shear stress renders results consistent with the experimental data. This method captures well the non-linear drop in the bed shear stress in the scour hole from its value in the approach region. This method can easily be incorporated into numerical models for sediment transport and scour computations.

3) When applying the law of the wall, one should use near-bed ($300 < y^+ < 800$) velocities as opposed to bottom-layer velocities. The use of the latter appears to underestimate the bed shear stress and produce results with more fluctuating features.

4) The model results show a number of realistic flow features, including strong downward flow adjacent to the upstream nose of the pier, circulation (in the vertical plane) in the scour hole upstream of the pier, and formation of eddies downstream of the pier in both the vertical and horizontal planes. These motions reflect some aspects of turbulent vortex flow around a pier.

5) The downward flow next to the upstream nose of the pier has been over-predicted. This is probably due to the use of fully-slippery condition on the pier surface. An improvement can be made by treating the surface as being partially-slippery.

Chapter 4 An efficient multi-layer model for pier scour computations

Summary: Pier scour has caused bridge failures with catastrophic consequences. This study aims to develop and verify a mathematical model for pier-scour predictions. A new approach is taken, which combines shallow-water equations with non-hydrostatic pressure corrections and non-uniform mesh in the horizontal with terrain-following layers in the vertical. This approach significantly improves computational efficiency from the conventional CFD approach. We conclude that, emerging from the lateral sides of a pier (cylinder), scour deepens while the patterns migrate upstream toward the pier's upstream nose. On the upstream side, scour continues to grow until the bed slope reaches the angle of repose of sediments. On the downstream side, scour grows until equilibrium is reached. The scour hole is shallower downstream than upstream of the pier. The presence of the pier causes a strong down flow near its upstream nose, a strong vortex at its foot on the upstream side and a weak vortex on the downstream side. The predicted flow velocity and scour depth agree well with measurements. The terrain-following layer feature is particularly useful for scour computations; the high efficiency makes the model practical for field scale applications, which are highly relevant to improved design of pier foundations and pier scour control.

4.1 INTRODUCTION

Flow-induced sediment scour around the base of bridge piers (Figure 4.1) have been the

major cause of bridge failures (Melville and Coleman, 2000). Clearly, reliable predictions of pier scour are of relevance to the safe and cost-effective design of pier foundations. Water flow approaching a pier generates complicated three-dimensional turbulent motions (Melville and Coleman, 2000). Their interaction with an erodible channel-bed is even more complicated, making pier scour notoriously difficult to predict.

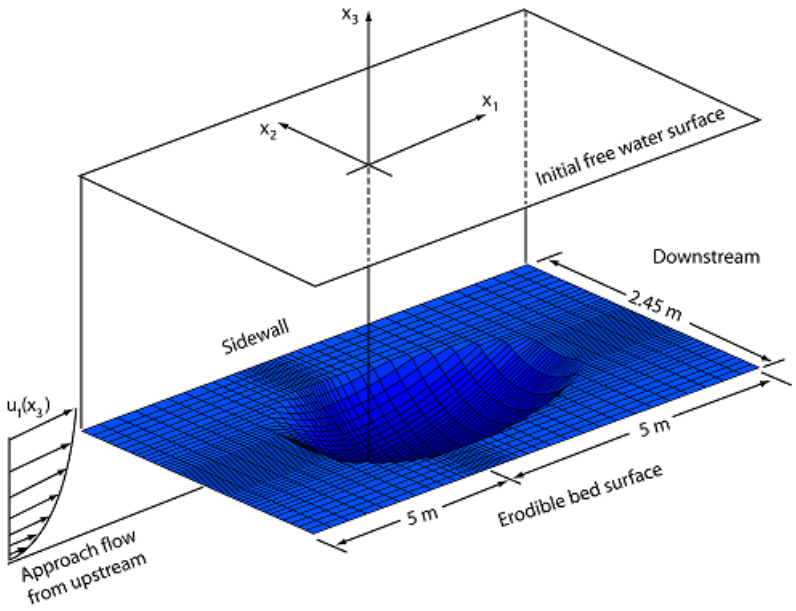

Figure 4.1 3-D diagram of the model channel. At the middle a circular pier of 0.15 m in diameter stands vertically (omitted for clear visualisation).The x_3-axis passes through the centre of the pier. The channel sections upstream and downstream of the pier are 5 m long (unless otherwise indicated). The channel-bed is flat and has a slope of 0.0016 initially but evolves during scouring. The channel is covered with non-uniform mesh in the horizontal. The approach flow has a prescribed profile, giving a depth-averaged velocity of 0.426 m/s and a discharge of 0.2 m^3/s.

Previous studies of pier scour have taken mostly the experimental approach. The main results are empirical formulae for determining such quantities as the maximum scour depth and bed evolution for given input parameters including depth-averaged approach velocity, pier diameter (D) and sediment grain size. The major drawback of this approach is that

experiments are expensive and time consuming to perform, and have uncertain scaling effect due to the use of typically small-scale laboratory models. In an assessment of commonly used scour depth formulae, Johnson (1995) emphasised a need for improvement. As an example, using the parameters given in Graf and Istiarto (2002) as input, we obtain inconsistent values for the maximum scour depth, equal to 1.93D, 1.47D and 1.87D, respectively, from the formulae of Melville and Chiew (1999), FHWA (2001) and Sheppard et al. (2004). Mathematical modelling is an alternative approach to the complicated pier scour problem.

The purpose of this paper is to develop an efficient computational model for predicting flow around piers and resultant scour and to verify the predictions using available experimental data. Although extensive modelling studies of flow around piers have been reported in the literature, many issues remain to be resolved. For example, most investigators have ignored the presence of a scour hole in their model domains; their focus was limited to the flow field or pier vibrations, without computations of bed shear stress, bedload or sediment scour, as is the case in Catalano et al. (2003), Richardson and Panchang (1998) and Salaheldin et al. (2004). Some investigators (Akbari and Price, 2005; Lam et al., 2008; Papaioannou et al., 2006) have considered the case of low Reynolds numbers, which does not fully reflect the turbulent nature of flow around piers. Roulund et al. (2005) computed the flow field and scour around a cylinder, using the rigid-lid approximation in their model, which is invalid at high Froude numbers.

Other issues with some existing models include prohibitively high computational costs, making it impractical to apply on field scale. Such models include Reynolds-averaged Navier-Stokes equation models (Dehghani et al., 2012; Nagata et al., 2005; Olsen and

Melaaen, 1993; Khosronejad et al., 2012) and large eddy simulation models (Yen et al., 2001). A need exists for improving computational efficiency as well as prediction accuracy. There are examples of pier scour modelling (Nagata et al., 2005), where the k-ε model is used for turbulence closure, which is known to encounter difficulties in accurately handling anisotropic turbulence expected in the vicinity of piers. Khosronejad et al. (2012) reported difficulties in obtaining accurate scour depth around a circular cylinder.

One way to reduce computational costs is to use non-uniform mesh, covering near-pier area with relatively fine spatial resolutions and the rest of the model domain with coarse resolutions, as in Baranya et al. (2013) among others. Fine resolutions around piers helps improve prediction accuracy. This paper combines efficient multi-layer modelling techniques with the beneficial use of non-uniform mesh. In the following, we describe the methodology for hydrodynamics and scour computations and simulation setup (Section 4.2), present and discuss the results of velocity and scour depth (Section 4.3), and draw conclusions (Section 4.4).

4.2 METHODOLOGY

4.2.1 Hydrodynamics equations and boundary conditions

An existing shallow-water equation model (HydroQual, 2002) is to be extended to include non-hydrostatic pressure, bedload and bed level change. In shallow water equations, the local rate of change of the water surface elevation comes from two contributions: advection and convergence. In the momentum balance of the flow, the distribution of pressure is hydrostatic. The shallow-water model equations are

$$\partial u_j / \partial x_j = 0; \quad j = 1,2,3 \tag{4.1}$$

$$\frac{\partial u_i}{\partial t}+\frac{\partial\left(u_i u_j\right)}{\partial x_j}=-\frac{1}{\rho}\frac{\partial p}{\partial x_i}+\frac{\partial}{\partial x_3}\left(K_M\frac{\partial u_i}{\partial x_3}\right)+F_i\,;\quad i=1,2\,;\quad j=1,2 \tag{4.2}$$

$$-\partial p/\partial x_3=\rho g \tag{4.3}$$

$$\partial\eta/\partial t+\partial\left(\eta u_i\right)/\partial x_i=0 \tag{4.4}$$

where the velocity is the Reynolds-averaged velocity, and η is the free surface elevation.

The horizontal diffusion due to subgrid-scale motions is given by

$$F_i=\frac{\partial}{\partial x_j}\left[A_M\left(\frac{\partial u_i}{\partial x_j}+\frac{\partial u_j}{\partial x_i}\right)\right];\quad i=1,2\,;\quad j=1,2 \tag{4.5}$$

where A_M is horizontal eddy viscosity , K_M is vertical eddy viscosity and F_i is horizontal diffusion term which is required to damp small-scale noise in the predicted velocity field. Using Smagorinsky's (1963) scheme, the horizontal eddy viscosity is related to mesh sizes (Figure 4.1) and mean flow strain rate. Using the scheme of Mellor and Yamada (1982), the vertical eddy viscosity is related to turbulence kinetic energy and turbulence macro-scale; these two quantities are predicted using unsteady advection-diffusion equations.

Dynamic and kinematic conditions are specified at the channel boundaries: At the free surface, the shear stress is zero; fluid particles on the surface will stay on the surface all the time. At the channel bed, the bed shear stress is specified in terms of bottom-layer velocity according to the quadratic law $\tau_b=C_D\rho|u_b|u_b$; the normal component of the velocity vector is zero. On the channel and pier sidewalls, due to excessively high computational costs, it is difficult to have mesh resolutions fine enough to resolve the associated boundary layers; therefore, the sidewalls are considered to be fully slippery, and the velocity component normal to the sidewalls is zero.

4.2.2 **Solution techniques**

The hydrodynamic computations make use of the terrain-following σ-coordinates in the vertical, which is particularly useful for simulating the development of a scour hole. Advantages include a realistic implementation of the kinetic and dynamic conditions at the varying bottom boundary. The transformation from the Cartesian coordinate in the vertical x_3 to the σ-coordinate is mathematically expressed as $\sigma = (x_3 - \eta)/(H + \eta)$. Both the varying free surface and channel-bed Figure 4.1 are transformed into coordinate surfaces: $\sigma = 0$ and -1, respectively. Correspondingly, Equations (4.1)–(4.5) and relevant relationships are transformed. Between the two σ coordinate surfaces, the water column is partitioned into multiple layers at constant σ values.

For better computational efficiency, mode splitting technique is applied by which the flow field is split into depth-averaged velocity (external mode) and vertical velocity shear (internal mode). Computations of the modes and free surface make use of the finite difference techniques.

The use of the hydrostatic pressure approximation [Equation (4.3)] is computationally efficient but needs to be improved in order to handle significant vertical motions and non-hydrostatic pressure distributions expected in a scour hole. An improvement is made by introducing non-hydrostatic pressure corrections.

4.2.3 **Non-hydrostatic pressure corrections**

Consider the velocity field obtained from the computations mentioned above as provisional flow field $(\tilde{u}_1, \tilde{u}_2, \tilde{u}_3)$.Following Casulli (1999), we correct the provisional solution as follows

$$u_1(i+1) = \tilde{u}_1(i+1) - \psi \frac{\Delta t}{\Delta x_1}\left[m(i+1) - m(i)\right] \tag{4.6}$$

$$u_2(j+1) = \tilde{u}_2(j+1) - \psi \frac{\Delta t}{\Delta x_2}\left[m(j+1) - m(j)\right] \tag{4.7}$$

$$u_3(k+1) = \tilde{u}_3(k+1) - \psi \frac{\Delta t}{\Delta x_3}\left[m(k+1) - m(k)\right] \tag{4.8}$$

where m is the non-hydrostatic pressure correction, Δt is the time interval, $\tilde{u}$ is the provisional velocity. The implicitness factor ψ ranges from 0.5 to 1 for stability ($\psi = 0.5$ in this study, according to Casulli and Cattani, 1994).

Substituting Equations (4.6)–(4.8) into the finite difference version of the continuity equation [Equation (4.1)] yields a seven diagonal linear system for the non-hydrostatic pressure. The system ensures the conservation of mass, which is a constraint to the seven diagonal linear system. This system is symmetric and has positive definition. The system can be solved for the corrected velocities by using preconditioned conjugate gradient iterations until residual norm is smaller than a given tolerance. With regards to boundary conditions on the channel sidewalls and pier's surface, the non-hydrostatic pressure is such that the normal flux is zero. At open boundaries, the non-hydrostatic pressure is specified. At the free surface, the non-hydrostatic pressure is zero.

Once the non-hydrostatic pressure is solved, the velocities are updated using Equations (4.6)–(4.8). At the same time, the free surface elevation is updated as below

$$\eta = \tilde{\eta} + m / g \tag{4.9}$$

where m is evaluated at the bottom layer, $\tilde{\eta}$ is provisional free surface elevation. For more details, refer to (Casulli, 1999).

4.2.4 **Bedload**

The bed shear stress is a key input to bedload predictions. It is calculated using the wall function because the function is reliable and is easy to implement in numerical modelling. The bed shear stress is expressed as

$$\tau_b = \rho u_*^2 \tag{4.10}$$

For the wall distance $y^+ > 11.53$, u_* is determined implicitly f%rom

$$\frac{u_p}{u_*} = \frac{1}{\kappa}\ln\left(\frac{y^+}{k_s^+}\right) + 8.5 \tag{4.11}$$

Test simulations indicate that using velocities from near-bed layers with y^+ in the range of 600 to 800 as opposed to the bottom layer produces more reliable τ_b estimates, without significant . This y^+ range corresponds to normal distances, from the bed surface, of about 0.15 times the total depth of flow.

Many bedload formulas have been reported in the literature. The well-referenced formula of van Rijn (1984) is used to calculate bedload flux q_b in this study. This formula allows for particle saltations under the influence of hydrodynamic and gravity forces. Its development is based on extensive experiments conducted with sediments of 200 to 2000 μm in particle diameter, flow depth larger than 0.1 m and Froude numbers less than 0.9, which fit the conditions considered in this study (Table 4.1). Pertinent relationships are

$$q_b = 0.053\sqrt{(s-1)g d_{50}^3}\,\frac{T^{2.1}}{D_*^{0.3}} \tag{4.12}$$

$$D_* = d_{50}\left[\frac{(\rho_s - \rho)g}{\nu^2}\right]^{1/3} \tag{4.13}$$

$$T = \frac{\tau_b - \tau_c}{\tau_c} \tag{4.14}$$

Table 4.1 A summary of parameters for model runs. The three different values in parentheses for some of the parameters correspond to model runs H1, H2 and H3

Parameters	Value	Unit
Discharge	0.20	m^3/s
Sediment median grain size d_{50}	2.1	mm
Sediment porosity λ	0.457	
Bottom roughness height $k_s(= 3d_{50})$	0.0063	m
Mesh dimensions in the x_1 direction	(113, 161, 85)	
Mesh dimensions in the x_2 direction	(63, 69, 63)	
Mesh resolution in the x_1 direction Δx_1	(1.66–10.2, 1.4–6.6, 1–5)	cm
Mesh resolution in the x_2 direction Δx_2	(1.66–8.35,1.4–6.6, 1–7.5)	cm
Number of layers in the x_3 direction	7	
Mesh aspect ratio	(6.14, 4.7,7.5)	
Time step Δt	(0.002, 0.002, 0.002)	s
Simulation period	(1940, 60, 60)	s
Bottom drag coefficient $C_D \times 10^3$	2.5	
Constant in calculation of A_m	0.1	
Criterion for convergence	10^{-6}	

According to Paphitis (2001), τ_c ranges from 0.59 to 1.69 Pa, with a mean value of 1.09 Pa (for $d_{50} = 2.1\text{mm}$). However, these values are relevant to the case of bedload transport over a flat channel-bed. Since the bed surface slopes in a scour hole, it is necessary to replace τ_c in Equation (4.14) with a modified critical shear stress. The resultant equation is

$$T = \frac{\tau_b - \varepsilon\tau_c}{\varepsilon\tau_c} \tag{4.15}$$

We express the modification factor ε following Roulund et al. (2005) but introduce a lower limit ε_o, yielding

$$\varepsilon = \max\left(\cos\beta\sqrt{1-\frac{\sin^2\alpha\tan^2\beta}{\tan^2\varphi_c}} - \frac{\cos\alpha\sin\beta}{\tan\varphi_c}, \varepsilon_\circ\right) \tag{4.16}$$

where β is angle of maximum bed slope, and α is angle of near bed velocity and the maximum slope direction. The critical shear stress in Equation (4.15) and the lower limit ε_o in Equation (4.16) are treated as calibration parameters. The reason for introducing the limit is as follows: The first expression in the parenthesis of Equation (4.16) leads to a decrease in ε or equivalently the modified critical shear stress $\varepsilon\tau_c$ with increasing bed slope. They approach zero at the angle of slope equal to the angle of repose of sediments, which can cause unrealistically large scour and result in numerical instability. The use of ε_o can effectively prevent the unrealistic condition from taking place.

4.2.5 **Morphologic model**

The bed level, Δz, (Figure 4.1) is updated according to the Exner equation

$$(1-\lambda)\frac{\partial z}{\partial t} + \frac{\partial q_j}{\partial x_j} = 0; \quad j = 1,2 \tag{4.17}$$

where λ is sediment porosity and q_j is bed load flux. The live layer is set to $2d_{50}$, used as the limit on bed level change Δz within one time step during a simulation. The bed level will be updated continuously until the scour depth reaches the equilibrium state, i.e., the shape and the depth of the scour hole no longer changes.

4.2.6 **Slope stability and land slide model**

During a simulation, the slope of local bed surface in a developing scour hole needs to be examined. The land slide model is not a numerical consideration. Rather, it reflects a physical phenomenon occurring in the nature. This is to ensure that the slope resulting from bed level change [Equation (4.17)] never exceeds the angle of repose of sediments φ_c. The slope angle (θ_1, θ_2) in the (x_1, x_2) directions is calculated as

$$\tan(\theta_1, \theta_2) = (\Delta z_1 / \Delta x_1, \Delta z_2 / \Delta x_2) \tag{4.18}$$

At any time, if bed level change results in $\theta_1 > \varphi_c$ or $\theta_2 > \varphi_c$, an adjustment to the bed levels of the two neighbouring nodes will be made by lowering the higher bed level and raising the lower bed level. If necessary, the adjustment is given by

$$\Delta z_j = \frac{1}{2}(\tan\theta_j - \tan\phi_c)\Delta x_j; \quad j = 1,2 \tag{4.19}$$

To prevent local fluctuating features in the bed level from causing a numerical instability problem, the bed level is smoothed out, as recommended by Liang and Cheng (2005). A five point median filter is applied. That is to say that the bed level at the node in question is taken as the median value of the bed levels calculated from Equation (4.17) and, if necessary, Equation (4.19) for that node and two nodes immediately upstream and downstream of that node.

4.2.7 **Setup of model runs**

The channel geometry, approach flow (Figure 4.1) and sediment grain size used in the simulations match the experiments of Graf and Istiarto (2002). This allows a direct comparison between numerical and experimental results. Individual simulations commence from an initially flat channel-bed (Figure 4.1) and proceed until sediment scour/deposition reaches as a state of equilibrium. In Table 4.1, key simulation parameters

are listed. At the upstream open boundary, the approach flow is 0.18 m deep; a velocity profile derived from the experimental data is imposed.

In the horizontal, the mesh sizes are as fine as 0.0166 m near the pier (Figure 4.1) to resolve expected large velocity gradients. To reduce computational costs, the sizes increase gradually (by a factor ≤ 1.4 between adjacent cells) for areas away from the pier, the coarsest mesh being 0.102 m. The ratio of the size in the x_1-direction to that in the x_2-direction is sufficiently low (≤ 6.14) to avoid flow distortion. In the vertical, the water column (Figure 4.1) is divided into seven σ layers, with thickness decreasing from the free surface to the channel-bed. The top layer is 23% of the local total depth of flow and the bottom layer is 3%, meaning that initially, the two layers have a thickness of 0.041 and 0.005 m, respectively. The use of higher resolutions closer to the bed is appropriate for resolving the bottom boundary layer.

4.3 RESULTS AND DISCUSSION

4.3.1 Mesh independence

The mesh used (Figure 4.1) must be such that solutions of scour and deposition development are independent of mesh configurations. This was tested through three runs: H1, H2 and H3. For H1 and H2, the upstream and downstream channel sections have the same length (5 m, Figure 4.1). For Run H3, the two channel sections have been shorten to 1.95 and 1.5 m, respectively, to save computation time. The mesh has successively refined resolutions from H1 to H2 to H3 (Table 4.1). These runs were carried out without and with non-hydrostatic pressure corrections.

Between Runs H1 and H2, the developing patterns of scour and deposition around the pier at model time of 1 min are compared in Figure 4.2a,b. The bed level changes are

similar: Two scour cores appear upstream of the pier's centre and two deposition cores appear downstream. The maximum scour depths normalised by the pier diameter are 0.60, 0.65 and 0.66, whereas the normalised maximum deposition heights are 0.45, 0.36 and 0.41 for Runs H1, H2 and H3, respectively (Table 4.2). The table also shows comparable results of scour/deposition areas as well as their central positions between the runs.

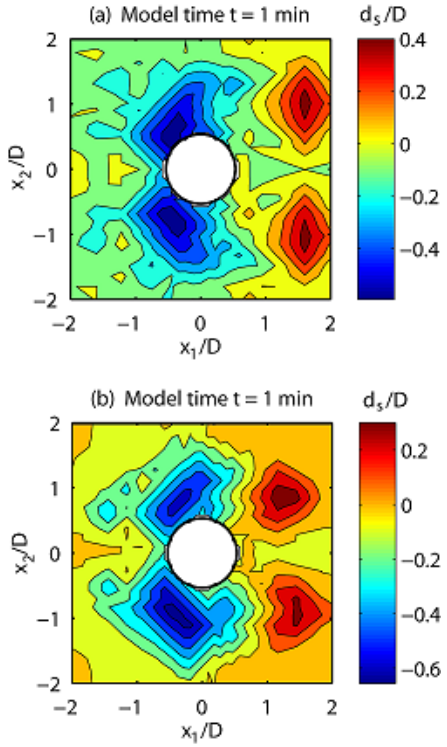

Figure 4.2 Contours of bed level change, showing sites of scour (negative values) and deposition (positive values): (a) for Run H1 and (b) for Run H2.

Table 4.2 Comparisons of predicted scour and deposition. The listed scour depths and deposition heights have been normalised by D, and the listed areas by $\pi D^2/4$.

	Max. scour depth	Scour deeper than 0.4D		Max. deposition height	Deposition higher than 0.1D	
		Area	Central position (x_1/D, x_2/D)		Area	Central position (x_1/D, x_2/D)
			Hydrostatic model computation			
H1	-0.60	0.52	(-0.40, -0.83)	0.45	2.16	(1.53, -0.98)
H2	-0.65	0.46	(-0.37, -0.93)	0.36	1.96	(1.40, -0.84)
H3	-0.66	0.47	(-0.42, -0.81)	0.41	2.01	(1.60,- 0.73)
			Non-hydrostatic model computation			
H1	-0.63	0.50	(-0.39, -0.80)	0.44	1.27	(1.53, -0.93)
H3	-0.55	0.47	(-0.42, -0.83)	0.39	1.31	(1.33,- 0.76)

Run H3 has produced bed level changes (not shown) similar to those shown in Figure 4.2a,b, except that the changes for H3 contain some small fluctuating features, probably caused by reflection from the downstream boundary as the model channel used has a relatively short extension downstream of the pier. The presence of fluctuating features is undesirable as they can cause numerical instability. Between Runs H1 and H2, the mesh used in H1 offers higher computational efficiency, and therefore is used for subsequent runs. With non-hydrostatic pressure corrections, between H1 and H3, the predicted scour and deposition areas and their central locations are comparable (Table 4.2); the predicted flow velocities are also comparable. For example, at the location of maximum scour depth, the horizontal velocities (u_1, u_2) are (0.35, -0.03) and (0.33, -0.03) m/s for H1 and H3, respectively.

4.3.2 **Velocity comparison**

A series of subsequent runs with non-hydrostatic pressure corrections were carried out to calibrate the model by adjusting the critical shear stress τ_c [Equation (4.15)] and the limit ε_o [Equation (4.16)] in the ranges of $0.62\,\text{Pa} \le \tau_c \le 0.95\,\text{Pa}$ and $0.2 \le \varepsilon_\circ \le 0.3$. Calibration is achieved with $\tau_c = 0.68$ Pa (for $d_{50} = 2.1$ mm, the corresponding Shields parameter is 0.02) and $\varepsilon_\circ = 0.23$ (Run N1), which gives the best comparison between predicted and measured velocities (Figure 4.3). The predicted velocities were extracted from the model results at a state of equilibrium for the same locations as the measurements made by Graf and Istiarto (2002). The comparisons are acceptable, especially with regards to strong velocities. Accurate predictions of velocity for locations of strong flow are the most important for calculations of the bed shear stress, and hence bedload transport and scour depth. The predicted maximum scour depth for Run N1 is also in the best agreement with measurements as will be discussed later. The predicted velocities for Run N2, where $\tau_c = 0.68$ Pa and $\varepsilon_\circ = 0.25$, are shown in Figure 4.3 for comparison.

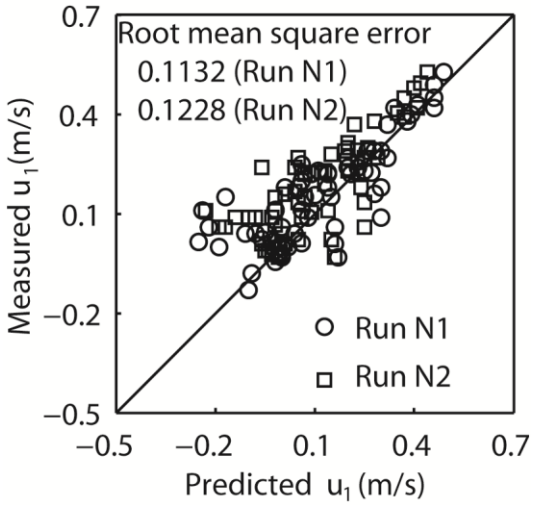

Figure 4.3 A comparison of predicted velocity u_1 with measurements (Graf and Istiarto, 2002) made from locations along the centreline $x_2 = 0$ (Figure 4.1). For Run N1, $\tau_c = 0.68$ Pa and $\varepsilon_\circ = 0.23$. For Run N2, $\tau_c = 0.68$ Pa and $\varepsilon_\circ = 0.25$.

4.3.3 **Equilibrium scour depth**

In the runs described in Section 4.3.2, integration of the unsteady model equations over time has produced solutions at a state of equilibrium are reached. This is illustrated in Figure 4.4, where time series of scour depth at the maximum scour site and the upstream nose of the pier for Runs N1 and N2 are plotted. A number of observations can be made: Firstly, the scour depth reaches a state of equilibrium at the model time of t_e = 32.3 min for Run N1 and t_e = 40 min for Run N2. For both runs, during the first 10 min of model time, the bed level changes rapidly, giving rise to a scour hole around the pier; subsequently, the scour hole grows at lower time rate. Second, Run N1 predicts a maximum scour depth of about 1.78D occurring to the southwest of the pier (Figure 4.2a,b), the coordinates (x_1/D, x_2/D) being (-0.45, -0.91). At the upstream nose of the pier the scour depth is about 1.56D. Third, Run N2 predicts a maximum scour depth of about 1.52D, which is smaller than the prediction for Run N1 by 14.6% as a result of an increase in the critical shear stress. The

maximum scour depth is located at $(x_1/D, x_2/D) = (-0.45, -1.02)$. For Run N2, the scour depth is about 1.13D at the upstream nose of the pier.

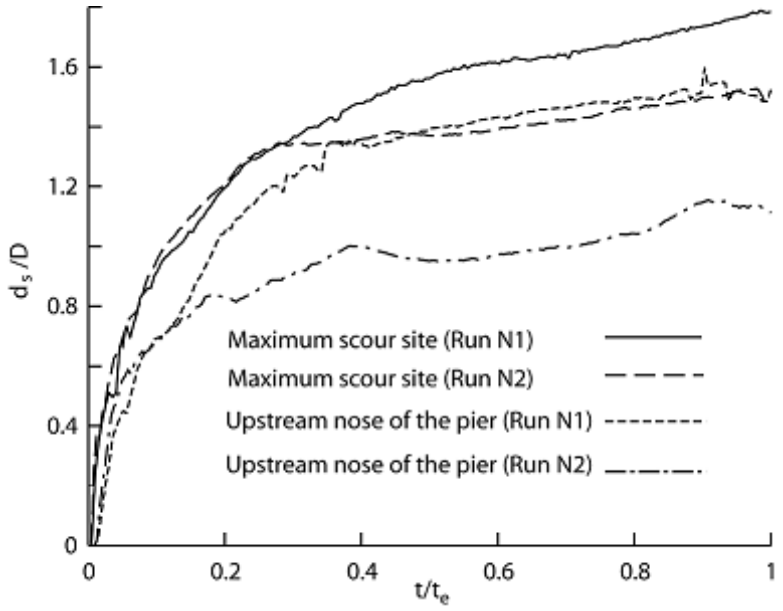

Figure 4.4 Time series of normalised scour depth d_s/D at the maximum scour site and the upstream nose of the pier for both Runs N1 and N2.

4.3.4 **Velocity field**

Velocity vectors at a stage of equilibrium for Run N1 are plotted in Figure 4.5a for the surface layer and Figure 4.5b the second layer from the bottom. In Figure 4.5a, as the flow approaches the pier, the longitudinal velocity decreases gradually from 0.54 m/s at $x_1 = -3D$ to 0.21 m/s close to the pier. The transverse velocity is significant around the pier, with a maximum value of 0.24 m/s; the transverse velocity is small at distances of larger than 3D from the pier. In the wake region, the flow reverses direction near the pier, with weak circulations in clockwise and counter-clockwise directions. The wake flow weakens with distance away from the pier.

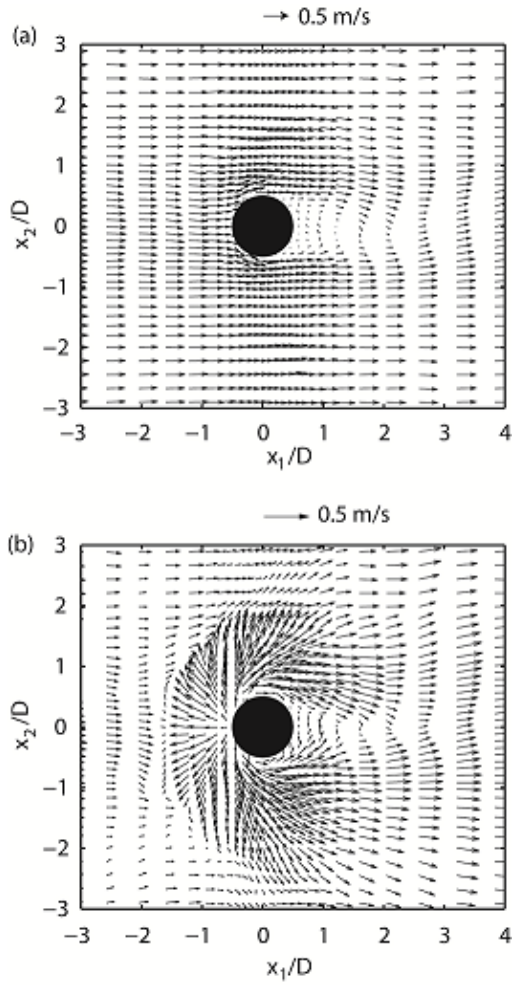

Figure 4.5 Velocity vectors for the top layer and the second layer from the bottom for Run N1.

In Figure 4.5b, the longitudinal velocity decreases from 0.30 m/s at $x_1 = -3D$ to very small values half way toward the pier. As the flow approaches the pier, the flow reverses direction; the flow has a maximum speed of 0.24 m/s in the x_1-direction and 0.37 m/s in the x_2-direction. This condition is expected to cause bed sediments to move around the pier. Immediately downstream of the pier, the flow direction is toward downstream, which has the tendency to carry sediments away from the vicinity of the pier toward downstream and to deposit them there. Downstream of the pier inside the scour hole, there is an increase in the longitudinal velocity with increasing distance toward downstream. As expected, the

transverse velocity is large near the pier inside the scour hole and becomes insignificantly small outside.

As illustrated in Figure 4.4, the predicted scour depths at the indicated locations are sensitive to the value chosen for ε_o in Equation (4.16). The predicted velocity field is also somewhat sensitive to the chosen value; this is indicated by the differences between the velocity vectors plotted in Figure 4.5a,b for Run N1 $(\varepsilon_0 = 0.23)$ and those (not shown) for Run N2 $(\varepsilon_0 = 0.25)$, but the differences are local and are limited to a small number of locations:

(a) Near the upstream edge of the scour hole around $(x_1 / D \approx -3, x_2 / D \approx 0)$ in Figure 4.5a, the longitudinal velocity for the surface layer is stronger for Run N1than Run N2, by up to 0.07 m/s or 13% of the local velocity.

(b) Behind the pier, between the two runs, the flow wakes for the surface layer have essentially the same strength, except some small shifts in the position of the wake paths.

(c) On the lateral sides of the pier, the longitudinal flow is stronger for N2 than N1, by up to 0.07 m/s for the surface layer and 0.12 m/s near the bottom to the left side of the pier (for an observer facing downstream, the same thereafter).

(d) Near the bottom, upstream of the pier around $(-1.5 < x_1 / D < -0.5, -0.5 < x_2 < 0.5)$ in Figure 4.5b, the reversal flow velocity is stronger for N1 than N2, by up to 0.24 m/s. Thus, it is important to optimise the parameter.

4.3.5 **Flow–sediment interaction**

Vertical sections along the centreline $x_2 = 0$ (Figure 4.6a-d) show snapshots of the

changing velocity field and channel-bed for Run N1. Shortly into the run (Figure 4.6a), velocity vectors are mostly parallel to the flat channel-bed, exhibiting a typical boundary-layer velocity profile. As the flow approaches the pier, it decelerates in the horizontal. For example, the surface-layer velocity drops from the approach velocity by 54% (Figure 4.6b) to 60% (Figure 4.6d). The horizontal deceleration forces a strong downflow at the upstream nose of the pier. The downflow maxima (Figure 4.6a-d) occur close to the bed, at a depth below the surface as 75% of the total depth. At equilibrium (Figure 4.6d), the downflow has a maximum magnitude of 0.82 m/s, which appears to be too high compared to 0.8 times as suggested by Copp and Johnson (1987). Most remarkably, a strong vortex system forms at the foot of the pier on its upstream side.

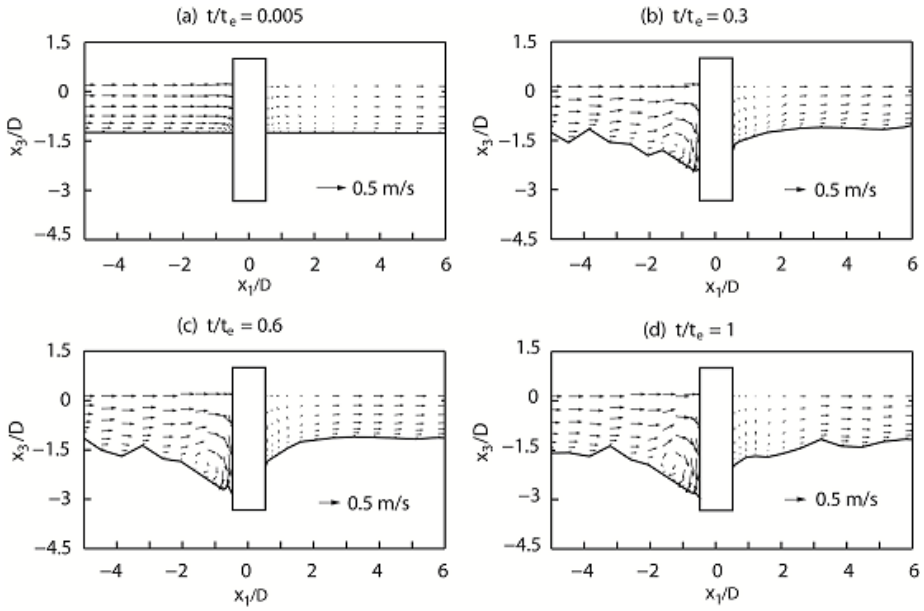

Figure 4.6 Vertical sections along the centreline, showing the development of the flow field and bed scour.

Immediately downstream of the pier, the flow reverses direction (Figure 4.6a-d, the first a few columns of vectors, not very visible) and is weak. A weak downflow of up to 0.05–

0.13 m/s develops in time (Figure 4.6a-c), with a maximum of 0.1 m/s at equilibrium (Figure 4.6d). At a short distance further downstream, the flow has an upward velocity component toward the water surface. The downward and upward motions create a weak vortex downstream of the pier. Consequently, flow-induced scouring is larger on the upstream than downstream side.

On the upstream side, the bed surface near the pier develops, in time (Figure 4.6a-d), a progressively smoother profile as wavy bed features propagate upstream, and at equilibrium (Figure 4.6d), the bed slope of the scour hole reaches the angle of repose of sediments (34°). On the downstream side, the bed slope also reaches 34° immediately downstream of the pier but rapidly decreases to 14° and remains so over a large distance $(1 \le x_1 / D \le 3)$.

4.3.6 **Scour around the pier**

Around the pier, scour develops as shown by contours of bed level change with time (Figure 4.7a-d). Scour depth increases from 0.17 m or 1.13D as the maximum on both lateral sides of the pier (Figure 4.7a) to 0.268 m or 1.78D around the location $(x_1 / D = -0.45, x_2 / D = -0.91)$ at equilibrium (Figure 4.7d). At the upstream nose of the pier, scour depth increases from 0.13 m (Figure 4.7a) to 0.235 m at equilibrium (Figure 4.7d). This is in good agreement with the measured scour depth of 0.25 m (Graf and Istiarto, 2002).

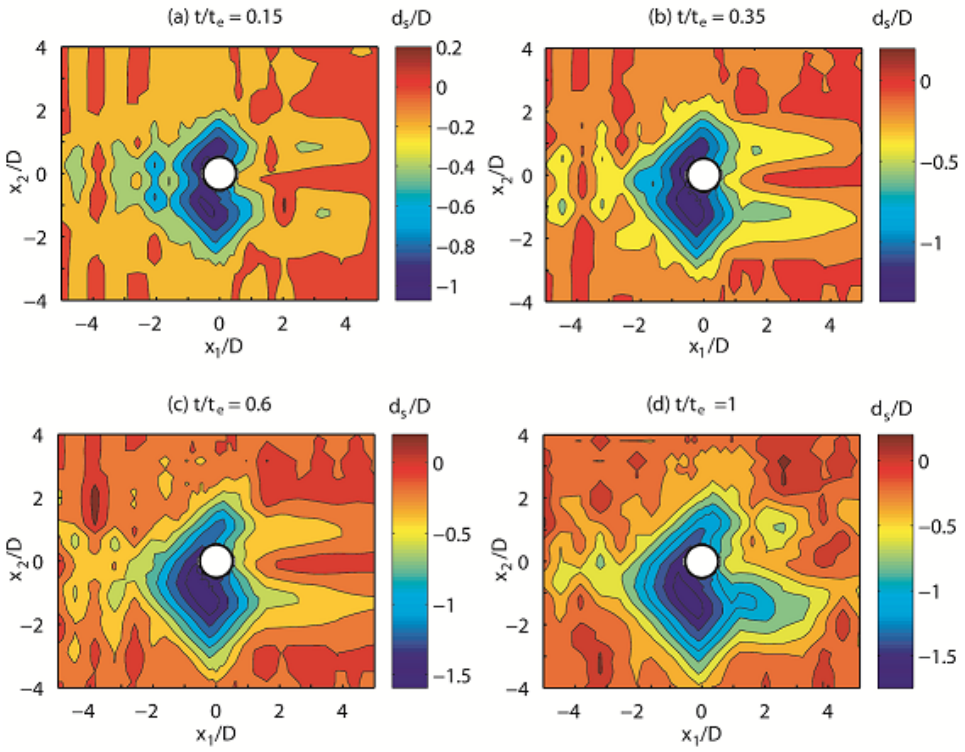

Figure 4.7 Contours of bed level change at selected model times for Run N1, showing the development of sediment scour and deposition around the pier. Positive and negative values mean sediment deposition and scour, respectively.

Downstream of the pier, sediments begin to deposit around the location $(x_1/D = 2, x_2/D = -0.8)$, with a maximum height of 0.043 m (Figure 4.7a). Later deposition shifts toward downstream. At equilibrium (Figure 4.7d), scour depth reaches a maximum of 0.19 m around the downstream location $(x_1/D = 0.59, x_2/D = -1.32)$ on one side of the centreline $x_2 = 0$ and 0.15 m around $(x_1/D = 0.59, x_2/D = 1.47)$ on the other side. Along the centreline, very close to the pier surface $(x_1/D = 0.59)$, scour depth is 0.115 m, which is lower than the measurement of 0.19 cm (Graf and Istiarto, 2002). The predicted 0.19 m maximum scour depth matches the measurement in magnitude, although there is a difference in location between the prediction and measurement.

From the initial condition of a flatbed (Figure 4.1), scour emerges from the lateral sides of

the pier (Figure 4.7a), and patterns of increasing scour depth migrate upstream toward the upstream nose of the pier (Figure 4.7b), whereas patterns of deposition on the downstream side shifts toward downstream. During their development, scour patterns are not symmetric about the centreline (Figure 4.7b,c).

With regard to the significance of non-hydrostatic pressure corrections, a comparison between Figure 4.7d and Figure 4.8 reveals that the corrections appear to reduce the asymmetry of the scour patterns about the centreline. Without the corrections, there is an under prediction of the scour depth at the nose of the pier from 1.56*D* (Figure 4.7d) to 1.4*D* (Figure 4.8). Predictions of scour depth and patterns are sensitive to the limit chosen for the parameter ε_o [Equation (4.16)]; this is clear from a comparison between the results for Run N2 where $\varepsilon_0 = 0.25$ (not shown) and the results shown in Figure 4.7a-d for Run N1 where $\varepsilon_0 = 0.23$. The latter has produced results in reasonable agreement with measurements (Graf and Istiarto, 2002).

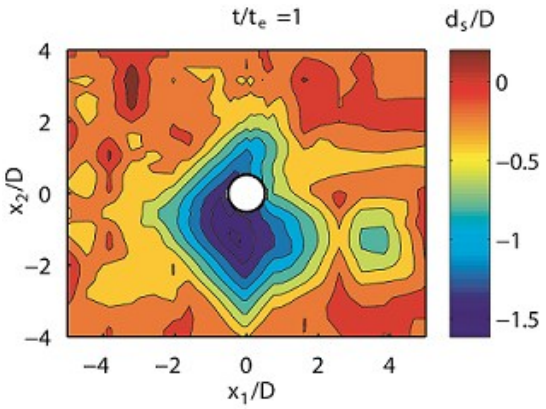

Figure 4.8 Contours of bed level change at equilibrium for a model run, where the conditions are the same as Run N1, except that the hydrostatic pressure approximation is used.

4.4 CONCLUSION

The multi-layer modelling techniques developed in this paper have successfully

predicted three- dimensional flow velocity around a pier and resultant pier scour, which are in reasonable agreement with measurements (Graf and Istiarto, 2002). The results show that a strong vortex forms at the foot of the pier on the upstream side and a weak vortex on the downstream side. A strong downflow occurs near the pier's upstream nose. As a result, sediments are effectively removed from the upstream nose and deposited downstream. Bed scour emerges from the lateral sides of the pier, patterns of increasing scour depth migrate upstream toward the nose, and the upstream scour hole continues to develop until the bed slope reaches the angle of repose of sediments. The scour hole extends its downstream edge towards the downstream direction until a state of equilibrium is reached. The scour hole is shallower downstream than upstream of the pier; this prediction is consistent with the findings from Richardson and Wacker (1999).

It can be seen that the maximum scour depth using the empirical equations of Melville and Chiew (1999), FHWA (2001) and Sheppard et al. (2004) are different from the result obtained from this study, by 8.4%, 17.4% and 5%, respectively.

This modelling work combines the beneficial use of non-uniform mesh in the horizontal and terrain-following σ coordinate in the vertical, which is particularly useful for local pier scour computations. In addition, the use of shallow-water equations in conjunction with non-hydrostatic pressure corrections offers not only high computational efficiency but also the capacity to handle strong vertical motions in a scour hole. Unlike general CFD models, which are impractical for field scale applications due to prohibitively high computational costs, the efficient yet adequate model from this work is suitable for much needed field scale applications.

Chapter 5 A bridge scour model with non-uniform sediments

Summary: Pier scour is a significant problem affecting the safety of bridges. For given hydraulic conditions and pier geometry, accurate scour prediction with non-uniform sediments is important, but this need has not been fulfilled. The purpose of this paper is to develop a three-dimensional (3-D) model for scour development prediction and to verify the model using existing laboratory measurements. The model allows for selective transport of non-uniform sediments, sediment particle hiding, and bed-level change in response to scour and deposition. We have successfully predicted the development of scouring around a circular pier on a mobile channel-bed with non-uniform sediments; equilibrium scour depth prediction agrees well with the measurements. Scour patterns emerge from the lateral sides of the pier and migrate toward its upstream nose. Upstream of the pier, strong downflow and eddy motions develop and effectively remove sediments from the foot of the pier further downstream; at equilibrium, the bed surface slope almost reaches the angle of repose of sediments. On the upstream side, the scour hole has a shape of almost half a cone, true for both uniform and non-uniform sediments. Grain size non-uniformity is shown to reduce the magnitude of scour. These findings are of relevance to the safe and cost-effective design of pier foundations. The modelling techniques presented are computationally efficient and are useful for field-scale applications.

5.1 INTRODUCTION

Sediment scour around bridge-piers has caused many bridge failures (Melville and Coleman, 2000). Thus, it is necessary to accurately predict scour for given hydraulic conditions and pier geometry so that the design of pier foundations is safe and cost-effective. So far this need has not been fulfilled. Difficulty in predicting is caused by the complex three-way interaction involving water flow, pier obstruction and erodible channel-bed, especially with non-uniform sediments (Hong et al., 2012). The purpose of this paper is to develop and verify a 3-D model for pier scour prediction, which considers fractional transport of non-uniform sediments.

The simplified case of pier scour with uniform sediments has been studied extensively on the basis of dimensional analysis (Melville and Coleman, 2000; Melville and Sutherland 1988; Raudkivi 1986). The outcome is semi-empirical formulae for predicting the maximum value of scour depth, d_s; input variables are mostly approach flow depth, velocity, u_o, pier diameter, D, and median sediment grain size, d_{50}. The prediction is typically presented in dimensionless form d_s/D. Overall, the formulae give an overprediction at the field scale (Mohamed et al., 2005; Lee and Strum 2009).

In fact, at many river sites of bridge failure or damage, the bed sediments were non-uniform (Melville and Coleman, 2000). A number of investigators have considered pier scour with non-uniform sediments, using various analytical methods. Johnson (1992) used the probabilistic approach to calibrate d_s formulae. Muzzammil and Ayyub (2010) compared the performance of some statistical neural network techniques for scour development prediction. Hong et al. (2012) applied the support vector regression technique, suggesting that the difference between the densimetric particle Froude number

and critical densimetric Froude number is important for predicting time-dependent d_s.

None of the studies mentioned-above has considered fractional transport of non-uniform sediments. At best, non-uniformity is indirectly reflected through the use of an effective grain size or d_{50}, along with the geometric standard deviation of grain size distribution, σ_g. In a recent review, Brandimarte et al. (2012) pointed out the importance to consider various aspects of the scour problem and to improve the understanding of scour-triggering dynamics.

The current understanding of the scour problem has been based on mostly observations from laboratory experiments. Experiments with uniform sediments show temporal variations in d_s and time to equilibrium (Melville and Chiew, 1999). They also show the influence on d_s from factors such as pier arrangement and spacing (Amini et al., 2012), pier diameter, D (Ettema et al., 2006), and the D/d_{50} ratio (Sheppard and Miller, 2006). Some of the findings from these studies are not conclusive. For example, Sheppard and Miller (2006) have suggested that the ratio D/d_{50} has a progressively weaker influence on d_s at higher u_o relative to the threshold velocity for the initiation of sediment motion. This contradicts Ettema et al.'s (2006) finding that d_s decreases with increasing D.

Experiments with fine to median size gravel (Raikar and Dey; 2005) show that d_s increases with decreasing gravel size, and dimensionless time to equilibrium increases with increasing pier Froude number for uniform gravel and decreases with increasing σ_g for non-uniform gravel, meaning that fractional transport should be considered in prediction of pier scour with non-uniform sediments. According to Chiew and Melville (1989), with non-uniform sediments, d_s is smaller than or equal to that associated with uniform sediments of the same d_{50}. The armour layer is progressively broken with increasing u_o. Therefore, at

high u_o, d_s for non-uniform sediments is equal to that for uniform sediments. The local scour depth becomes independent of sediment size for $D/d_{50} > 50$. Note that there are uncertainties in translating laboratory-based scour predictions from the small laboratory scale to the field scale.

Numerical modelling is a good alternative, with the advantages of less time consuming and less expensive. More importantly, numerical modelling can easily be implemented at the field scale. A review of the literature shows some studies of modelling pier scour with uniform sediments (Khosronejad et al., 2012; Roulund et al., 2005). These studies have ignored the effects of armouring, selective transport and relative exposure on scour development. Chiew (1991) showed experimental evidence that at low flow velocity, an armoured bed of coarse particles can form with a slight transport of fine particles, whereas at high velocity, particles of all sizes participate in transport and a transition flatbed form at all sediment size. Modelling the indicated scour process is difficult.

Three-dimensional models involving non-uniform sediments have been applied to channel bends and lateral contractions (Bui and Rutschmann, 2010; Fischer et al., 2009; Tritthart and Schober, 2011). To the best of our knowledge, no application to pier scour has been reported in the literature. This study deals with pier scour with non-uniform sediments around a cylindrical pier under steady clear-water condition, without supply of sediments to the local scour hole from upstream under flow velocities below the critical velocity for general sediment entrainment (Melville and Coleman, 2000). In the following, we describe the methodologies, discuss results and data comparison, and draw conclusions.

5.2 METHODOLOGIES

5.2.1 Hydrodynamics equations

For hydrodynamics computation, Pournazeri et al. (2013) added a new module for non-hydrostatic pressure to an existing 3-D hydrodynamics model that uses the hydrostatic pressure approximation (HydroQual, 2002). For details about the existing model, refer to Pournazeri et al. (2013). Only the main features of the model are briefly described here: The model is based on the equations of continuity and momentum balance. We obtain provisional velocity components $(\tilde{u}_1, \tilde{u}_2, \tilde{u}_3)$ and provisional water-surface elevation $\tilde{\eta}$ from solving the equations. Smagorinsky's (1963) scheme is used for turbulence closure in the horizontal. Mellor and Yamada's (1982) 2nd order scheme is used for turbulence closure in the vertical. The vertical eddy viscosity is related to turbulence kinetic energy and turbulence macro-scale. These two turbulence quantities are predicted using unsteady advection-diffusion equations. The horizontal and vertical diffusivities in the equations are calculated as a function of the two turbulence quantities.

5.2.2 **Boundary conditions**

At the free surface, the shear stress is zero; fluid particles on the surface will remain there all the time. At the channel-bed, the bed shear stress is calculated according to the quadratic law; the normal component of the velocity vector is zero. The channel and pier sidewalls are fully slippery; the velocity component normal to the sidewalls is zero. At the upstream open boundary, steady flow is prescribed; at the downstream open boundary, water surface elevation is given.

5.2.3 **Non-hydrostatic pressure**

As flow approaches a pier, acceleration in the vertical becomes significant. Therefore, the hydrostatic pressure approximation made in the model developed by HydroQual (2002)

is no longer adequate. Pournazeri et al. (2013) introduced non-hydrostatic pressure corrections to the model, using the formulation given in Casulli (1999). At a given time step, the corrected velocity components (u_1, u_2, u_3) are expressed as

$$u_1(i+1,j,k) = \tilde{u}_1(i+1,j,k) - 0.5\frac{\Delta t}{\Delta x_1}\left[m(i+1,j,k) - m(i,j,k)\right] \tag{5.1}$$

$$u_2(i,j+1,k) = \tilde{u}_2(i,j+1,k) - 0.5\frac{\Delta t}{\Delta x_2}\left[m(i,j+1,k) - m(i,j,k)\right] \tag{5.2}$$

$$u_3(i,j,k+1) = \tilde{u}_3(i,j,k+1) - 0.5\frac{\Delta t}{\Delta x_3}\left[m(i,j,k+1) - m(i,j,k)\right] \tag{5.3}$$

where $(\tilde{u}_1, \tilde{u}_2, \tilde{u}_3)$ is provisional velocity in x_1, x_2 and x_3 directions. The constant of 0.5 is the implicitness factor for stability. Suppose that the model domain is discretised into cells with dimensions (imx, jmx, kmx) in the (x_1, x_2, x_3) directions. Substituting Equations (5.1) to (5.3) into the continuity equation $\partial u_1/\partial x_1 + \partial u_2/\partial x_2 + \partial u_3/\partial x_3 = 0$ yields a seven-diagonal linear system for m.

(5.4)

$$\begin{bmatrix} A_1 & B_1 & 0 & . & C_1 & 0 & . & G_1 & 0 & . & . & 0 \\ D_2 & A_2 & B_2 & 0 & . & C_2 & 0 & . & G_2 & . & . & . \\ 0 & D_3 & A_3 & B_3 & . & . & C_3 & . & . & . & . & . \\ . & 0 & . & . & . & . & . & . & . & . & . & 0 \\ E_{imx-1} & . & 0 & . & . & . & . & . & . & . & . & G_{nm2} \\ 0 & E_{imx} & . & 0 & . & . & . & . & . & . & . & 0 \\ . & 0 & . & . & . & . & . & . & . & . & . & . \\ F_{np1} & . & 0 & . & . & . & . & . & . & . & . & C_{nm1} \\ . & F_{np2} & . & . & . & . & . & . & . & . & . & . \\ . & . & . & . & . & . & . & . & . & . & . & 0 \\ . & . & . & . & . & . & . & . & . & . & . & B_{n-1} \\ 0 & 0 & . & 0 & F_n & 0 & . & E_n & . & 0 & D_n & A_n \end{bmatrix} \begin{bmatrix} m_1 \\ m_2 \\ . \\ . \\ . \\ . \\ . \\ . \\ . \\ . \\ . \\ m_n \end{bmatrix} = \begin{bmatrix} R_1 \\ R_2 \\ . \\ . \\ . \\ . \\ . \\ . \\ . \\ . \\ . \\ R_n \end{bmatrix}$$

with $np1 = (imx-2)(jmx-2)+1$, $np2 = (imx-2)(jmx-2)+2$, $nm2 = n-(imx-2)(jmx-2)$, and $nm1 = n-(imx-2)$. Here, m_1, m_2, …, m_n are the unknowns or non-hydrostatic pressure values for the interior cells; A_1, B_1, …, D_n, A_n are the coefficients of the system; R_1, R_2, …, R_n are the constant terms. Subscript 1 corresponds to substituting Equations (5.1) to (5.3) into the continuity equation for the first interior cell $(i,j,k) = (2,2,2)$, and subscript n for the last interior cell $(i,j,k) = (imx-1, jmx-1, kmx)$. The system [Equation (5.4)] is symmetric and has positive definition. It is solved for the unknowns through preconditioned conjugate gradient iterations. Boundary conditions on m are as follows: On the sidewalls and pier surface, m is such that the normal flux is zero. At open boundaries, m is specified. At the water surface, m is zero.

Once m is solved, the velocity components are updated using Equations (5.1) to (5.3). The free surface elevation for a given interior cell is updated as

$$\eta = \tilde{\eta} + m/g \tag{5.5}$$

In Equation (5.5), m is associated with the bottom layer.

5.2.4 **Hydrodynamics solution techniques**

The model equations presented in the preceding sections are transformed to the σ-coordinate in the vertical. The free water surface as well as the channel-bed are transformed through into coordinate planes. This terrain-following feature of the σ-coordinates has advantages for simulating scour development.

The transformed model equations are then cast into finite difference equations and are numerically solved. The finite difference techniques used have 2nd order accuracy in space and time. For better computational efficiency, mode splitting techniques are used to separate vertically integrated flow (external mode) and flow structure in the vertical (internal mode).

5.2.5 **Bedload**

The bed shear stress τ_b is calculated using the logarithmic law of the wall. The friction velocity u_* is determined implicitly from

$$u_p / u_* = \kappa^{-1} \ln\left(y^+ / k_s^+\right) + 8.5 \tag{5.6}$$

The roughness height k_s is taken as $3d_{50}$. τ_b is related to u_* as $\tau_b = \rho u_*^2$. Application of Equation (5.6) using u_p in the (x_1, x_2) directions gives bed shear stress (τ_{b1}, τ_{b2}) in the two directions. Equation (5.6) is valid for the wall distance $y^+ > 11.53$. The actual y^+ values are determined from the shortest distance from the channel-bed surface to the location of u_p in question. This study uses velocity data from near-bed locations with $300 < y^+ < 500$ as opposed to the bottom layer velocity. This produces more reliable τ_b values and avoids

such results with fluctuating features.

Suppose that a sediment mixture is divided into J size fractions, and the j'th fraction has a percentage of f_j by volume. The percentages of individual fractions are updated at each time step during a simulation. For the j'th fraction, the per-unit width bedload rates in the (x_1, x_2) directions are given by

$$(q_{b1}, q_{b2}) = \frac{(\tau_{b1}^{1.5}, \tau_{b2}^{1.5})}{\rho^{1.5}(s-1)g} f_j W_j \tag{5.7}$$

The transport rate W_j is related to a transport function G as $W_j = 0.00218G(\phi)$. The functional form of $G(\phi)$ can be found in Parker (1990). The argument ϕ combines the effects of the normalized bed shear stress, particle reduced hiding factor and a straining factor as

$$\phi = \phi_\circ g_\circ \omega \tag{5.8}$$

$$\phi_\circ = \frac{(\tau_{b1}, \tau_{b1})}{(s-1)\rho g d_g \tau_c} \tag{5.9}$$

$$g_\circ = (d_j / d_g)^{-0.0951} \tag{5.10}$$

The straining factor allows for the effect of the difference between substrate and surface grain size distributions. Data fitting (Parker, 1990) yields the following relationship

$$\omega = 1 + \sigma_\phi(\omega_\circ - 1)/\sigma_\circ \tag{5.11}$$

with $\omega_\circ = 0.45 + 1.02e^{-0.6\phi_\circ}$, $\sigma_\circ = 1.5 - 1.67e^{-0.9\phi_\circ}$ and $\sigma_\phi = [\sum_j \ln^2(d_j / d_g)\ln^{-2} 2 f_j]^{0.5}$.

The critical shear stress in Equation (5.9) is specified in two steps: First, we determine an appropriate value based on the mean grain diameter. Then, we multiply the value by a modification factor, ε, to allow for the effect of bed slope (Roulund et al., 2005). This factor

is given by

$$\varepsilon = \max\left(\cos\beta\sqrt{1-\sin^2\alpha\tan^2\beta/\tan^2\phi_c} - \cos\alpha\sin\beta/\tan\phi_c, \varepsilon_\circ\right) \tag{5.12}$$

A lower limit, ε_o, has been imposed on ε, because the first expression in the parenthesis approaches zero at a slope angle equal to the angle of repose of sediments, and would cause infinite bedload and hence numerical instability. The lower limit is used to avoid instability.

5.2.6 **Morphologic model**

Bed-level changes are calculated using the Exner equation

$$(1-\lambda)\frac{\partial z}{\partial t} = -\sum_{j=1}^{J}\left(\partial q_{b1}/\partial x_1 + \partial q_{b2}/\partial x_2\right)_j \tag{5.13}$$

A live layer of thickness of $2d_{50}$ is assumed, meaning that bed level change will not exceed this thickness in one time step. The bed level is updated continuously until a state of equilibrium.

Some researchers (Armanini and Di Silvio, 1988; Borah et al., 1982; Rahuel et al., 1989) related active-layer thickness to flow depth, dune height or grain size. There is no consensus on how active-layer thickness is related to physical processes taking place in the layer and how to define the thickness (Bui and Rutschmann, 2010). Following Bui and Rutschmann (2010), we consider the maximum bed deformation at current time step as the active layer.

5.2.7 **Slope stability**

During scour development, the slope of channel-bed surface needs to be examined to ensure that the slope resulting from a bed-level change [Equation (5.13)] does not exceed the angle of repose of sediments. The slope angle in the (x_1, x_2) directions is calculated as

$$\tan(\theta_1, \theta_2) = (\Delta z_1 / \Delta x_1, \Delta z_2 / \Delta x_2) \tag{5.14}$$

At any time, if a bed-level change results in $\theta_1 > \phi_c$ or $\theta_2 > \phi_c$, an adjustment at two neighbouring nodes will be made by lowering the higher bed level and raising the lower one. The adjustment is given by

$$\Delta z_1 = 0.5(\tan\theta_1 - \tan\phi_c)\Delta x_1, \ \Delta z_2 = 0.5(\tan\theta_2 - \tan\phi_c)\Delta x_2 \tag{5.15}a,b$$

To prevent local fluctuating features in the bed-level, which can possibly cause a numerical instability problem, the bed-level is smoothed out using a five point median filter (Liang and Cheng, 2005).

5.2.8 **Model run setup**

Model runs are setup for hydraulic conditions and pier geometry matching an experiment (Run S3) reported in Chang et al. (2004). The model channel is shown in Figure 5.1. At the upstream boundary, the steady approach flow has a depth of 0.2 m and a vertical profile of u_1 velocity that gives a discharge of 0.056 m^3/s. In the experiment, the bed sediments have a median grain size $d_{50} = 1$ mm and a geometric standard deviation $\sigma_g = 2$. We construct a grain size distribution with six fractions (Figure 5.2), which has the same d_{50} and σ_g values as the experiment. The size fractions cover sediment classes from fine sands to fine gravel with grain sizes 0.19, 0.38, 0.75, 1.5, 3 and 6 mm. The corresponding percentages are 7, 22, 45.5, 17.5, 5 and 3%.

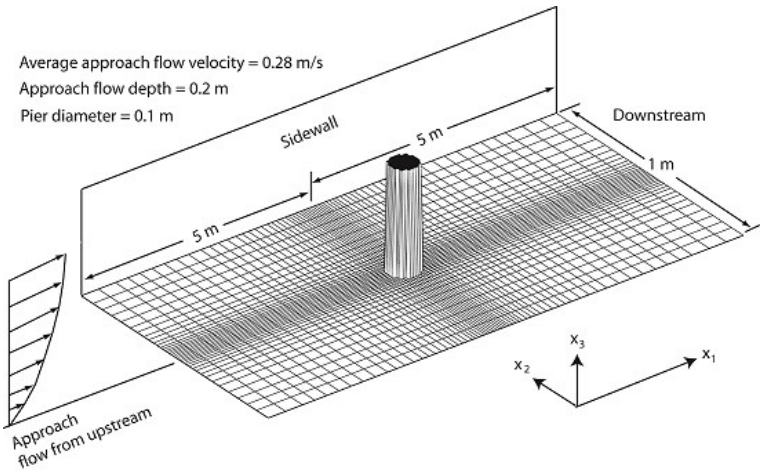

Figure 5.1 3-D view of the model channel, with a circular pier at the middle. Non-uniform mesh is used to cover the channel in the horizontal. Initially, the channel-bed is flat and has a slope of 0.0007 in the x_1-direction.

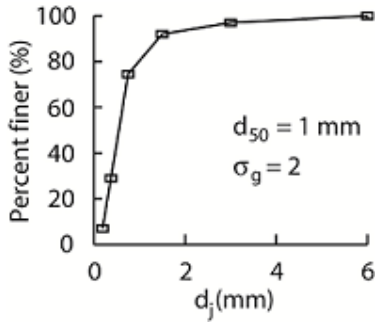

Figure 5.2 Sediment grain size distribution.

The channel is covered with non-uniform mesh in the horizontal (Figure 5.1). The mesh size is as fine as 0.01 m for the near-pier area to resolve velocity gradients. Away from the pier, the mesh size increases gradually by a factor less than or equal to 1.4 between neighbouring cells. This is saving to computational costs. The coarsest mesh size is 0.098 m. The aspect ratio of the mesh sizes in the (x_1, x_2) directions is limited to 9.8 or lower to avoid flow distortion. In the vertical, the water column is divided into 7 layers of varying thickness. The layer thickness is small near the bottom and relatively larger near the water surface. The bottom layer thickness is 3% the local flow depth, and the surface layer

thickness is 23%, meaning 0.006 and 0.046 m at the beginning of a simulation, respectively. Such layer partitioning maintains high computational efficiency and at the same time resolves the bottom boundary layer reasonably well.

Model runs start from the initial condition of a flat channel-bed and continues until a state of equilibrium. The channel-bed evolves as the bed sediments are removed or deposited by the action of the bed shear stress exerted by the flowing water.

The grain size distribution considered (Figure 5.2) has a median grain size $d_{50} = 1$ mm. The critical shear stress, τ_c in Equation (5.9), is estimated to be in the range of 0.25 to 0.75 Pa (Paphitis, 2001). The corresponding values for the Shields parameter are in range of 0.015 to 0.046. Note that τ_c is a calibration parameter. The model variables and parameters are listed in Table 5.1. The armour velocity listed is an estimate from empirical equations (Melville and Coleman, 2000).

Table 5.1 A summary of model variables and parameters, along with their values.

Parameters	Value	U
Discharge	0.056	m
Approach flow depth	0.20	m
Cross-sectionally averaged approach flow	0.28	m
Approach flow Froude number	0.2	
Sediment median grain size d_{50}	1	m
Geometric mean grain size d_g	0.7	m
Geometric standard deviation of sediment	2	
Sediment porosity λ	0.47	
Bottom roughness height k_s (= $3d_{50}$)	3	m
Ratio of the approach flow depth to pier	2	
Ratio of pier diameter to d_{50}	100	
Mesh dimension in the x_1-direction	(150, 155, 170)	
Mesh dimension in the x_2-direction	(36, 43, 46)	
Mesh size in the x_1-direction Δx_1	(1-9.8,0.9-9.6,0.8-8.3)	cm
Mesh size in the x_2-direction Δx_2	(1-5,0.9-3.5,0.8-3.2)	cm
Number of layers in the x_3-direction	7	
$\Delta x_1/\Delta x_2$ ratio	(9.8, 10.6,10.37)	
Time step Δt	(0.002,0.002, 0.002)	s
Simulation period	(2290, 550, 550)	s
Bottom drag coefficient	0.0025	
Constant in calculation of A_m	0.1	
Criterion for convergence	10^{-6}	
Ratio of u_o to armour velocity	0.45	

5.3 RESULTS AND DISCUSSION

5.3.1 **Sensitivity test**

Three runs P1, P2 and P3 were carried to test the model with regards to numerical stability, solution convergence and independence of the results on mesh configuration. These three runs differ in mesh sizes, Δx_1 and Δx_2 (Table 5.1). In the x_1-direction, Δx_1 ranges from 1 to 9.8 cm (or 0.1D to 0.98D) for run P1, and is progressively refined to 0.9 to 9.6 cm for Run P2 and to 0.8 to 8.3 for run P3. In the x_2-direction, the mesh size is also refined from run P1 to P2 and to P3. The aspect ratio $\Delta x_1/\Delta x_2$ is similar among the three

runs. For details about the setup, see Table 5.1.

Bed-level changes around the pier at selected model time of 550 s for Runs P1, P2 and P3 are compared in Figure 5.3a-d. The changes for P1 and P2 are similar. For P3, scour depth and deposition height are slightly larger than predictions for P1 and P2. The common features are that all the three runs predict two sites of scour upstream of the pier's centre and two sites of deposition downstream. The scour is deeper on the site to the right of the pier (to an observer facing toward downstream) than to the left, true for all the runs. The maximum values of scour depth for Runs P1, P2 and P3 are 0.254*D*, 0.256*D* and 0.29*D*, respectively, whereas the maximum deposition heights for the three runs are 0.278*D*, 0.264*D* and 0.253*D* (Table 5.2). The table shows comparable results of scour/deposition areas as well as their central positions for the three runs, meaning that the model results are independent of mesh configuration. The mesh used in Run P1 is the most efficient, and thus is used for subsequent runs**.**

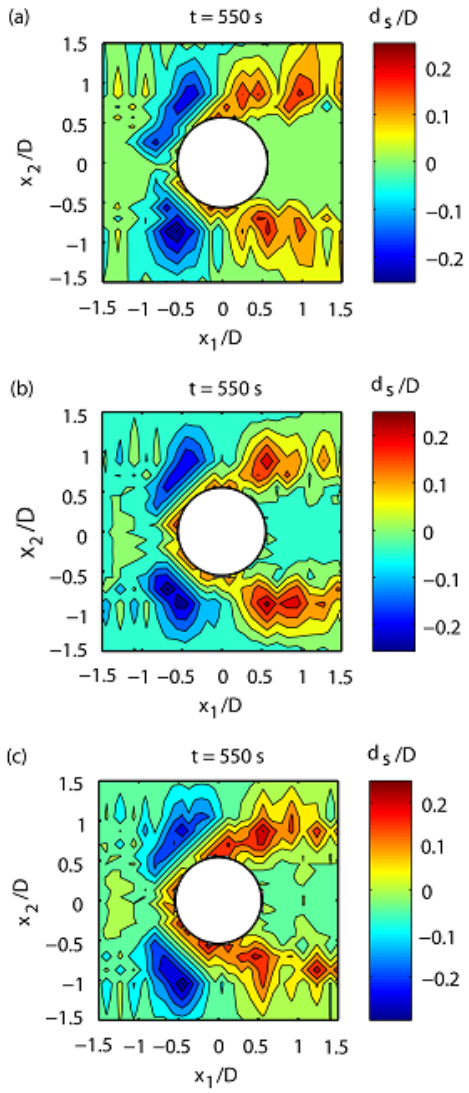

Figure 5.3 Contours of bed-level change, showing scour and deposition for Runs: (a) P1; (b) P2; (c) P3.

Table 5.2 Between-run comparison of predicted scour and deposition. The listed scour depths and deposition heights have been normalised by D, and the listed areas by $\pi D^2/4$.

Run	Max. Scour depth	Scour depth > 0.10D		Max. deposition height	Deposition height > 0.10D	
		Area	Central position (x_1/D, x_2/D)		Area	Central position (x_1/D, x_2/D)
P1	-0.254	0.39	(-0.57, -0.85)	0.278	0.36	(0.99, 0.87)
P2	-0.256	0.41	(-0.67, -0.89)	0.264	0.33	(0.97, 0.83)
P3	-0.290	0.40	(-0.55, -0.90)	0.253	0.34	(0.95, 0.85)

5.3.2 **Equilibrium solution**

A series of calibration runs were carried out using the critical shear stress τ_c [Equation (5.9)] and the limit ε_o [Equation (5.12)] as calibration parameters. Values tested are in the range of $0.25\,\text{Pa} \le \tau_c \le 0.32\,\text{Pa}$ and $0.1 \le \varepsilon_0 \le 0.15$. A value of 0.25 Pa for τ_c is suitable (Paphitis, 2001) for a sediment mixture with $d_{50} = 1$ mm; the corresponding Shields parameter is 0.015. The results for two of the calibration runs (C1 and C2) are discussed below: For Run C1, with $\varepsilon_\circ = 0.1$, and Run C2, with $\varepsilon_\circ = 0.15$, the predicted values of scour depth, d_s, at the pier nose (or the maximum d_s at the location next to the leading edge of the pier) are compared with the laboratory measurements of Chang et al. (2004) as time series in Figure 5.4. During the initial state of scour ($t/t_e < 0.2$, Figure 5.4), the bed-level changes rapidly, giving rise to a scour hole around the pier. Subsequently, the scour hole grows gradually with time ($t/t_e > 0.2$).

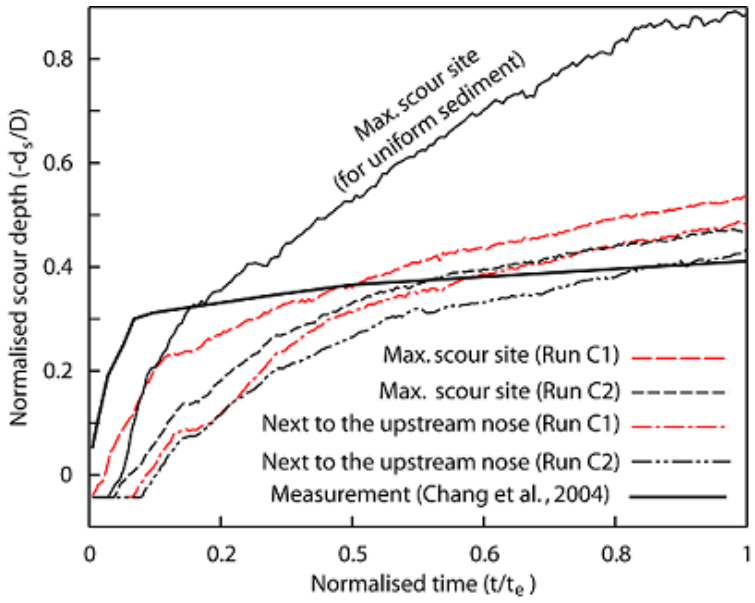

Figure 5.4 Time series of scour depth, ds, at the maximum scour site and/or around the pier nose for Runs C1 and C2, and for a calibration run with uniform sediments. Time series of d_s measured around the pier nose is shown for comparison. Values of d_s have been been normalised by the pier diameter.

At time to equilibrium t_e, the measurements (Chang et al., 2004) give a scour depth of $d_s = 0.43D$ (Figure 5.4, the thick solid curve). For Run C1, scour reaches a state of equilibrium at model time of 35 min, and the maximum d_s is $0.535D$,which occurs at the location ($x_1/D = -0.57$, $x_2/D = -0.86$). At the pier nose, d_s is $0.48D$; the prediction error is slightly lower than 12%. For Run C2, scour reaches a state of equilibrium at model time of 38.16 min, and d_s at the pier nose is $0.458D$ (Figure 5.4, dashed dotted curve), with a prediction error of as low as 6.5%. The scour depth reaches $0.471D$ as the maximum (Figure 5.4); this occurs at a location ($x_1/D = -0.7$, $x_2/D = 0.25$) very close to the nose. For Run C2, d_s predictions at the maximum scour location and at the pier nose agree well with the laboratory measurements.

For comparison, we calculate the local or maximum d_s for the hydraulic and pier geometric conditions given in Table 5.1, using a widely used empirical formula. Johnson's (1992) equation for maximum d_s, along with coefficients from Muzzammil and Siddiqui (2009), gives a value of 0.878D. This is a significant overprediction compared to Chang et al.'s (2004) measurement (0.43D). The calculations have used the Froude number of 0.2 and sediment gradation of 3.1, as given in Chang et al. (2004). In this modelling study, the predictions for Run C2 have accuracy of better than 90%. The model results for this run will be discussed further.

A time series of d_s for a calibration run with uniform sediments (d_{50} = 1 mm) is plotted as the thin solid curve in Figure 5.4. This calibration run uses the same conditions as Run C2 with the non-uniform sediments ($d_{50} = 1$ mm and $\sigma_g = 2$), except the sediments have uniform size. This calibration run predicts a maximum d_s at equilibrium almost two times that for Run C2. The implication is that sediment non-uniformity plays on an important role in scour development. Specifically, non-uniformity leads to a reduction in the magnitude of pier scour. This is consistent with the finding of Chiew and Melville (1989) who reported a reduction in the depth of scour hole, depending on the value of σ_g. The reduction can possibly be explained as the effect of armouring developed on non-uniform bed sediments.

5.3.3 **Velocity field in the horizontal**

The velocity vector field at a state of equilibrium for Run C2 is shown in Figure 5.5a,b. The approach flow has a cross-sectionally averaged velocity of $u_0 = 0.28$ m/s (Table 5.1). In the surface layer (Figure 5.5a), as the flow approaches the pier, the longitudinal velocity decreases from $u_1 = 0.37$ m/s at the upstream edge of the scour hole to $u_1 = 0.15$ m/s close to the pier. The transversal velocity u_2 is relatively high on the upstream side of the pier, with a maximum value of 0.22 m/s. The longitudinal velocity is as large as $u_1 = 0.41$ m/s on both sides of the pier. In the wake region, the flow direction reverses and results in weak circulation in clockwise and counter-clockwise. Far away ($x_1 / D > 16.2$) from the pier toward downstream, u_1 recovers the maximum value of 0.35 m/s, whereas u_2 decreases. Accordingly, wake intensity weakens.

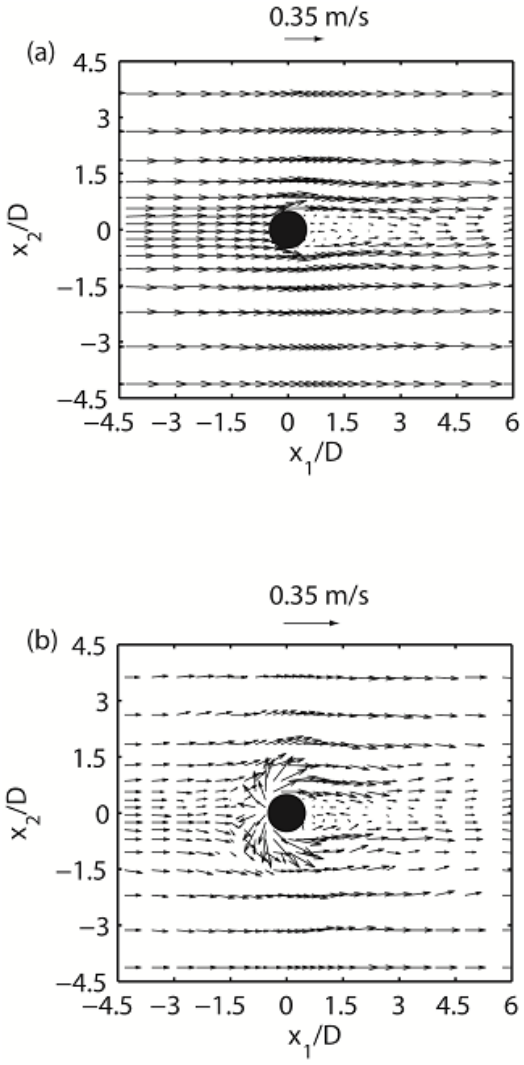

Figure 5.5 Velocity field for Run C2: (a) the top layer; (b) the second layer from the bottom. Every second column and row are plotted.

In the second layer from the bottom (Figure 5.5b), as the flow approaches the pier, u_1 decreases from 0.2 m/s to almost zero at the upstream edge of the scour hole. Then, flow reversal takes place, with a flow magnitude of 0.13 m/s in the vicinity of the pier. On the upstream side of the scour hole, u_2 is strong, with a magnitude of 0.27 m/s. The same holds true for u_1, with a magnitude of 0.24 m/s. The resultant flow velocity has a significant strength to carry sediments away from the upstream side toward downstream.

Downstream of the pier, the flow reverses its direction, with a magnitude of 0.08 m/s as

the maximum and produces wakes circulating in clockwise and counter clockwise. Further away from the pier toward downstream, u_1 increases to almost 0.14 m/s, with reduced wake intensity.

5.3.4 **Flow–sediment interaction**

During scour development, the velocity field, pier and channel-bed interact. To illustrate this interaction, we plot vertical cross sections (Figure 5.6d), showing velocity vectors and channel-bed profiles at selected time steps. The cross sections are located near the channel centreline (at $x_2 / D = 0.15$). Shortly after the beginning of Run C2 (Figure 5.6a), as the flow approaches the pier, the longitudinal velocity, u_1, decelerates by 72% (from 0.32 m/s in the approach channel), which creates a significant downflow just upstream of the pier. The downflow has a maximum of 0.22 m/s (close to the average approach flow velocity of 0.28 m/s), occurring at a depth equal to 55% the total depth below the water surface. Immediately downstream of the pier, the flow is downward; the flow remains downward over a horizontal distance of $x_1 / D = 1.5$ from the pier. Further downstream from the pier, there is an increase in horizontal flow velocity. The vertical flow velocity decreases to almost zero.

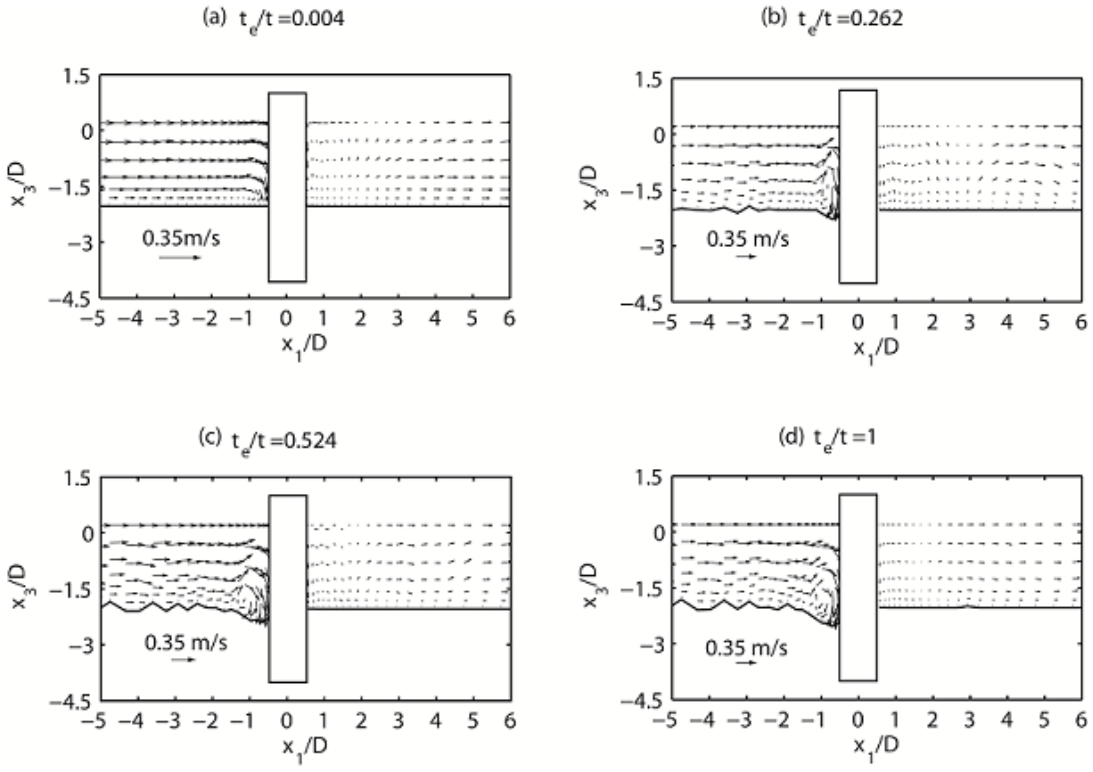

Figure 5.6 Vertical cross sections nearly along the centreline (at x_2/D=0.15), showing velocity-field and channel-bed profile development for Run C2.

Toward the end of the initial stage of the scour process (Figure 5.6b), eddy motions upstream of the pier intensify, especially at the foot of the pier. As the flow approaches the pier, u_1 decreases by 50% (from 0.37 m/s in the approach channel) and the flow reverses direction near the channel-bed. The reversal flow has a maximum speed of 0.16 m/s. At the pier nose, the downflow has a maximum speed of 0.83 m/s, at a depth equal to 72.5% the total depth below the water surface. Immediately downstream of the pier, the flow is downward, with a maximum speed of 0.1 m/s. The flow becomes upward at a horizontal distance of $x_1 / D = 2.4$. Further downstream of the pier, the flow becomes parallel to the channel-bed, and u_1 increases to a maximum of 0.39 m/s. Eddy motions downstream of the pier are weak and are not effective to cause scouring.

During the gradual development stage of scour (Figure 5.6c), the approach flow velocity

drops by 50% in the surface layer. The flow reverses its direction near the channel-bed, with a maximum speed of 0.16 m/s. At the pier nose, the downflow has a maximum speed of 0.65 m/s, occurring at a depth equal to 72.5% the total depth below the water surface. Immediately downstream of the pier, downflow up to 0.12 m/s takes place. The longitudinal velocity is the reverse direction over a horizontal distance of $x_1 / D = 1.5$. Far downstream of the pier the flow is parallel to the bed with a maximum value of 0.37 m/s.

At a state of equilibrium (Figure 5.6d), the longitudinal velocity decreases by 50% in the surface layer. Near the channel-bed, the flow reverses its direction, with a maximum speed of 0.13 m/s. At the pier nose, the downflow has a maximum speed of 0.75 m/s at a depth equal to 72.5% the total depth below the free surface. This maximum value is 2.39 times the average approach flow velocity. This value is an over-prediction. Copp and Johnson (1987) and Melville (1988) have suggested 0.8 times. The over-prediction is probably due to the use of fully slippery condition at the pier surface. Upstream of the pier, eddy motions are strong, removing sediments from the foot of the pier. Downstream of the pier, eddy motions are essentially the same as in Figure 5.6c.

Upstream of the pier, the bed slope along the channel centreline reaches 31° (Figure 5.6d), close to the angle of repose of uniform sediments (34º). In principle, the angle of repose of non-uniform sediments can be calculated using the formulation of Yang et al. (2009). However, this requires to track individual sediment grains, which is not feasible.

As an approximation, the angle of repose of non-uniform sediments is taken as 34º, which corresponds to uniform sands with d_{50} = 1 mm.

5.3.5 **Scour around the pier**

The development of scour and deposition is shown in Figure 5.7a-d. At the initial stage of scour development (Figure 5.7a), scouring ($d_s < 0$) emerges from two side areas upstream of the pier, which are somewhat symmetric about the channel centreline through the pier centre. The maximum value for scour depth, d_s, is $0.168D$ located at ($x_1 / D = -0.7, x_2 / D = 0.35$)]. At this stage, the pier nose has not shown any significant scour. Downstream of the pier, sediment deposition begins to both sides of the channel centreline, with a maximum height of $0.27D$ located at ($x_1 / D = 0.97, x_2 / D = -0.86$).

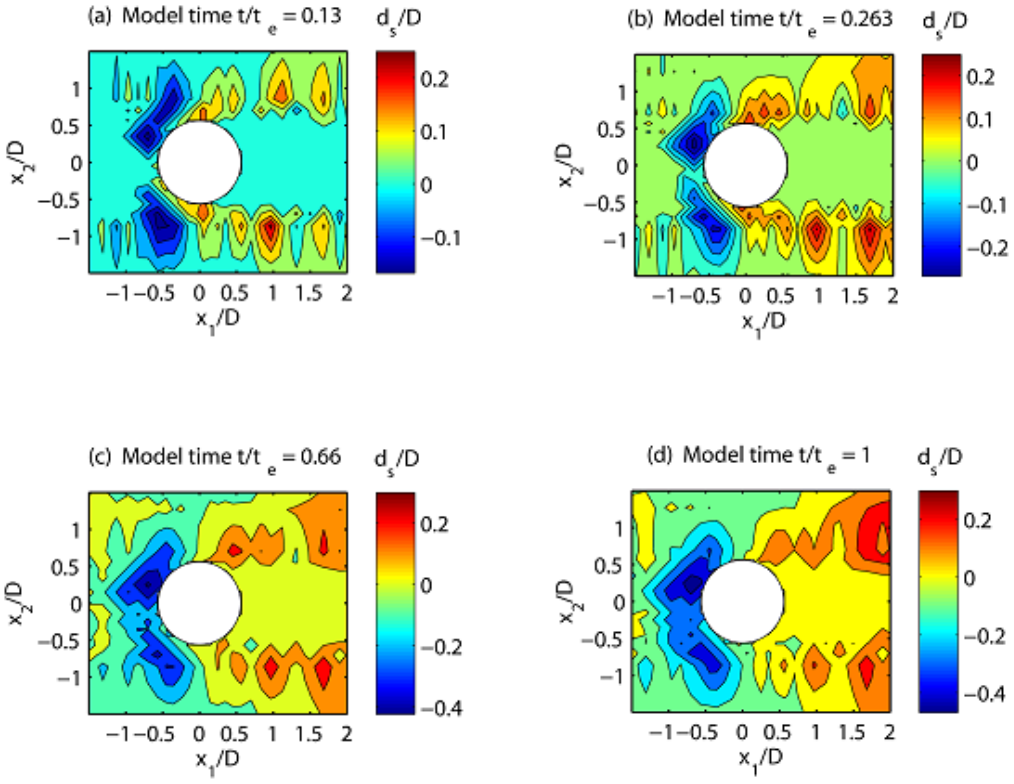

Figure 5.7 Contours of bed-level change for Run C2, showing scour ($d_s < 0$) and deposition ($d_s > 0$) developing around the pier.

Near the end of the initial stage (Figure 5.7b), d_s increases to $0.269D$ near the pier nose at ($x_1 / D = -0.69, x_2 / D = 0.25$). Deposition has a maximum height of $0.272D$ located at ($x_1 / D = 2.67, x_2 / D = -0.86$). The depth of the scour hole at the pier nose increases to

0.205D.

During the stage of gradual scour development (Figure 5.7c), d_s grows, the maximum value being 0.423D at the approximately same location as in Figure 5.7b. At the pier nose, d_s increases to 0.361D. Downstream of the pier, sediment deposition reaches a maximum height of 0.372D, with the location shifting slightly toward downstream. The scour patterns in Figure 5.7c appear to be less symmetric about the channel centreline than those in Figure 5.7b.

At a state of equilibrium (Figure 5.7d), d_s increases to a maximum of 0.471D at the same location as in Figure 5.7b,c. At the upstream nose, d_s reaches 0.458D. Downstream of the pier, deposition shifts toward downstream, with a maximum height of 0.4D near the end of the channel. The outer shape of the scour hole, upstream of the pier, is approximately half cone, which is very similar to the results reported in Richardson and Wacker (1999).

5.4 CONCLUSION

This study has extended a 3-D non-hydrostatic model for river flow applications (Pournazeri et al., 2013) to include the transport of non-uniform sediments as well as variations in riverbed level with time and space. With this extension, the model is suitable for prediction of the development of bridge-pier scour with non-uniform sediments. An application of the model has successfully reproduced the results of a non-uniform sediment scour experiment (Chang et al., 2004) with regard to equilibrium scour depth.

The suitability of the model for predicting 3-D velocity field and bed shear stress has been discussed in Pournazeri et al. (2013).

We show that the presence of a pier causes the approach flow to decelerate in the longitudinal direction and flow separation on the lateral sides of the pier. Flow deceleration

in the horizontal is compensated by the creation of a strong downflow immediately upstream of the pier or next to the pier nose. When reaching the channel-bed, the downflow is forced to circulate, giving rise to flow reversal and energetic eddy motions at the foot of the pier. The downflow combines with the eddy motions, effectively removing bed sediments locally from the pier foot. As a result, a scour hole develops around the pier. During this development, the bed-level changes which in turn causes changes to the flow field. The complex three-way interaction has been captured well in the model application.

Upstream of the pier, as the channel-bed evolves, downflow intensifies, reaching a magnitude greater than that of the approach flow. The same holds true for eddy motions. The development of scour hole continues until a state of equilibrium, at which the maximum slope angle of bed surface upstream of the pier is slightly smaller than the angle of repose of sediments. Downstream of the pier, flow circulations in the vertical and horizontal are shown to produce relatively weak vortices and wakes, whose intensities decrease with increasing distance from the pier toward downstream.

Scouring with non-uniform sediments emerges from the lateral sides of the pier, caused by strong velocities of flow bifurcating around the pier nose, and scour patterns migrate toward the pier nose, as the local downflow and eddy motions intensify with time. The initiating and migrating feature of scour patterns is common between uniform and non-uniform sediments.

With regard to equilibrium scour depth, the sediment size variation of surface bed materials plays an important role. Non-uniformity has the effect of reducing the magnitude of scour. It is not adequate to represent non-uniformity merely through an effective grain size (e.g. the median sediment size) for prediction of the equilibrium scour depth in non-

uniform sediments; the consequences include an overprediction. This study has demonstrated the importance of allowing for armouring, selective transport and relative exposure of sediment particles. It would be interesting to consider the effect of unsteadiness in future studies of bridge-pier scour.

Chapter 6 Conclusion and Suggestions for Future work

6.1 CONCLUSION

Scouring is one of the main factors in bridge failures. Cost effective design of piers' foundations requires accurate estimates of the scour depth. Most of the previous studies on computation of sediment scour around bridge's piers were conducted for uniform sediments as bed materials. Due to the non-uniform distribution of sediments sizes, considering the non-uniformity of bed materials in calculation of scour depths is significantly important and results in predictions at higher precisions. As bed shear stress is a significant issue in sediment transport calculations, we utilised an efficient method that reduces the numerical errors and computational costs. In addition, down-flow occurring upstream of the piers is one of the essential factors in scour depth. Thus considering the vertical acceleration of flow around a pier gives a rise to the accurate predictions of flow velocities and scour depth around the pier.

In this doctorate research, a 3-D multi-layer hydrodynamics model is developed that incorporates non-hydrostatic pressure corrections to simulate the flow passing around a pier and calculates the correspondent scour depth. The ECOMSED (HydroQual, 2002) code was initially used to simulate the flow in the channel. In order to consider the non-hydrostatic pressure corrections for vertical acceleration around the pier, we applied a seven-diagonal linear system. This system was solved for the corrected velocities by

employing preconditioned conjugate gradient iterations until residual norm was smaller than a given tolerance.

The model was initially tested in a fixed scour bed using the law-of-wall method to estimate the bed shear stress. To avoid large numerical errors in bed shear stress calculation, near bed velocities instead of velocities of the bottom layer were applied in calculations. Results from this simulation revealed a non-linear shrinkage of bed shear stress in the scour hole. Upstream of the pier, vortices had higher vorticity than those downstream. Upstream of the pier's nose, velocity of the down-flow was over-predicted. This over prediction might be due to applying a fully slippery condition on the pier surface and may be improved by treating the surface as partially-slippery. The calculated velocities and bed shear stresses were in excellent agreement with those measured in the experiment.

The model was further modified for mobile bed to simulate the scour depth around the pier. Using uniform sediment as bed material, the calculated flow velocities and scour depth matched the measurement data. The numerical results showed the realistic flow characteristics such as strong downward flow next to the upstream nose of the pier, and strong and weak vortices on upstream and downstream side of the pier foot, respectively.

The wakes produced downstream of the pier circulate in both clockwise and counter-clockwise directions. Intensified downward velocities and developed horseshoe vortices upstream of the pier cause the sediments to be removed from the upstream nose and deposited downstream. Bed scour emerges from the sides of the pier and patterns of increasing scour depth migrate upstream toward the nose. Furthermore, the scour hole upstream of the pier continues to develop until the bed slope reaches the sediment's angle of repose and the downstream edges of the scour hole extends until it reaches an

equilibrium state. Results also showed that the scour hole is shallower on the downstream than the upstream side and the calculated equilibrium scour depth and flow velocities around the pier are in good agreement with the measurement data.

Considering non-uniform sediments for bed materials, it was observed that the slope angle of the bed upstream of the pier was close to the sediment's angle of repose and the scouring downstream of the pier was negligible comparing to that upstream of the pier. The scour holes upstream of the pier had similar shapes to a half cone in both uniform and non-uniform sediment models. The equilibrium scour depth in uniform sediment was larger than that in a non-uniform bed due to the formation of an armour layer on the base of the scour hole in non-uniform sediment model.

This doctorate research has contributed to the following areas:

- The use of the shallow-water equations combined with non-hydrostatic pressure corrections resulted in high computational efficiency and provides the capacity to handle strong vertical motions in a scour hole.
- The near bed velocities instead of velocities of bottom layer were used to obtain bed shear stress predictions. This approach reduces the numerical errors in boundary layer and increase the computational efficiency.
- The non-uniformity of bed material was applied in the numerical model to calculate the scour depth around a pier. This approach is compatible with the scouring that happens in natural riverbed that contains non-uniform sediment grain sizes.
- The models used non-uniform mesh in horizontal and σ coordinate in vertical axes to apply kinematic and dynamic conditions at the varying bottom boundary more truthfully.

- The present model is more suitable for field scale applications versus other general CFD solvers that are computationally expensive in such cases.
- General purpose CFD code do not usually include sediment mixture transport. The model presented in this thesis reflects the real condition of riverbed materials (non-uniform sediment).
- The main application of this study is for the structural design of bridge piers and foundations. It can be extended to calculate scour around abutments and spur dikes.
- This study has not considered unsteady flow condition, and the model does not have the capability of calculating scour depth with cohesive bed materials and suspended load.

6.2 FUTURE WORK

1) The scour depth around a cylinder with non-uniform sediment should be estimated under unsteady flow conditions where the temporal flow discharge increases to the peak value similar to that in a non-uniform model under steady flow condition. In this regard, the impact of flow unsteadiness on the depth of the scour hole can be determined by comparing the scour depths obtained under steady versus unsteady flow conditions.
2) The scour depth around a single pier with different shapes should be investigated numerically in non-uniform bed, and the effect of the pier's shape on the scour depth and pattern can be studied. This will contribute to an efficient design of the bridge's foundation and its depth under the channel bed and subsequently decreases the probability of bridge's failure.

3) The scour depths in non-uniform bed around multi-piers with different arrangements and spacing should be investigated numerically to find the most appropriate configuration resulting in the minimum depth of the scour hole.
4) The live bed condition should be considered for numerical investigation of the scour depth around a pier in non-uniform sediments while the armouring diminishes.
5) Cohesive-sediment scour around a pier is worthy a while to numerically investigate.
6) Long-term temporal evolution of bed should be investigated; thus, variation in sediment porosity due to soil consolidation should be considered in uniform and non-uniform sediments transport models.

References

Aarabi, M., Chamani, M., Dehghani, A. & Asghari, K., 2011. Numerical simulation of temporal evolution of local scour in bridge pier with non-uniform sediment. *Advanced material Research,* Volume 250-253, pp. 3610-3614.

Akbari, M. & Price, S., 2005. Numerical investigation of flow patterns for staggered cylinder pairs in cross-flow. *Journal of Fluids & Structures,* Volume 20, pp. 533-554.

Akilli, H., Akar, A. & Karakus, C., 2004. Flow characteristics of circular cylinders arranged side by side in shallow water. *Journal of flow measurement & instrumentation,* Volume 15, pp. 187-197.

Ali, K. & Karim, O., 2002. Simulation of flow around piers. *Journal of Hydraulic Research,* 40(2), pp. 161-174.

Amini, A., Melville, B., Ali, T. & Ghazali, A., n.d. Clear-Water Local Scour around Pile Groups in Shallow-Water Flow. *J. Hydraul. Eng.,* 138(2), pp. 177–185.

Armanini, A. & Di Silvino, G., 1988. A one dimensional model for the transport of a sediment mixture in non-equilibrium conditions. *Journal of Hydraulic Research,* 26(3), pp. 275–292.

Baranya, S., Olsen, N., Stoesser, T. & Strum , T., 2013. A nested grid based computational fluid dynamics model to predict bridge pier scour. *Proceedings of the Institution of Civil Engineers–Water Management, DOI:* 10.1680/*wama.*12.00104.

Bernard, S. & Wallace, J., 2002. Turbulent flow: analysis, measurement, and prediction. s.l.:*Jouhn Wiley & Sons Inc*.

Borah, D., Alonso, C. & Prasad, S., 1982. Routing graded sediments in streams: Formulations. *Journal of the Hydraulics Division, ASCE,* 108(12), pp. 1486–1505.

Brandimarte, I., Paron, P. & Baldassarre, G., 2012. Bridge pier scour: A review of processes, measurements and estimates. *Environmental Engineering and Management Journal,* 11(5), pp. 975-989.

Breuer, M., 1998. Large eddy simulation of the subcritical flow past a circular cylinder: Numerical and modelling aspects.. *International Journal for Numerical Metods in Fluids,* Volume 28, pp. 1281-1302.

Brice, J. & Blodgett, J., 1978. Countermeasurements for hydraulic problems at bridges. *Federal Highway Administration Report FHWA-RD*-78-162.

Bui, M. & Rutschmann, P., 2010. Numerical modelling of non-equilibrium graded sediment transport in a curved open channel. *Computers & Geosciences,* Volume 36, pp. 792–800.

Casulli, V., 1999. A semi-implicit finite difference method for non-hydrostatic, free-surface flows. *International Journal for Numerical Methods in Fluids ,* 30(4), pp. 425–440.

Casulli, V., Cattani, E., 1994. Stability, accuracy and efficiency of a semi-implicit method for three-dimensional shallow water flow. *Computers & Mathematics with Applications,* 27(4), pp. 99–112.

Catalano, P., Wang, M., Iaccarino, G. & Moin, P., 2003. Numerical simulation of the flow around a circular at high reynolds numbers. *International Journal of Heat and Fluid Flow,* 24(4), pp. 463-469.

Chang, W., Lai, J. & Yen, C., 2004. Evolution of scour depth at circular bridge piers. *Journal of Hydraulic Engineering,* 130(9), pp. 905-913.

Chiew, Y., 1991. Bed features in non-uniform sediments. *Journal of Hydraulic Engineering, it*

Chiew, Y. & Melville, B., 1989. Local scour at bridge piers with non-uniform sediments. *Proceedings of the ICE - Water Management,* 87(2), pp. 215 –224.

Copp, H. & Johnson, J., 1987. Riverbed Scour at Bridge Piers. *Report WA-RD*-118.1*, the Department of Civil and Environmental Engineering, the Washington State University, Pullman, WA* 99164.

Dargahi, B., 1989. The turbulent flow field around a circular cylider. *Experiments in Fluids,* Volume 8, pp. 1-12.

Debnath, K. & Chaudhuri, S., 2010. Bridge pier scour in clay sand mixed sediments at near threshold velocity for sand. *Journal of Hydraulic Engineering, ASCE,* 136(9), pp. 597-609.

Dehghani, A., Esmaeili, T., Chang , W. & Dehghani, N., 2012. 3D numerical simulation of local scouring under hydrographs. *Proceedings of the Institution of Civil Engineers– Water Management,* 166(3), pp. 120–131.

Dey, S., 1995. Three-dimensional vortex flow field around a circular cylinder in a quasi-equilibrium scour hole.. *Sabhana, Proc. Indian Acad. Sci.,* 20(December), pp. 771-785.

Dey, S., Bose, S. & Sastry, G., 1995. Clear water scour of circular piers: a model. *Journal of Hydraulic Engineering,* 121(12), pp. 869-876.

Ettema, R., 1980. Scour at bridge pier. *PhD Thesis, Aukland University, Aukland Report No. 216.*

Ettema, R., Kirkil, G. & Muste, M., 2006. Similitude of large-scale turbulence in experiments on local scour at cylinders. *Journal of Hydraulic Engineering, ASCE,* 132(1), pp. 33-40.

Ettema, R., Melville, B. & Barkdoll, B., 1998. Scale effect in pier-scour experiments. *Journal of Hydraulic Engineering,* 124(6), pp. 639-642.

FHWA, 2001. Evaluating scour at bridges. *Washington DC, USA, Publication No. FHWA NHI* 01-001*, Hydraulic Engineering Circular No.* 18.

Fichenich , C., 2001. Stability thresholds for stream resortation materials. *Technical note: ERDC TN-EMRRP-SR-*29.*US Army corps of Engineers Research and development center. Vicksburg, Missippi, USA,* 10*p.*

Fischer-Antze, T., Ruther, N., Olsen, N. & Gutknecht, D., 2009. Three-dimensional (3D) modelling of non-uniform sediment transport in a channel bend with unsteady flow. *Journal of Hydraulic Research,* 47(5), pp. 670–675.

Grade, R. & Kothyari, U., 1998. Scour around bridge piers. *INSA senior scientist, Central Water and Power Research Station, Khdakwasla, Pune-*411024*, PINSA* 64*, A,* Issue 4, pp. 569-580.

Graf, W. & Altinakar, M., 1998. Fluvial hydraulics. *Wiley, Chichester, U.K.*

Graf, W. & Istiarto, I., 2002. Flow pattern in the scour hole around a cylinder. *Journal of Hydraulic Research,* 40(1), pp. 13-20.

Hechanova, R., 1977. Practical applications of the basic principles of hydraulics and soil mechanics in aquaculture engineering*. Tigbauan, Iloilo, Philippines: South china sea fisheries development and coordinating program report* 2, *SEAFDEC Aquaculture department facilities*.

Hong, J., Goyal, M., Chiew, Y. & Chau, L., 2012. Predicting time-dependent pier scour depth with support vector regression. *Journal of Hydrology,* Volume 468–469, pp. 241–248.

HydroQual, 2002 . A Primer for ECOMSED, Version 1.3. HydroQual, Inc., Mahwah, N.J. 07430.

Issa, R., 1985. Solution of the implicitly discretized fluid flow equations by oprator-splitting. *Journal of computational Physics,* Volume 62, pp. 40-65.

Jain, S. & Fischer, E., 1980. Scour around bridge piers at high flow velocities. *Journal of Hydraulic division, ASCE,* 106(11), pp. 1827-1842.

Johnson, P., 1992. Reliability-based pier scour engineering. *Journal of Hydraulic Engineeing,* 118(10), pp. 1344-1358.

Johnson, P., 1995. Comparison of pier-scour equations using field data. *Journal of Hydraulic EngineeringASCE ,* 121(8), pp. 626–629.

Julien, P. Y., 1995. Erosion and sedimentation. *Cambridge University Press, New york.*

Khosronejad, A., Kang, S. & Sotiropoulos, F., 2012. Experimental and computational investigation of local scour around bridge piers. *Advences in water resources ,* 37(March), pp. 73-85.

Kothyari, U., Grade , R. & RangaRaju, K., 1992. Temporal variation of scour around circular bridge piers. *Journal of Hydraulic Engineering, ASCE,* 118(8), pp. 1091-1106.

Kravchenko, A. & Moin, P., 2000. Numerical studies of flow over a circular cylinder at Re = 3900. *Physics of Fluids,* 12(2), pp. 403–417.

Kun, L., Dong-jun, M., De-jun, S. & Xie-yuan, Y., 2007. Wake patterns of flow past a pair of circular cylinders in side by side arrangements at low Reynolds numbers. *Journal of Hydrodynamics,* 19(6), pp. 690-697.

Lam , K., Gong, W. & So, R., 2008. Numerical simulation of cross-flow around four cylinders in an in-line square configuration. *Journal of Fluids & Structures,* Volume 24, pp. 34-57.

Lam , K. & Zou, L., 2009. Experimental study and large eddy simulation for the turbulent flow around four cylinders in an in-line square configuration. *International Journal of Heat & Fluid Flow,* Volume 30, pp. 276-285.

Laursen, e. & Toch, A., 1956. Scour around bridge piers and abutments. *Iowa Institute of Hydraulic Research Bulletin 4. State University of Iowa, Iowa City, Iowa..*

Lee, K. & Yang, K., 2009. Flow patterns past two circular cylinders in proximity.. *Computers & Fluids,* 38(4), pp. 778–788.

Lee, S. & Strum, T., 2009. Effect of sediment size scaling on physical modeling of bridge pier scour. *Journal of hydraulic engineering, ASCE,* 135(10), pp. 793-802.

Liang, D. & Cheng, L., 2005. Numerical Model for Wave-Induced Scour below a Submarine Pipeline. *Journal of Waterway, Port, Coastal, and Ocean Engineering,* 131(5), pp. 193–202.

Lin, G., 1993. Study on local scour around cylindrical bridge piers (in Chinese). *M.S. Thesis . Feng-Chia University, Taichung, Taiwan, R.O.C.*

Lin, Z., Yu-feng, L. & Kit, L., 2008. Large ddy simulation of flow arund cylinder arrays at a subcritical Reynolds number. *Journal of Hydrodynamics,* 20(4), pp. 403-413.

Lyn, D., Einav, S., Rodi, W. & Park, J., 1995. A laser Doppler velocimetry study of ensemble-average characteristics of turbulent wake of a square cylinder. *Journal of Fluid Mechanics,* Volume 304, pp. 285-319.

Mellor, G. & Yamada, T., 1982. Development of a turbulence closure model for geophysical fluid problems. *Reviews of Geophysics,* 20(4), pp. 851–875.

Melville, B., 1975. Local scour at bridge sites. *Report* No. 117, *University of Aukland, school of Engineering, New Zealand.*

Melville, B., 1988. Scour at Bridge sites. *Chapter* 15 *of Civil Engineering Practice 2 (Ed. Cheremisinoff, N.P., Cheng, S.L), Technomic Publishing Co., Pennsylvania.*

Melville, B., 1997. Pier and abutent scour: integrated approach.. *Journal of Hydraulic Engineering, ASCE,* 123(2), pp. 125-136.

Melville, B., 2008. The physics of local scour at bridge piers. *Fourth Interantional Conference on scour and erosion, ICSE-4, Tokyo,* pp.28-40.

Melville, B. & Chiew, Y., 1999. Time scale for local scour at bridge piers.. *Journal of Hydraulic Engineering, ASCE,* 125(1), pp. 59-65.

Melville, B. & Coleman, S., 2000. Bridge Scou. *Water Resources Publications, LLC.Highlands Ranch, CO, USA,* pp. 1–550.

Melville, B. & Raudkivi , A. J., 1977. Flow characteristics in local scour at bridge piers. *Journal of Hydraulic,* 15(4), pp. 373-380.

Melville, B. & Sutherland, A., 1988. Design method for local scour at bridge piers. *Journal of Hydraulic Engineering,* 114(10), pp. 1210-1226.

Mia, M. & Nago, H., 2003. Design method of time-dependent local scour at circular bridge pier. *Journal of Hydraulic Engineering,* 129(6), pp. 420–427.

Mohamed, T., Noor, M., Ghazali, A. & Huat, B. B., 2005. Validation of Some Bridge Pier Scour Formulae Using Field and Laboratory Data. *American Journal of Environmental Sciences,* 1(2), pp. 119-125.

Motta, D., Pacheco, R. & Telo, R., 2007. Advanced numerical modeling of the scouring process around the piers of a bridge. *Proceedings of the congress-internaional association for hydrauluc research,* 2; 594.

Muzzammil, M. & Ayyub, M., 2010. ANFIS-based approach for scour depth prediction at piers in non-uniform sediments. *Journal of Hydroinformatics,* 12(3), pp. 303-317.

Muzzammil, M. & Siddiqui, N., 2009. A reliability-based assessment of bridge pier scour in non-uniform sediments. *Journal of Hydraulic Research, IAHR,* 47(3), pp. 372–380.

Nagata, N., Hosoda, T., Nakato, T. & Muramoto, Y., 2005. Three dimensional numerical model for flow and bed deformation arounnd river hydraulic structures.. *Journal of hydraulic Engineering, ASCE,* 131(12), pp. 1074-1087.

Oliveto, G. & Hager, W., 2002. Temporal evolution of clear-water pier and abutment scour. *Journal of Hydraulic Engineering ASCE,* 128(9), pp. 811-820.

Olsen, N. & Melaaephillipn, M., 1993. Three-dimensional calculation of scour around cylinders. *Journal of Hydraulic Engineering, ASCE,* 119(9), pp. 1048–1054.

Palau-Salvador, G., Stoesser, T. & Rodi, W., 2008. LES of the flow around two cylinders in tandem. *Journal of Fluids and Structures,,* 24(8), pp. 1304–1312.

Papaioannou, G., Yue, D., Triantafyillou, M. & Karniadahis, G., 2006. Three-dimensionality effects in flow around two tandem cylinders. *Journal of Fluid Mechanics,* Volume 558, pp. 387-413.

Papaioannou, G., Yue, G., Triantafyllou, M. & Karniadakis, G., 2007. On the effect of spacing on the vortex-induced vibrations of two tandem cylinders. *Journal of Fluids & Structures,* Volume 24, pp. 833-854.

Paphitis, D., 2001. Sediment movement under unidirectional flows: an assessment of empirical threshold curves. *Coastal Engineering,* 43(3-4), pp. 227–245.

Parker, G., 1990. Surface-based bedload transport relation for gravel rivers. *Journal of Hydraulic Research,* 28(4), pp. 417-436.

Pasiok, R. & Stilger-szyd, E., 2010. Sediment particles and turbulent flow simulation around bidge piers. *Archives of Civil and Mechanical Engineering, Institute of Geotechnics and Hydrotechnics, Wrocaw University of Technology,* X(2), pp. 67-79.

Piomelli, U. & Liu, J., 1995. Large -eddy simulation of rotating channel flows using a localized dynamic model. *Phys.Fluids,* 7(4), pp. 839-848.

Pournazeri, S., Li, S. S., Haghighat, F., 2013. Efficient non-hydrostatic modelling of flow and bed shear stress in a pier scour hole. *Submitted to Canadian Journal of Civil Engineering.*

Rahuel, J. et al., 1989. Modelling of riverbed evolution for bedload sediment mixtures. *Journal of Hydraulic Engineering,* 115(11), pp. 1521–1542.

Raikar, R. & Dey, S., 2005. Clear-water scour at bridge piers in fine and medium gravel beds. *Canadian Journal of Civil Engineering,* 32(4), pp. 775-781.

Raudkivi, A., 1986. Functional trends of scour at bridge piers. *Journal of Hydraulic Engineering, ASCE,* 112(1), pp. 1-13.

Raudkivi, A. & Ettema, R., 1983. Clear water at cylindrical piers. *Journal of Hydraulic Engineering,* 109(3), pp. 338-350.

Richardson, J. & Wacker, A., 1999. Bridge scour and stream instability counter measures in stream stability and scour highway bridges. *In Compendium of papers ASCE Water Resources Engineering.*

Richarson, J. & Panchang, V., 1998. Three-dimensional simulation of scour inducing flow at bridge piers. *Journal of Hydraulic Engineering ASCE,* 124(5), pp. 530-540.

Rodi, W., 1993. Turbulence models and their application in hydraulics : *A state of the art review*, Institute of Hydrodynamics, University of Karlsruhe, Karlsruhe.

Roulund, A., Sumer, B., Fredsoe, J. & Michelsen, J., 2005. Numerical and experimental investigation of flow and scour around a circular pile. *Journal of Fluid Mechanics,* Volume 534, pp. 351-401.

Sadeque, M., Rajaratnam, N. & Loewen, M., 2008. Flow around cylinder in open channels. *Engineering Mechanics,ASCE,* 134(1), pp. 60-71.

Said, N., Mhiri, H., Bournot, H. & Le Palec, G., 2008. Experimental and numerical modelling of the three dimensional incompressible flow behavior in the near wake of circular cylinder. *Journal of Wind Engineering and Industrial Aerodynamics,* Volume 96, pp. 471-502.

Salaheldin, T., Imran, J. & Chaudhury, M., 2004. Numerical modeling of three-dimensional flow field around circular piers. *Journal of Hydraulic Engineering–ASCE,* 130(2), pp. 91–100.

Sarker, M., 1998. Flow measurements around scoured bridge piers using Acoustic Doppler Velocimeter (ADV). *Flow measurement & Instrumentation,* 9, pp. 217-227.

Schewe, G., 1983. On the force fluctuations acting on a circular cylnder in crossflow from subcritical up to transcritical Reynolds numbers. *Journal of Fluid mechanics*, Volume 133, pp. 265-285.

Sheppard, D. & Miller, M., 2006. Live bed pier scour experiments. *Journal of hydraulic Engineering, ASCE,* 132(7), pp. 635-642.

Sheppard, D., Odeh, M. & Glasser, T., 2004. Large scale clear waterlocal pier scour experiments. *Journal of Hydraulic Engineering, ASCE,* 130(10), pp. 957-963.

Sheppard, D., Ontowirjo, B. & Zhao, G., 1995. Local scour near single piles in steady currents. *Proc, 1st Hydraulic Engineering Conference, San Antonio.*

Shields, A., 1936. Application of similarity principles and turbuence research to bedload movement. *Hydrodynamics laboratory. California institute of technology,* Issue 167.

Shirole, A. & Holt, R., 1991. Planning for a comprehensive bridge safety assurance program. *Transportationn Research Record,* Issue 1290, pp. 137-142.

Smagorinsky, J., 1963. General circulation experiments with the primitive equations. *Monthly Weather Review*, 91(3), pp.99-164.

Singh, S.P., Mittal, S., 2005. Flow past a cylinder: shear layer instability and drag crisis. *International Journal for Numerical Methods in Fluids,* 47(1), pp. 75–98.

Srinivas, Y., Biswas, G., Parihar, A. & Ranjan, R., 2006. Large eddy simulation of high reynolds number turbulent flow past a square cylinder. *Journal of Engineering Mechanics ASCE,* 132(3), pp. 327-335.

Tison, L. J., 1961. Local scour in rivers. *Journal of Geophysical Research.* 66, pp. 4227–4232.

Tritthart, M. & Schober, B., 2011. Non-uniformity and layering in sediment transport modelling 1: flume simulations. *Journal of Hydraulic Research IAHR,* 49(3), pp. 325–334.

Unger, J. & Hager, W., 2007. Down-flow and horseshoe vortex characteristics of sediment embedded bridge piers. *Experiments in Fluids,* 42(1), pp. 1-19.

van Rijn, L., 1984. Sediment transport. Part I: Bed load transport. *Journal of Hydraulic Engineering,, ASCE,* 110(10), pp. 1431-1456.

Wang, G. & Vanka, S., 1996. Large eddy simulations of high Reynolds number turbulent flow over a square cylinder.. *Dept. of Mechanical and Industrial Engineering Rep. No. CFD* 96-02*, Univ. of Illinois at Urbana-Champaign.*

Wilcox, D., 1993. Turbulence modelling for CFD.. *DCW Industries, Inc., California..*

Yang, F., Liu, X., Yang, K., Cao, S., 2009. Study on the angle of repose of non-uniform sediment. *Journal of Hydrodynamics*, 21(5), pp. 685-691.

Yanmaz, A. & Altinbelik, H., 1991. Study of time dependent local scour around bridge piers. *Journal of Hydraulic Engineering, ASCE,* 117(10), pp. 1247-1268.

Yeh, J., 1996. The flow fields around square and circular cylinders mounted vertically on a fixed flat bottom (in Chinese) . M.S. Thesis. Natiional Chunng-Hsing Universit*. , Taichung, R.O.C.*

Yen, C., Lai, J. & Chang, W., 2001. Modeling of 3D flow and scouring around circular piers. *Proceedings of the National Science of Republicc of China,* 25(1), pp. 17-26.

Zou, L., Lin, Y. & Lam, K., 2008. Large eddy simulation of flow around cylinder arrays at a subcritical Reynolds number. *Journal of Hydrodynamics,* 20(4), pp. 403–413.

Appendix A

Hydrodynamics Model Equations with Hydrostatic Approximation

The hydrodynamics model ECOMSED (HydroQual, 2002) is used for computation of the flow velocity and free surface elevation. On the Cartesian coordinates system (x_1, x_2, x_3), let the x_3-axis point positively upwards, and the equilibrium water level be the vertical datum. The free surface islocated at $x_3 = \eta(x_1, x_2, t)$, and the channel-bed at $x_3 = -H(x_1, x_2)$. For an incompressible fluid under the hydrostatic pressure, the continuity and momentum equations are given by

$$\frac{\partial u_j}{\partial x_j} = 0, \qquad j = 1, 2, 3 \tag{A.1}$$

$$\frac{\partial u_i}{\partial t} + \frac{\partial (u_i u_j)}{\partial x_j} = -\frac{1}{\rho}\frac{\partial p}{\partial x_i} + \frac{\partial}{\partial x_3}\left(K_M \frac{\partial u_i}{\partial x_3}\right) + F_i, \qquad i = 1, 2;\ j = 1, 2, 3 \tag{A.2}$$

$$-\frac{\partial p}{\partial x_3} = \rho g \tag{A.3}$$

where u_j and p are unknown and K_M is vertical eddy viscosity. To calculate p, one should compute the surface elevation, η.

The horizontal diffusion due to subgrid-scale motions is given by

$$F_i = \frac{\partial}{\partial x_j}\left[A_M\left(\frac{\partial u_i}{\partial x_j} + \frac{\partial u_j}{\partial x_i}\right)\right], \qquad i = 1, 2; \qquad j = 1, 2 \tag{A.4}$$

The horizontal eddy viscosity is calculated according to Smagorinsky's (1963) scheme

$$A_M = (C_s \Delta x_1 \Delta x_2)\sqrt{2S_{ij}S_{ij}}, \qquad i = 1, 2; \qquad j = 1, 2 \tag{A.5}$$

where C_s is in the range of 0.1 to 0.24 and $S_{ij} = 0.5(\partial u_i / \partial x_j + \partial u_j / \partial x_i)$ is the mean strain rate. The diffusion term is required to damp small scale noise in the predicted velocity field.

The vertical eddy viscosity is obtained by appealing to a second order turbulence closure scheme developed by Mellor and Yamada (1982). This scheme relates turbulent mixing to turbulence kinetic energy, $q_t^2/2$, and turbulence macro-scale, l. These two quantities are predicted using unsteady advection-diffusion equations. The vertical eddy viscosity and diffusivity are calculated as $K_M = lq_t/B_1^{1/3}$ and $K_q = lq_tS_q$, where K_M is vertical eddy diffusivity and K_q is vertical eddy diffusivity. Mellor and Yamada (1982) suggested that B_1, E_1, E_2 and S_q are equal to 16.6, 1.8, 1.33 and 0.2, respectively.

In order to solve the flow field in a given model channel, appropriate conditions at the boundaries of the channel must be specified. There are four types of boundaries: the free water surface, channel bed, sidewalls and lateral open boundaries. The treatments of these boundaries are described below: At the free surface, the dynamic condition is that the shear stress is zero; the kinematic condition is that fluid particles on the surface will stay on the surface all the time, expressed as

$$u_3 = u_1 \frac{\partial \eta}{\partial x_1} + u_2 \frac{\partial \eta}{\partial x_2} + \frac{\partial \eta}{\partial t}, \qquad \text{at } x_3 = \eta(x_1, x_2, t) \tag{A.6}$$

At the channel bed, the dynamic condition that the bed shear stress is specified according to the quadratic law

$$\vec{\tau}_b = C_D \rho |\vec{u}_b| \vec{u}_b, \qquad \text{at } x_3 = -H(x_1, x_2) \tag{A.7}$$

The kinematic condition that the normal component of the velocity vector is zero, mathematically expressed as

$$u_3 = -u_1 \frac{\partial H}{\partial x_1} - u_2 \frac{\partial H}{\partial x_2}, \qquad \text{at } x_3 = -H(x_1, x_2) \tag{A.8}$$

On the channel and pier sidewalls, due to excessively high computational costs, it is difficult to have grid spacing fine enough to resolve lateral boundary layers associated with the sidewalls. The dynamic condition is that the sidewalls are fully slippery, and the kinematic condition is that the velocity component normal to the sidewalls is zero.

Appendix B

Non-hydrostatic Pressure Corrections

The pressure field calculations in Appendix A give reasonable results for a flat-bottom part channel (Figure 3.1a,b). For the region of a scour hole, it is necessary to consider non-hydrostatic pressure distribution. The calculations in Appendix A produce provisional velocity field and surface elevation. Corrections to the provisional solutions are described as follows:

The corrected velocities are expressed as (Casulli, 1999)

$$u_1(i+1,j,k) = \tilde{u}_1(i+1,j,k) - \psi \frac{\Delta t}{\Delta x_1}\left[m(i+1,j,k) - m(i,j,k)\right] \tag{B.1}$$

$$u_2(i,j+1,k) = \tilde{u}_2(i,j+1,k) - \psi \frac{\Delta t}{\Delta x_2}\left[m(i,j+1,k) - m(i,j,k)\right] \tag{B.2}$$

$$u_3(i,j,k+1) = \tilde{u}_3(i,j,k+1) - \psi \frac{\Delta t}{\Delta x_3}\left[m(i,j,k+1) - m(i,j,k)\right] \tag{B.3}$$

where the implicitness factor is in the range of $0.5 \leq \psi \leq 1$ for stability ($\psi = 0.5$ in this study). Assuming that the pressure in the surface cells is hydrostatic, the pressure correction m in the bottom layer is obtained from

$$g(\eta - x_3) = g(\overline{\eta} - x_3) + m \tag{B.4}$$

Substituting the new velocities [Equations (B.1) – (B.3)] into the continuity equation [Equation (A.1)] and Equation (B.4) yields a seven diagonal linear system for the non-hydrostatic pressure. This system is symmetric and has positive definition. The system can

be solved for the corrected velocities by using preconditioned conjugate gradient iterations until residual norm is smaller than a given tolerance.

With regards to boundary conditions, on the sidewalls and pier's surface, the non-hydrostatic pressure is such that the normal flux is zero. At open boundaries, the non-hydrostatic pressure is specified. At the water surface, the non-hydrostatic pressure is zero.

Once the non-hydrostatic pressure is solved, the velocities are updated using Equations (B.1) - (B.3).The free surface elevation is updated as below

$$\eta = \tilde{\eta} + m / g \tag{B.5}$$

For more details, refer to (Casulli, 1999).